AN INVESTIGATION OF THE DEUTERON-NUCLEUS TENSOR INTERACTION IN $^{90}Zr(\vec{d},\vec{d})^{90}Zr$ ELASTIC SCATTERING

by

David J. Abbott

A dissertation submitted to the faculty of the University of North Carolina at Chapel Hill in partial fulfillment of the requirements for the degree of Doctor of Philosophy in the Department of Physics and Astronomy.

Chapel Hill

1990

Approved by :

Hugon J. Kaworski Advisor

_____ Reader

_____ Reader

Abstract

DAVID J. ABBOTT. An Investigation of the Deuteron-Nucleus Tensor Interaction in $^{90}Zr(\vec{d},\vec{d})^{90}Zr$ Elastic Scattering. (Under the direction of Dr. Hugon J. Karwowski.)

An investigation of the role of the deuteron-nucleus tensor interaction is made through measurement of angular distributions of the cross section, analyzing powers and the polarization transfer observable (PTO) $3K_y^{z'z'}+K_{yy}^{z'z'}$ for deuteron elastic scattering from ^{90}Zr at 15 MeV. Two compact and efficient deuteron polarimeters based on the $^3He(d,p)^4He$ reaction were designed and built to perform the polarization transfer measurements.

The observable $K_y^{z'z'}$ proved to be very sensitive to the presence of a T_r-type tensor interaction and also to provide information which cannot be obtained through measurement of tensor analyzing powers. The measurement of PTO and of the tensor analyzing power A_{xz} provide a particularly effective means of parameterizing the tensor interaction.

Phenomenological optical model calculations give a real T_r potential which differs significantly from folding model predictions, in that it is weaker and predominantly surface-peaked. The imaginary T_r potential, however, is in qualitative agreement with the folding model. In addition to the optical model analysis, finite-range coupled-channels calculations were performed coupling the three most strongly populated ^{90}Zr(d,p)^{91}Zr states to the elastic channel in order to gauge the contribution of the (d,p) channel to the deuteron-nucleus tensor interaction. Coupling effects on the observables were found to be small and equivalent to that of an imaginary T_r tensor potential 1/5 of that used in the optical model analysis.

Acknowledgments

I came to the University of North Carolina knowing that I wanted to study nuclear physics, and in hindsight I don't know that I could have made a better choice. Much of what made my education here fruitful came from Professors Tom Clegg and Ed Ludwig as well as Dr. Bill Thompson. Their continued support and guidance through the years was much appreciated as I learned "the trade". The bulk of my experience, however, came from working with many of my fellow graduate students. Most of them have gone on into the cruel world now, but to Dr. Robert Varner, Dr. James Bowsher, Dr. Roy Fauber, Dr. Tim Mooney and last but not least Dr. Tom Spencer I owe many thanks both for the knowledge they have imparted to me as well as their friendship over the years.

Early on in my struggles with the polarization transfer project a new Professor at UNC, Dr. Hugon Karwowski, took a interest in the work and and came to my rescue. He provided the impetus as well as the experimental knowledge to make the whole project work. I shall always be grateful for his support as my advisor and even for his little "pushes" along the way to get me out of graduate school.

Even given the technical support and training I could not have completed this work without the theoretical motivation and background first provided by Dr. Felipe Santos and later extended in help with analysis of the data by Dr. Jeff Tostevin. To them both I am indebted.

To the friends an colleagues I leave behind, Eric Crosson, Susan Lemieux, Dr. Rupak Das, Kurt Fletcher, Tim Black and others, I thank for the many hours and midnights given to this project and for all the good times we had. Good Luck!

To the director Dr. Ed Bilpuch and all the support personnel at the Triangle Universities Nuclear Lab; Bob Rummel, Paul Carter, Sidney Edwards, Pat Mulkey and many others, I appreciate their support for this project.

Funding for this project was also provided in part by the Department of Energy.

Finally, I wish to thank my wife Donna who has been with me from the very beginning, in both the good times and hard times. I could not have made it to the finish line without her love and support. I dedicate this dissertation to her and to my sons Robert and James.

TABLE OF CONTENTS

LIST OF TABLES

LIST OF FIGURES

Chapter I

Introduction

1.1 The deuteron-nucleus interaction

The scattering of deuterons from complex nuclei is of particular interest because it allows one to study the simplest composite nucleus and its interaction with other nuclei. We pretend we understand the nucleon-nucleus interaction having investigated scattering phenomena at nucleon incident energies from keVs to GeVs, from which numerous models have stemmed ranging from global optical model parameterizations to quark models. It is therefore all the more surprising to find that when a proton and neutron are combined to form a bound state so much of the resulting deuteron-nucleus interaction is still not well understood. That is not to say that models do not exist that describe the data. To the contrary, there have been many investigations of deuteron elastic scattering at many different energies, most of which have provided a reasonable description of the observables (some of these are briefly described in section 2.2). The problem is that a majority of these studies were really too phenomenological in their approach to provide a good quantitative description of the interaction. While some parameterizations may do well in predicting elastic scattering observables they in do not reproduce the inelastic reaction channels through DWBA analysis. Only recently have investigations begun to look into a more complete description by taking into consideration the more dominant inelastic

processes (see section 2.3). This is in a large part due to the increased sophistication of computer codes and more computing power for analysis of a complex problem.

What "sweetens the pot", so to speak, and makes deuteron scattering so interesting is, of course, the nature of the bound state. There are several features of the deuteron which complicate its interaction with a nucleus. The first comes from the fact that the proton and neutron have their spins aligned, forming a spin 1 projectile. This provides the deuteron-nucleus interaction with a rich variety of polarization phenomena to study (this is discussed in more detail in Chapter III), but in return it makes experimental measurements much more complex to perform. A related property of the deuteron is the fact that it is not spherical but rather has a significant D-state component to its wave function. Hence, its orientation with respect to the nucleus becomes very important in describing the interaction. This is particularly true for the spin-dependent parts of the interaction. Finally, the deuteron is not very strongly bound (E_B = -2.225 MeV). So, as scattering energies increase so does its propensity to break-up. Also because it is so weakly bound the deuteron is a rather large and "floppy" object. Therefore, attempts to treat it as a particle with no internal degrees of freedom could meet with somewhat unphysical results. It is all the more interesting then that the deuteron single folding model prescription describes the data as well as it does (see section 2.1).

One of the significant failures, however, of the folding model is its predictions for the deuteron-nucleus tensor interaction. While there is little question that a tensor potential of some form is necessary for a reasonable description of the elastic scattering observables, at energies above the Coulomb barrier folding model predictions do not describe the tensor-force-sensitive observables well at all. As stated earlier, this is not altogether unusual. It is simply an indication that more complicated processes are present and, within the phenomenological framework of the optical model based on the simple folding of the proton and neutron scattering

potentials, it is difficult (if not impossible) to distinguish between all these processes and their contributions to elastic scattering.

1.2 Goals for this work

It is the primary objective of the work described in this dissertation to focus on one aspect of the deuteron-nucleus interaction, specifically the tensor interaction, and to provide a more quantitative study than previous optical model analyses into its form and possible origins. This was accomplished in two major ways. First, a compact and efficient deuteron polarimeter was designed and built (see Chapter IV) in order to measure polarization transfer observables (PTO) in deuteron elastic scattering from heavy nuclei. The PTO measurements provided new information independent of the standard single scattering observables ($\frac{d\sigma(\theta)}{d\Omega}$, iT_{11}, T_{20}, T_{21}, T_{22}) and uniquely sensitive to the tensor interaction (see Chapter III). Because polarization transfer experiments for deuteron scattering are so involved, one target, ^{90}Zr, was chosen on which to make these measurements, because it had both experimental and theoretical advantages as discussed in Chapter V. Second, analyses using both an optical model formalism and a coupled-channels formalism were employed (see Chapter VI). They were used to first determine the role of complex tensor potentials in predicting the elastic scattering observables and then to quantitatively define the contributions of specific inelastic channels to the elastic scattering potentials, in particular to measure effects on the deuteron-nucleus tensor interaction. Of primary interest to this work are neutron transfer, or $^{90}Zr(d,p)^{91}Zr$, coupling to elastic scattering and the nature of the spin-dependent potential generated in the elastic channel by this coupling. So, in addition to the $^{90}Zr(\vec{d},\vec{d})^{90}Zr$ scattering observables at 15 MeV, measurements of $^{90}Zr(d,p)^{91}Zr$ cross sections for three strongly populated states in ^{91}Zr were also

made. The (d,d) and (d,p) data and their analysis are discussed in detail in Chapter V.

By providing new experimental information for elastic scattering and making a theoretical analysis within a coupled-channels framework, it is believed that a more quantitative study of the deuteron-nucleus tensor interaction in elastic scattering and its possible origins can be made.

A brief description of the topics discussed in this dissertation by chapter is as follows:

Chapter II : *Theoretical Background* - A general theoretical description of the deuteron interaction with nuclear matter is given, starting with a simple folding model for the deuteron. This model provides predictions that can be used in an optical model analysis of deuteron elastic scattering, including the tensor interaction. Some results of previous analyses and the problems they faced are discussed. Finally, a brief discussion is presented of recent attempts to include other reaction channels through coupling and their effects on the elastic scattering.

Chapter III : *Methods in Polarization Experiments with Deuterons* - Details of the formalism for performing polarization experiments with spin-1 particles are discussed, including definitions of all the observables which may be measured. Simplifications of the relations for use in elastic-scattering experiments are shown, followed by a discussion of the sensitivity of observables to the tensor interaction.

Chapter IV : *The Polarimeter* - The design, performance and calibration of a deuteron polarimeter for making polarization transfer measurements is described. General experimental techniques including data

acquisition methods and the electronics set-up using the polarimeter are also given.

Chapter V : *Data Acquisition and Analysis* - Details of all the experiments performed for this work and the results are described including measurements of the elastic single scattering observables for $^{90}Zr(\vec{d},d)^{90}Zr$, the polarization transfer measurements and the $^{90}Zr(d,p)^{91}Zr$ cross section measurements.

Chapter VI : *Optical Model and Coupled Reaction Channels Calculations* - Optical model calculations are made for $^{90}Zr(\vec{d},\vec{d})^{90}Zr$ at 15 MeV, concentrating on the role of tensor potentials (specifically a T_r-type potential) in generation of the elastic observables. Following this phenomenological analysis, calculations are made that include coupling several strongly populated (d,p) channels to the elastic channel. The effective tensor potential generated in the elastic channel through this coupling is estimated. Finally, possible contributions from coupling to other inelastic channels are also discussed.

Chapter VII : *Summary and Conclusions* - Concluding remarks are made including suggestions for future study related to this work.

Chapter II

Theoretical Background

2.1 The folding model and tensor potentials

The basic assumption in the static single folding model (first introduced by Watanabe [Wat58]) is that the deuteron-nucleus interaction can be approximated by a potential $U_0(\mathbf{R})$ made up of the sum of proton-nucleus and neutron-nucleus potentials averaged over the internal wave function $\phi_d(\mathbf{r})$ of the deuteron. The effective Hamiltonian for the system made up of the proton, neutron and nucleus is

$$\begin{aligned} H &= K_p + K_n + V_p(\mathbf{r}_p) + V_n(\mathbf{r}_n) + v_{np}(\mathbf{r}_p - \mathbf{r}_n) \\ &= K_{\mathbf{R}} + V_p(\mathbf{R} - \tfrac{1}{2}\mathbf{r}) + V_n(\mathbf{R} + \tfrac{1}{2}\mathbf{r}) + [K_{\mathbf{r}} + v_{np}(\mathbf{r})] \end{aligned} \tag{2.1}$$

where the center of mass coordinate $\mathbf{R}=\frac{1}{2}(\mathbf{r}_p+\mathbf{r}_n)$ and the relative coordinate $\mathbf{r}=\mathbf{r}_n-\mathbf{r}_p$ have been introduced (see Figure 2.1). V_p and V_n are the individual nucleon-nucleus potentials, usually taken to be the optical potentials, and v_{np} is the n-p interaction potential that determines the deuteron binding. The K_i are the corresponding kinetic energy operators. The Schrödinger equation associated with the above Hamiltonian is

$$\left[-\frac{\hbar^2}{4m}\nabla_{\mathbf{R}}^2 + V(\mathbf{R},\mathbf{r}) - \frac{\hbar^2}{m}\nabla_{\mathbf{r}}^2 + v_{np}(\mathbf{r}) \right] \psi(\mathbf{R},\mathbf{r}) = E\psi(\mathbf{R},\mathbf{r}) , \tag{2.2}$$

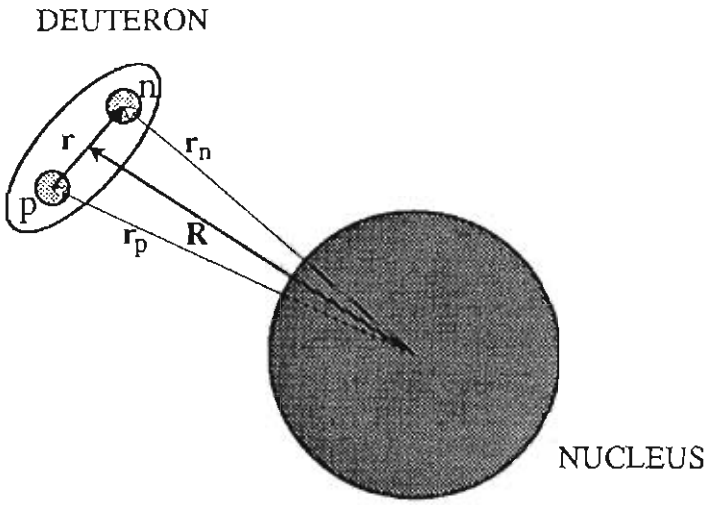

Figure 2.1 - Coordinate systems used for the deuteron single folding model

where $V(\mathbf{R},\mathbf{r}) = V_p + V_n$. The wavefunction $\psi(\mathbf{R},\mathbf{r})$ may be considered separable for large $\mathbf{R}$ where $\psi(\mathbf{R},\mathbf{r}) = \Phi_0(\mathbf{R})\phi_d(\mathbf{r})$. The wave function $\Phi_0(\mathbf{R})$ describes the motion of the deuteron as a single particle relative to the nucleus. If one assumes minimal distortions of the deuteron in the scattering process, then the effective folded potential, $U_0(\mathbf{R})$, integrated over the internal motion of the deuteron is

$$U_0(\mathbf{R}) = \int \phi_d^2(\mathbf{r}) V(\mathbf{R},\mathbf{r}) d\mathbf{r} \ . \tag{2.3}$$

The resulting Schrödinger equation simplified from Eqn. 2.2 becomes

$$[K_{\mathbf{R}} + U_0(\mathbf{R})]\Phi_0(\mathbf{R}) = E_0\Phi_0(\mathbf{R}) \ , \tag{2.4}$$

where E_0 is the incident energy of the deuteron. The deuteron potential $U_0(\mathbf{R})$ can be written in a more specific form, for use in an OM formalism, by identifying the central, spin-orbit and tensor parts [Kea73]. If $\phi_d(\mathbf{r})$ is written in the form

$$\phi_d(\mathbf{r}) = \left[\frac{u(r)}{r} + \frac{w(r)}{r\sqrt{8}} S_{pn}(r) \right] , \tag{2.5}$$

where $u(r)$ and $w(r)$ are the S and D-state parts of the wave function respectively and the spin operator $S_{pn}(r) = 3(\sigma_p \cdot r)(\sigma_n \cdot r) - (\sigma_p \cdot \sigma_n)$ describes the angular dependence of the D-State part ($\propto Y_2(\theta)$), also if the function $V(\mathbf{R},\mathbf{r})$ in Eqn. 2.3 is written in optical model form , $V(\mathbf{R},\mathbf{r}) = V_C + V_{SO}\sigma \cdot \mathbf{L}$, where V_C and V_{SO} are complex central and real spin-orbit potentials respectively, then $U_0(\mathbf{R})$ can be written as

$$U_0(\mathbf{R}) = U_C(R) + U_{SO}(R)\mathbf{S}\cdot\mathbf{L} + U_T(R)[(\mathbf{S}\cdot\boldsymbol{R})^2 - \tfrac{2}{3}] , \tag{2.6}$$

where $\mathbf{S} = \frac{1}{2}(\sigma_p + \sigma_n)$ is the spin-1 operator for the deuteron. Substituting for $\phi_d(\mathbf{r})$ and $V(\mathbf{R},\mathbf{r})$ into Eqn. 2.3 and keeping the largest terms we have [Kea73]

$$U_C(R) = \frac{2}{4\pi}\int V_C(|\mathbf{R} + \tfrac{1}{2}\mathbf{r}|)\left[\frac{u(r)}{r}\right]^2 d\mathbf{r} , \tag{2.7a}$$

$$U_{SO}(R) = \frac{1}{4\pi}\int \frac{V_{SO}(|\mathbf{R} + \frac{1}{2}\mathbf{r}|)}{r^2} \times \left[\left(u^2 - \frac{uw}{\sqrt{2}}\right)\left(1 + \frac{\mathbf{r}\cdot\mathbf{R}}{2R^2}\right) + \frac{3uw}{\sqrt{8}} sin^2\theta \right] d\mathbf{r} , \tag{2.7b}$$

$$U_T(R) = \frac{6\sqrt{2}}{4\pi}\int V_C(|\mathbf{R} + \tfrac{1}{2}\mathbf{r}|)\frac{uw}{r^2}P_2(\theta)\, d\mathbf{r} . \tag{2.7c}$$

The deuteron potential in this approximation is made up of a complex central, a real spin-orbit and a complex tensor potential. The presence of the tensor term U_T requires the inclusion of the D-state term $w(r)$ in the deuteron wave function. The tensor operator associated with U_T is known as the T_r operator. Satchler [Sat60] showed that there can be three possible forms of the tensor operators, provided that certain symmetries hold for the interaction potential. These include rotational invariance, parity conservation, and the equivalent of time reversal invariance for a

complex potential[1] . They are generally refered to as T_r, T_p and T_L and are defined as

$$T_r = (\mathbf{S}\cdot\boldsymbol{R})^2 - \frac{2}{3}, \tag{2.8a}$$

$$T_p = (\mathbf{S}\cdot\mathbf{P})^2 - \frac{2}{3}P^2, \tag{2.8b}$$

$$T_L = (\mathbf{S}\cdot\mathbf{L})^2 + \frac{1}{2}(\mathbf{S}\cdot\mathbf{L}) - \frac{2}{3}L^2, \tag{2.8c}$$

where $\boldsymbol{R}$ is a unit vector defined previously , $\mathbf{P}$ is the deuteron momentum operator and $\mathbf{L}$ is the relative angular momentum of the deuteron with respect to the nucleus.

In this model, a T_r potential arises in first order from the inclusion of the deuteron D-state and is the type generally used in the studies of the deuteron-nucleus interaction. However, tensor potentials of the T_p and T_L type can also arise. An extension of the folding model to second order (i.e. by including products of the nucleon spin-orbit terms) introduces a T_L coupling,even without $w(r)$. This is generally expected to be quite small [Sat60]. A T_L term may also arise when coupling to virtual break-up channels [Sta70, Kea73, Ise89]. The role of the T_p-type tensor potential is somewhat less clear. In general though if one were to introduce velocity dependent or non-local potentials this can give rise to a T_p coupling [Sat60]. Another property of consequence for these tensor operators should be noted here, namely that while T_L conserves orbital angular momentum ($\mathbf{L}$), T_p and T_r not only couple partial waves of the same L ($\Delta L=0$) but also partial waves for which $\Delta L=2$ (not $\Delta L=1$ because of parity). This property of T_r and T_p is useful for distinguishing polarization phenomena associated primarily with the tensor interaction, as opposed to the scalar and vector interactions. There have been several studies done introducing various forms of the tensor interactions to describe deuteron elastic scattering [God79,Tak87,Lai88], but

---

[1] Satchler indicates that time reversal invariance cannot be imposed because the interaction potential is complex. Instead he simply requires the scattering matrix to be symmetric or that the potential be a simple central potential of the form V(r) + iW(r) for both the spin-dependent and non-spin-dependent parts.

the evidence to date seems to indicate that the use of the T_r form is sufficient to provide a good description to the data, at least at relatively low bombarding energies. It is not clear from these studies, however, that the folding model prediction for T_r describes the data well at all.

2.2 The optical model and deuteron scattering

Tensor potentials in the optical model

In the optical model the incident projectile is treated as a particle moving in a potential that represents the effective interaction between the nucleons in the projectile and the nucleons in the target. This potential must be in general *complex* where the imaginary part represents in a gross way the loss of flux from the elastic channel into competing inelastic processes. These may be nuclear reactions or target and projectile excitations, break-up, etc. In addition, the optical potential is usually chosen to be *local* in that the interaction should depend only on the wave function at the CM position **R** from the target and not be influenced by values anywhere else. The OM central potential is also generally taken to be *spherically symmetric* so that it as well as other potential form factors are functions of the radial position only. Finally, because the deuteron is a spin-1 projectile the OM potential must include *spin-dependent* parts, including a vector **L•S** term and up to three tensor terms corresponding to T_r, T_p, and T_L. For spin-0 target nuclei there is are spin-spin interaction terms.

There is a basic assumption in the OM formalism which must hold in order for the elastic scattering to be well described. When one considers the competing inelastic processes present it is assumed that none of the channels has a more profound effect on the elastic channel than any other and that they all "add up" in such

a way as to average those effects out. In this way they can be treated through an "effective" imaginary potential. Failure of this assumption can cause some difficulties for deuteron optical models to provide good descriptions of the data over a wide mass and energy range. In any case, the most general form for the deuteron optical potential [Sat60] assuming the scattering of a spin-1 projectile from a spin-0 nucleus is[2]

$$V(R,S) = V_{Coul}(R) + V_C(R) + V_{SO}(R)\boldsymbol{L}\cdot\boldsymbol{S} + V_{T_r}(R)T_r + V_{T_L}(R)T_L + \tfrac{1}{2}[V_{T_p}(R)T_p + T_pV_{T_p}(R)] \; . \qquad (2.9)$$

The $V_i(R)$, with $i = C, SO, T_r, T_L, T_p$, are complex functions (form factors) representing each potential type. They are generally taken to be Woods-Saxon or Woods-Saxon derivative forms, $V(R) = V_0(1+e^x)^{-1}$ where $x = (R - R_0A^{1/3})/a$. A complete description of these potentials is given in Appendix A.

The folding model provides predictions for these potentials, and while all form factors (both real and imaginary) may be present in general, the FM predicts, when including a complex nucleon-nucleus central potential and real spin-orbit potential, only a complex central potential, a real spin-orbit potential V_{SO} and a complex T_r potential.

Results from previous OM analyses

Earlier analyses of deuteron elastic scattering have included data taken with a wide variety of targets at many different energies. In a typical single-scattering experiment with incident polarized deuterons one may measure angular distributions of the cross section as well as vector analyzing power A_y and tensor analyzing

---

[2] This form is also subject to the symmetry properties discussed in section 2.1 regarding tensor potentials (i.e. parity, rotations and time reversal).

powers (A_{xz}, A_{xx}, A_{yy} and A_{zz})[3]. Some initial success was made in calculating these observables using FM predictions for energies below the Coulomb barrier [Knu73,75]. It was apparent from this study of d + ^{90}Zr at 5.5 MeV that predictions for the TAP were essentially zero without a T_r potential and including it provided an good description of the observables. In other studies at higher energies [Bür72, Kea73, Bak75, God79, Dae80, Tak87] it was generally found that while the FM predictions used in the OM analyses provided a qualitatively good description of the cross section and vector analyzing power, it completely missed when it came to predicting the TAP data. This was especially true for A_{xz} which provides the strongest sensitivity to T_r.

Goddard [God78,79] was among the first to make systematic attempts to determine the form of the deuteron-nucleus tensor potential. Included in his analysis were a complete set of TAP measurements for targets from ^{40}Ca to ^{122}Sn at energies ranging from 10 to 15 MeV. He found that in a majority of cases the real T_r potential was in general very small (often consistent with zero), while the imaginary T_r potential was consistent with or larger than FM predictions (W_{T_r}≈1-4 MeV). He found little or no evidence for the inclusion of a T_p or T_L potential at least within the OM framework. Figure 2.2 shows as an example the large discrepancy in the forms for the FM tensor potentials and those needed to fit the tensor analyzing power data. Goddard also indicated that an imaginary spin-orbit potential of the same form as the real spin-orbit consistently improved agreement with the data - both vector and tensor analyzing powers. It should be noted, however, that his tensor potential parameterizations when the imaginary spin-orbit potential was included differed significantly from their original forms when no imaginary spin-orbit term was included. In addition, the geometries for his T_r parameterizations varied significantly with target

---

[3] The A_{ij} are Cartesian forms of the analyzing powers. They are related to the spherical tensor analyzing powers, namely- $A_y \propto iT_{11}$, A_{yy}-$A_{xx} \propto T_{22}$, $A_{xz} \propto T_{21}$ and $A_{zz} \propto T_{20}$. See Chapter III and Appendix B for a more complete description of the polarization observables.

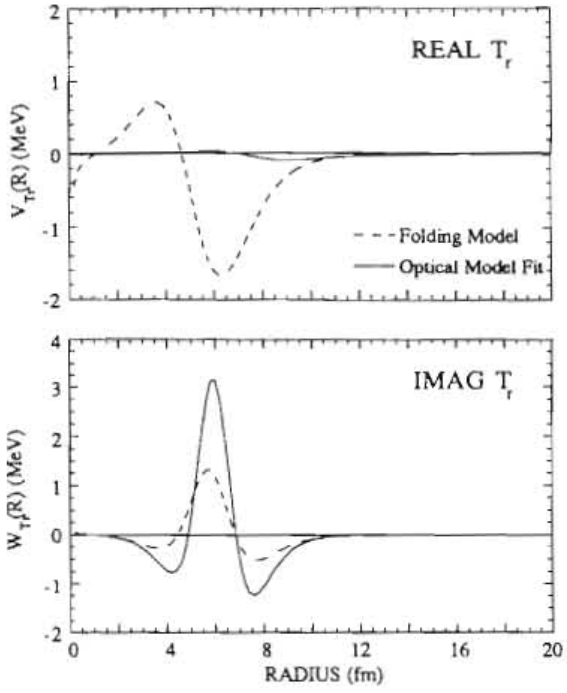

Figure 2.2 - T_r type tensor potentials for $^{90}Zr(d,d)$ scattering at 15 MeV. The dashed line is the folding model prediction and the solid curve represents a best fit optical potential from [God79].

mass and energy.

In contrast to Goddard's analysis an investigation by Takei *et al.* at a slightly higher energy of 22 MeV [Tak87] resulted in somewhat better agreement with the FM tensor interaction, although the real T_r potentials obtained were still small ($V_{T_r} \approx 2$ MeV). The geometry used in their analysis, while being significantly different from FM predictions, was also in general more consistent for the various isotopes studied (A = 40 to 110). Contrary to Goddard's analysis, Takei *et al.* discounted the use of an imaginary spin-orbit potential indicating that its effects on the vector and tensor analyzing powers were small. This may in part explain the larger T_r potentials determined in their analysis. This study of the T_r potential at 22 MeV had the advantage of consistently large values of T_{21} (or A_{xz}) primarily at backward angles. It was these T_{21} data that were used to parameterize the tensor potentials. Their attempts at including T_p and T_L type potentials also (as with Goddard's analysis) met with no success in improving agreement with experimental data.

It is not obvious whether the discrepancies between these OM studies of deuteron scattering are real, in that not enough is known about the energy dependence of the tensor interaction or the inelastic processes which may also contribute, or are just due to limitations of the data sets. This is one motivating factor for extending the

data base to the measurement of polarization transfer observables. As we will discuss in the next chapter, cross section and analyzing powers do not fully determine the scattering matrix for deuteron elastic scattering. Other observables (PTO) can be measured that provide not only new information but also information more sensitive to the tensor interaction.

2.3 Inelastic channels - modifications toward a more quantitative study.

It has been stressed in the preceding sections that the deuteron is not a static object forever sitting in its ground state, but rather one that is quite able to undergo changes in the scattering process. This "softness" has manifested itself in the many problems that exist in reproducing the data. There have been attempts in the past to account for some of the dominant inelastic processes in deuteron scattering and for their effects on elastic scattering. It is hoped that in this way one may resolve some of the discrepancies which continue to exist in conventional OM analyses.

Deuteron break-up

Among the first inelastic processes to be considered quantitatively was the break-up of the deuteron [Sta70]. Unfortunately, it is also the most difficult one to handle theoretically. One of the first realistic calculations of deuteron break-up [Raw77,78] which included spin-dependent effects indicated that break-up generated significant vector and tensor potentials in the elastic channel. This was some justification [God78] to add an imaginary spin-orbit term to the optical potential at least to account for the vector effects. However, because break-up is such a non-local process there is some question as to whether is can be realistically treated with an

effective local optical potential.

More recently, deuteron break-up has been treated at intermediate energies (56 MeV) [Ise89] and at energies below the Coulomb barrier [Tos87]. These are two very different regions of deuteron scattering that showed some interesting contrasts.

Tostevin [Tos87] found that break-up of the deuteron at sub-Coulomb energies (from the Coulomb field only) does not contribute at all to the vector (spin-orbit) dependence in the deuteron-nucleus interaction; However, Coulomb break-up does generate an attractive T_r interaction $\propto(Z^2/R^4)$ which can contribute to the deuteron-nucleus tensor interaction and the elastic TAP. This tensor term differs significantly from what the folding model prediction for T_r (Eqn. 2.6) reduces to as the incident energy falls below the Coulomb barrier and the nuclear potentials no longer contribute to its strength. The deuteron D-state T_r contribution is repulsive in nature, $\propto 3Q_dZ/(2R)^3$, where Q_d is the deuteron quadrupole moment) and can be calculated exactly.

Iseri *et al.* [Ise89] used a method of Coupled Discretized Continuum Channels (CDCC) [Yah82] to include virtual-break-up effects. This method allowed them to consider the multi-step process of break-up into specified continuum states and subsequent recombination and its effects on the elastic channel observables. This was done for several nuclei (A = 16-208) at incident deuteron energies of 21.5 MeV and 56 MeV. The results were that they found quite large effects for both the cross section and analyzing powers. The nature of the tensor spin dependence, however, was associated primarily with a T_L-type interaction. Some T_r sensitivity was seen through introduction of the deuteron D-state in the calculations. The effects calculated also varied significantly with target mass and with incident energy.

It is known that the break-up cross sections generally get larger with increasing bombarding energy and target Z. One would expect therefore that the effects it has on the elastic scattering would also vary. At higher energies indications

are that break-up plays an important role in the vector and T_L tensor spin dependence [Ise89] while at sub-Coulomb energies T_r tensor effects seem more significant [Tos87]. This is interesting because, while it is generally believed that the understanding of deuteron break-up is essential in accurately describing the deuteron-nucleus interaction, it still remains essentially a 3-body problem with no easy solution.

Transfer reactions

Another process which is related to deuteron break-up but is theoretically a little easier to handle is the deuteron stripping or (d,p) reaction. It is also one of the subjects of interest for this dissertation. Unlike break-up, where the neutron is scattered into continuum states, the neutron is captured by the nucleus into a bound state that has a well defined energy, spin and parity. Effects on the elastic scattering can be calculated by coupling the two-step process of stripping and pick-up to the direct elastic channel. It is expected also that these effects should be stronger for nuclei near closed shells where the stripping cross sections are larger.

One of the first theoretical investigations into the possible spin-dependent effects by transfer channel coupling to the elastic scattering was done by Rawitcher and Mukherjee [Raw71]. They looked at (d,d) and (d,p) scattering from ^{40}Ca at 11 MeV. Their analysis showed a very large contribution to the elastic iT_{11} by coupling to the (d,p) $2p^{1/2}$ and $2p^{3/2}$ states in ^{41}Ca. They, however, made no quantitative investigation of tensor contributions.

More recent calculations at sub-Coulomb energies [Tos83,87] for (d,d) and (d,p) from ^{208}Pb at 8-9 MeV have indicated that coupling generates considerable contributions to the spin-dependent potentials of the elastic channel. In fact, it was shown that both the vector and tensor analyzing powers can be completely accounted

for without the addition of the spin dependence predicted from the folding model. This is not altogether unusual because at sub-Coulomb energies the deuteron does not really probe the nuclear potentials from which this spin dependence is generated. The generation of a T_r tensor interaction via the coupling, however, is a motivating factor for studies at higher energies. An interesting consequence of these results is to bring into question use of phenomenological optical potentials in describing the deuteron-nucleus interaction at sub-Coulomb energies.

As a final note, it should be mentioned that coupling to stripping channels is not the only process that is being investigated in relation to deuteron elastic scattering. Recent calculations involving coupling to mass-3 channels (i.e. (d,t) and (d,^{3}He)) have been done for ^{40}Ca at 52-80 MeV [Mac87]. The basic assumption for this analysis is that it is not cross sections which determine the strength of the coupling so much as the projectile-target overlap, which is much larger in general for the pick-up channels than for stripping channels. They found very large changes in the elastic central potentials caused by this coupling. They however made no conjectures as to the effect on the spin-dependent potentials. Still, it provides more support to the idea that deuteron scattering can only be understood through quantitative investigations of this type.

Chapter III

Methods in Polarization Experiments with Deuterons

3.1 Polarization formalisms

In the investigation of polarization phenomena from nuclear reactions and scattering experiments there are five general classes of experiments one can attempt[1]:

a)	$A(\vec{b},c)D$	Analyzing power experiment
b)	$A(b,\vec{c})D$	Polarization experiment
c)	$A(\vec{b},\vec{c})D$	Polarization transfer
d)	$\vec{A}(\vec{b},c)D$	Spin correlation (initial channel)
e)	$A(b,\vec{c})\vec{D}$	Spin correlation (final channel) (3.1)

These do not apply to every type of scattering experiment involving particles with spin. For the case of deuteron elastic scattering from a spinless target only a)-c) are applicable. In addition, a) and b) provide essentially the same information, assuming time-reversal invariance. Until fairly recently, analyzing power experiments were performed almost exclusively. This type of experiment, however, cannot provide a

[1] In practice the spins of more than two particles or reactants can be measured, but it has been shown [Sim67,70] that the measurement of two spins at one energy and angle is sufficient to completely determine all scattering amplitudes.

complete description of the interaction. A polarization transfer experiment must also be made in order to completely determine the scattering amplitudes.

In this chapter a formalism for the description of spin-1 polarization is introduced that will include definitions of the different types of polarization observables that can be measured in an experiment of the form **1** + **A** —> **1** + **B**. For this work the primary concern is for the specific case of deuteron elastic scattering and target spins **A**=**B**=0. This information is presented in more detail in several papers [Ohl72a, Ohl72b, Sal73, Rob74, Spe83], the most comprehensive being a review paper on polarization transfer experiments by Ohlsen [Ohl72a]. We provide here a summary of most of the important ideas, as well as information applicable to deuteron elastic scattering experiments.

Coordinate systems

To describe the polarization observables measured in a deuteron elastic scattering experiment it is necessary to define several coordinate frames to which they may be associated. The first reference frame S is called the *projectile helicity frame* and is defined with the positive z axis along the incident beam direction $\boldsymbol{k}_{in}$ (see Figure 3.1). The y axis is perpendicular to the scattering plane defined by $\boldsymbol{k}_{in}$ and $\boldsymbol{k}_{out}$ in the direction $\boldsymbol{k}_{in}\times\boldsymbol{k}_{out}$. The x axis is then defined to complete the right-handed coordinate system. There are two scattered particle reference frames of interest. These are called the *outgoing reactant helicity frames* S′(lab) and S′(CM) and correspond to the z′ axis along the unit vectors $\boldsymbol{k}_{out}$(lab) and $\boldsymbol{k}_{out}$(CM) respectively. In both the S and S′ frames y=y'.

The direction of the spin vector of the incident beam is described following the Madison convention [Bar70], for which the angle β refers to the angle between the z

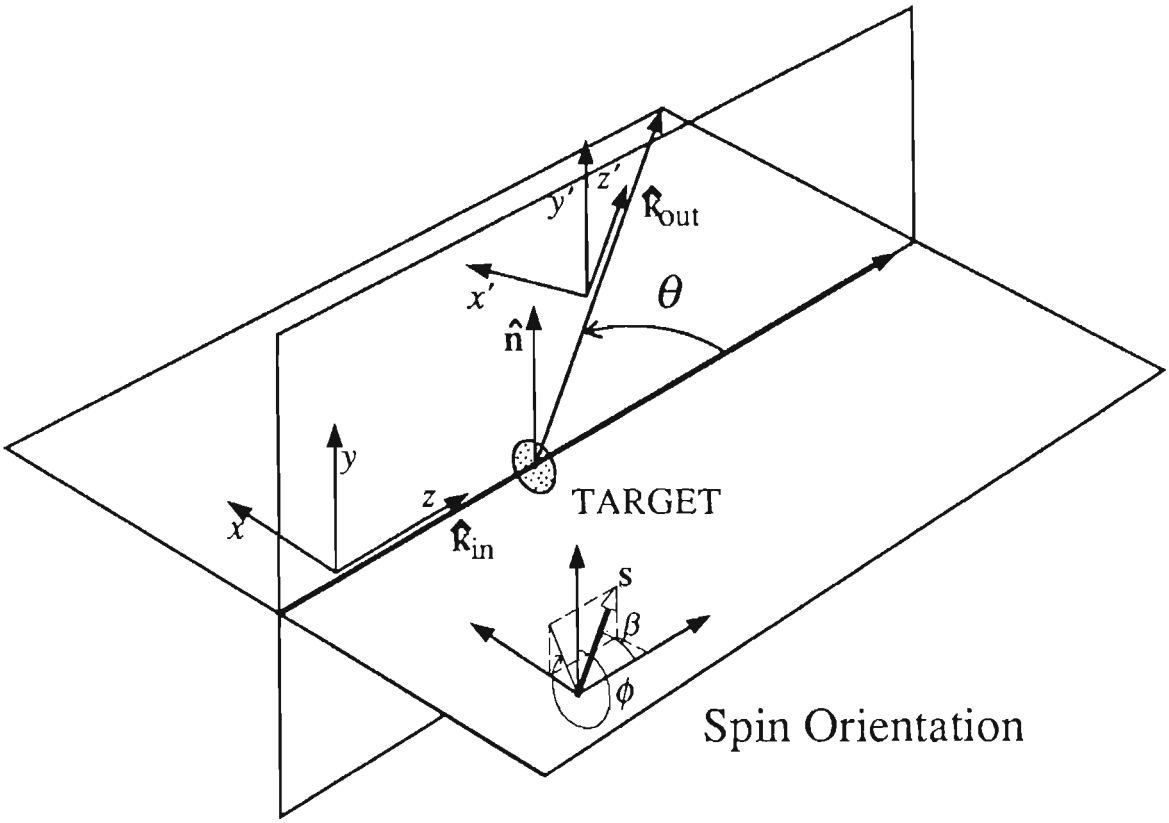

Figure 3.1 Coordinate systems and spin orientations for use in deuteron scattering experiments

axis and the spin vector S so that $\cos\beta = S \cdot k_{in}$. The azimuthal angle ϕ is the angle made with the projection of S in the x-y plane and the y axis. The angles β and ϕ can also be associated with a Cartesian frame defined as X,Y and Z which is determined at the polarized source. There Z refers to the direction of the spin symmetry axis, as is discussed in more detail in section 3.3.

Spin-1 formalism

The deuteron is a spin-1 particle and thus can exist in one of three spin angular momentum states. The spin wave function of the deuteron, $\chi(S)$, is a three-component spinor, so the density matrix, ρ, that describes the polarization state of a

deuteron beam will therefore be a 3×3 Hermitian matrix. The basic spin-1 angular momentum operators can also be expressed as 3×3 matrices, namely:

$$S_x = \frac{1}{\sqrt{2}}\begin{pmatrix} 0 & 1 & 0 \\ 1 & 0 & 1 \\ 0 & 1 & 0 \end{pmatrix} \quad S_y = \frac{1}{\sqrt{2}}\begin{pmatrix} 0 & -i & 0 \\ i & 0 & -i \\ 0 & i & 0 \end{pmatrix} \quad S_z = \begin{pmatrix} 1 & 0 & 0 \\ 0 & 0 & 0 \\ 0 & 0 & -1 \end{pmatrix} \tag{3.2}$$

Note that S_z is diagonal, with the corresponding eigenvalues for spin-1.

These three operators, however, are not sufficient to completely describe the deuteron beam polarization state. A total of nine operators is necessary to span the space. One can construct a set of operators from those listed in Eqn. 3.2. The Cartesian form of these nine operators can be written as [Gol58]

$$\begin{aligned} &S_i && i=x,y,z \\ &S_{ij} = \tfrac{3}{2}(S_iS_j + S_jS_i) - 2\delta_{ij}\mathbf{1} && i,j=x,y,z \end{aligned} \tag{3.3}$$

where S_i are the vector polarization operators and S_{ij} are the operators corresponding to the tensor polarization moments. Exact forms of these matrices are given in Appendix B. Including the identity matrix $\mathbf{1}$, this gives an over-complete set. There is therefore a relational constraint for the tensor operators,

$$S_{xx} + S_{yy} + S_{zz} = \begin{pmatrix} 0 & 0 & 0 \\ 0 & 0 & 0 \\ 0 & 0 & 0 \end{pmatrix} \tag{3.4}$$

The density matrix can be expanded in terms of these operators as follows,

$$\rho = \frac{1}{3}\left[I + \frac{3}{2}(p_x S_x + p_y S_y + p_z S_z) + \frac{2}{3}(p_{xy} S_{xy} + p_{yz} S_{yz} + p_{xz} S_{xz}) + \frac{1}{3}(p_{xx} S_{xx} + p_{yy} S_{yy} + p_{zz} S_{zz}) \right] \quad (3.5)$$

where the $p_{ij} \equiv \langle S_{ij} \rangle = \mathrm{Tr}(\rho S_{ij})$ are the expectation values for each operator. They also represent the individual polarization components for the state. The constraint equation for the p_{ij} takes the form $p_{xx} + p_{yy} + p_{zz} = 0$.

As was mentioned before, the above equations form the Cartesian representation for a spin-1 system. It is often useful to use the spherical tensor notation to represent the polarization state for deuterons, in particular in section 3.3 when the polarization observables are represented in terms of scattering matrix elements. The irreducible spherical tensor operators are represented by τ_{kq} where k=0,1,2 and $|q| \leq k$, and the corresponding polarization components[2] are $t_{kq} \equiv \langle \tau_{kq} \rangle$. The density matrix can then be written in a particularly simple form:

$$\rho = \frac{1}{3}\mathbf{1}\left(\sum_{kq} t_{kq} \tau_{kq}^{\dagger} \right) \quad (3.6)$$

Both the Cartesian and spherical tensor notations are useful in the description of polarization phenomena in scattering and both will be used throughout this thesis interchangeably. The Cartesian notation will be used more in the discussion of experiments, while in theoretical discussions the spherical tensor notation generally proves more convenient.

It should also be noted here that all the quantities (operators, polarizations, observables,density and scattering matrices) are defined with respect to some reference axes. This becomes specifically important in the discussion of scattered

[2] Refer to Appendix B for the relationship between Cartesian and spherical tensor operators and polarization components. It should be noted that k=0,1,2 represent the scalar, vector and tensor components of the spin 1 polarization state; hence $\tau_{2q} \propto p_{ij}$, $\tau_{1q} \propto p_i$ and $\tau_{00} = \mathbf{1}$.

polarized deuteron beam and the measurement of polarization transfer observables and their relation to the scattering matrix amplitudes.

3.2 Deuteron elastic scattering

When a deuteron beam (spin-1) with density matrix ρ_i describing its polarization is elastically scattered from a spinless target[3], the scattered beam's polarization state is then expressed by a matrix ρ_f. The two states are related via a scattering matrix M:

$$\rho_f = M\rho_i M^\dagger. \tag{3.7}$$

The (3×3) matrix M is in general made up of nine complex amplitudes which are functions of both energy and scattering angle. This scattering matrix provides all the information about the scattering reaction in question. Determination of all its components can in principle be achieved through measurement of all polarization observables.

There are restrictions for the elements of the scattering matrix which result from the various symmetries being applied. This reduces the number of independent amplitudes which must be measured. Parity conservation reduces this number from nine to five. For elastic scattering, time-reversal invariance provides an additional constraint[4] reducing it to four independent complex amplitudes or in other words seven numbers plus an overall phase. Hence a minimum of seven observables at each energy and angle must be measured to completely determine the scattering matrix [Lop77,Els88].

---

[3] The following arguments in this section hold for the general case concerning spins **1 + A --> 1 + B**.
[4] The exact form of this constraint is dependant on the reference axes chosen to describe the matrix.

The classification of observables one can measure can be derived from Eqn. 3.7. In particular, if ρ_i is normalized to unity, then the intensity for a polarized deuteron beam is given by

$$I(\theta,\phi) \equiv \mathrm{Tr}(\rho_f) = \mathrm{Tr}(M\rho_i M^\dagger). \tag{3.8}$$

For an unpolarized incident beam (i.e. $\rho_i = \frac{1}{3}\mathbf{1}$) then $I(\theta,\phi) \equiv I_0(\theta) = \frac{1}{3}\mathrm{Tr}(MM^\dagger)$. The scattered polarization moments are defined in the same way as the incident moments by the relations

$$\begin{aligned} p_{k'} &\equiv \langle S_{k'} \rangle = \mathrm{Tr}(\rho_f S_{k'})/\mathrm{Tr}(\rho_f) \ , \\ p_{k'l'} &\equiv \langle S_{k'l'} \rangle = \mathrm{Tr}(\rho_f S_{k'l'})/\mathrm{Tr}(\rho_f) \ . \end{aligned} \tag{3.9}$$

By using Eqns. 3.5 and 3.7 one can get generalized expressions for the polarized cross section and outgoing polarizations [Ohl72a];

$$\begin{aligned} I(\theta,\phi) &= I_0(\theta)\left[1 + \frac{3}{2}\sum_j p_j A_j(\theta) + \frac{1}{3}\sum_{j,k} p_{jk} A_{jk}(\theta)\right] \\ p_{l'} I(\theta,\phi) &= I_0(\theta)\left[P^{l'}(\theta) + \frac{3}{2}\sum_j p_j K_j^{l'}(\theta) + \frac{1}{3}\sum_{j,k} p_{jk} K_{jk}^{l'}(\theta)\right] \\ p_{l'm'} I(\theta,\phi) &= I_0(\theta)\left[P^{l'm'}(\theta) + \frac{3}{2}\sum_j p_j K_j^{l'm'}(\theta) + \frac{1}{3}\sum_{j,k} p_{jk} K_{jk}^{l'm'}(\theta)\right] \end{aligned} \tag{3.10}$$

where the functions $A(\theta)$ (analyzing powers), $P(\theta)$ (outgoing polarizations) and $K(\theta)$ (polarization transfer coefficients) are given by

$$A_j(\theta) = \frac{\mathrm{Tr}(MS_jM^\dagger)}{\mathrm{Tr}(MM^\dagger)} \qquad A_{jk}(\theta) = \frac{\mathrm{Tr}(MS_{jk}M^\dagger)}{\mathrm{Tr}(MM^\dagger)}$$

$$P^{l'}(\theta) = \frac{\mathrm{Tr}(MM^\dagger S_{l'})}{\mathrm{Tr}(MM^\dagger)} \qquad P^{l'm'}(\theta) = \frac{Tr(MM^\dagger S_{l'm'})}{\mathrm{Tr}(MM^\dagger)} \tag{3.11}$$

$$K_j^{l'}(\theta) = \frac{\mathrm{Tr}(MS_jM^\dagger S_{l'})}{\mathrm{Tr}(MM^\dagger)} \qquad K_j^{l'm'}(\theta) = \frac{\mathrm{Tr}(MS_jM^\dagger S_{l'm'})}{\mathrm{Tr}(MM^\dagger)}$$

$$K_{jk}^{l'}(\theta) = \frac{\mathrm{Tr}(MS_{jk}M^\dagger S_{l'})}{\mathrm{Tr}(MM^\dagger)} \qquad K_{jk}^{l'm'}(\theta) = \frac{\mathrm{Tr}(MS_{jk}M^\dagger S_{l'm'})}{\mathrm{Tr}(MM^\dagger)}$$

These functions are the invariant polarization observables characteristic of the scattering interaction itself (i.e. they depend only on the incident energy and scattering angle). One can see that they are made up of linear combinations of the products of scattering matrix amplitudes. One should also note that Eqn. 3.10 is written as a generalized contraction of scalar, vector and tensor components. However, not all of the observables are allowed under the symmetry constraints which have been previously imposed. There are three useful rules to govern which coefficients may be present. These are discussed in more detail elsewhere [Ohl72a] and are given here without proof. For the case of a reaction where the y and y' axes are perpendicular to the reaction plane $\boldsymbol{k}_{in}\times\boldsymbol{k}_{out}$, let N_x, N_y and N_z be the number of times x,y or z appears as a coefficient index. Then,

(1) If $N_x + N_z$ is odd, the coefficient is zero by parity conservation (i.e. $A_{xy} = 0$).

(2) If $N_x + N_y$ is odd, the coefficient is an odd function of the scattering angle, θ. This is a consequence of rotational invariance.

(3) If N_x is odd, the corresponding coefficient in the inverse reaction reverses sign (i.e. $K_x^{z'} = K_z^{x'}$). For elastic scattering the forward and inverse reaction are identical by time-reversal for the reference frames S and S′(CM).

Employing the above rules, one obtains the general form of the polarization observables for the reaction **1** + **A** --> **1** + **B** shown in Eqn. 3.12.

$$
\begin{aligned}
I(\theta,\phi) &= I_0\left[1 + \tfrac{3}{2}p_y A_y + \tfrac{3}{2}p_{xz}A_{xz} + \tfrac{1}{3}\left(p_{xx}A_{xx} + p_{yy}A_{yy} + p_{zz}A_{zz}\right)\right] \\
p_{x'}I &= I_0\left[\tfrac{3}{2}p_x K_x^{x'} + \tfrac{3}{2}p_z K_z^{x'} + \tfrac{2}{3}p_{xy}K_{xy}^{x'} + \tfrac{2}{3}p_{yz}K_{yz}^{x'}\right] \\
p_{y'}I &= I_0\left[P^{y'} + \tfrac{3}{2}p_y K_y^{y'} + \tfrac{2}{3}p_{xz}K_{xz}^{y'} + \tfrac{1}{3}\left(p_{xx}K_{xx}^{y'} + p_{yy}K_{yy}^{y'} + p_{zz}K_{zz}^{y'}\right)\right] \\
p_{z'}I &= I_0\left[\tfrac{3}{2}p_x K_x^{z'} + \tfrac{3}{2}p_z K_z^{z'} + \tfrac{2}{3}p_{xy}K_{xy}^{z'} + \tfrac{2}{3}p_{yz}K_{yz}^{z'}\right] \\
p_{x'y'}I &= I_0\left[\tfrac{3}{2}p_x K_x^{x'y'} + \tfrac{3}{2}p_z K_z^{x'y'} + \tfrac{2}{3}p_{xy}K_{xy}^{x'y'} + \tfrac{2}{3}p_{yz}K_{yz}^{x'y'}\right] \\
p_{y'z'}I &= I_0\left[\tfrac{3}{2}p_x K_x^{y'z'} + \tfrac{3}{2}p_z K_z^{y'z'} + \tfrac{2}{3}p_{xy}K_{xy}^{y'z'} + \tfrac{2}{3}p_{yz}K_{yz}^{y'z'}\right] \\
p_{x'z'}I &= I_0\left[P^{x'z'} + \tfrac{3}{2}p_y K_y^{x'z'} + \tfrac{2}{3}p_{xz}K_{xz}^{x'z'} + \tfrac{1}{3}\left(p_{xx}K_{xx}^{x'z'} + p_{yy}K_{yy}^{x'z'} + p_{zz}K_{zz}^{x'z'}\right)\right] \\
p_{x'x'}I &= I_0\left[P^{x'x'} + \tfrac{3}{2}p_y K_y^{x'x'} + \tfrac{2}{3}p_{xz}K_{xz}^{x'x'} + \tfrac{1}{3}\left(p_{xx}K_{xx}^{x'x'} + p_{yy}K_{yy}^{x'x'} + p_{zz}K_{zz}^{xx'}\right)\right] \\
p_{y'y'}I &= I_0\left[P^{y'y'} + \tfrac{3}{2}p_y K_y^{y'y'} + \tfrac{2}{3}p_{xz}K_{xz}^{y'y'} + \tfrac{1}{3}\left(p_{xx}K_{xx}^{y'y'} + p_{yy}K_{yy}^{y'y'} + p_{zz}K_{zz}^{y'y'}\right)\right] \\
p_{z'z'}I &= I_0\left[P^{z'z'} + \tfrac{3}{2}p_y K_y^{z'z'} + \tfrac{2}{3}p_{xz}K_{xz}^{z'z'} + \tfrac{1}{3}\left(p_{xx}K_{xx}^{z'z'} + p_{yy}K_{yy}^{z'z'} + p_{zz}K_{zz}^{z'z'}\right)\right]
\end{aligned}
\qquad (3.12)
$$

The observables may vary between limits imposed by the form of their defining operators or products of operators taken separately. Table 3.1 shows the corresponding range of values constraining each observable.

Polarizations	Analyzing Powers	Polarization Transfer Coefficients	Limits
$P^{y'}$	A_y	$K_y^{y'}, K_x^{x'}, K_z^{z'}, K_x^{z'}, K_z^{x'}$	± 1
$P^{x'z'}$	A_{xz}	$K_y^{x'z'}, K_x^{y'z'}, K_z^{x'y'}, K_x^{x'y'}, K_z^{x'y'}, K_{xy}^{x'}, K_{xy}^{z'}, K_{xz}^{y'}, K_{yz}^{x'}, K_{yz}^{z'}$	$\pm\frac{3}{2}$
		$K_y^{x'x'}, K_y^{y'y'}, K_y^{z'z'}, K_{xx}^{y'}, K_{yy}^{y'}, K_{zz}^{y'}$	± 2
		$K_{xy}^{x'y'}, K_{xy}^{y'z'}, K_{xz}^{x'z'}, K_{yz}^{x'y'}, K_{yz}^{y'z'}$	$\pm\frac{9}{4}$
		$K_{xx}^{x'z'}, K_{yy}^{x'z'}, K_{zz}^{x'z'}, K_{xz}^{x'x'}, K_{xz}^{y'y'}, K_{xz}^{z'z'}$	± 3
$P^{x'x'}, P^{y'y'}, P^{z'z'}$	A_{xx}, A_{yy}, A_{zz}		$+1\ -2$
		$K_{xx}^{x'x'}, K_{xx}^{y'y'}, K_{xx}^{z'z'}, K_{yy}^{x'x'}, K_{yy}^{y'y'} K_{yy}^{z'z'}, K_{zz}^{x'x'}, K_{zz}^{y'y'}, K_{zz}^{z'z'}$	$+4\ -2$

Table 3.1 - Limits on the range for spin 1 polarization observables.

3.3 Deuteron Polarization Analyzers

Techniques for Polarization Analyzers

When a deuteron beam is produced in a polarized-ion source with a unique magnetic-field direction, Z, the direction of its spin quantitization axis is along this Z axis. The beam also has an axial symmetry about the Z axis, so X and Y are arbitrary. Hence, a description of its polarization state is simplified to four quantities. First, one must know the direction of the spin axis, which can be oriented arbitrarily using a Wien filter. This axis is given by the angles β and ϕ defined in Figure 3.1. One must also know the relative populations of substates $m = 0,\pm1$. If N_1, N_{-1} and N_0 are the relative fractions of the beam in these states, then the vector and tensor components of the beam are given by the relations

$$p_Z = N_1 - N_{-1} \qquad p_{ZZ} = N_1 + N_{-1} - 2N_0 \ , \tag{3.13}$$

and all other polarization moments are zero. All of the polarization moments for the incident beam at the target are functions of these four quantities β, ϕ, p_Z and p_{ZZ} [Ohl72a]:

$$\begin{aligned} p_x &= p_Z \sin\phi\sin\beta & p_{xx} &= \tfrac{1}{2}p_{ZZ}(3\sin^2\phi\sin^2\beta - 1) \\ p_y &= p_Z \cos\phi\sin\beta & p_{yy} &= \tfrac{1}{2}p_{ZZ}(3\cos^2\phi\sin^2\beta - 1) \\ p_z &= p_Z \cos\beta & p_{zz} &= \tfrac{1}{2}p_{ZZ}(3\cos^2\beta - 1) \\ & & p_{xy} &= -\tfrac{3}{2}p_{ZZ}\sin^2\beta\cos\phi\sin\phi \\ & & p_{xz} &= -\tfrac{3}{2}p_{ZZ}\sin\beta\cos\beta\,\sin\phi \\ & & p_{yz} &= \tfrac{3}{2}p_{ZZ}\sin\beta\cos\beta\,\cos\phi \end{aligned} \tag{3.14}$$

When the deuteron beam is scattered, however, the initial symmetry may be

lost because of the interaction. Now, all the polarization moments of the scattered beam must be determined individually[5]. This of course can be done via a second scattering (analyzing) reaction and measurement of the asymmetry of counts between appropriately placed detectors. These asymmetries are generated by the azimuthal dependence of the polarized-beam cross section. From Eqn. 3.14, one can deduce the general azimuthal dependence of the cross section. If one considers the S´ frame and defines the azimuthal angle ϕ' analogously with ϕ in the incident frame and defines θ' as the angle of a second scattering interaction, then,

$$I(\theta',\phi') = I_0(\theta')[1 + A + B\sin\phi' + C\cos\phi' + D\sin2\phi' + E\cos2\phi'] . \qquad (3.15)$$

When written in terms of the the scattered beam polarizations ($p_{i'}$ and $p_{i'j'}$) and analyzing powers for the second interaction Eqn. 3.15 takes the form:

$$\begin{aligned} I(\theta',\phi') = I_0(\theta')[1 &+ \tfrac{3}{2}(p_{x'}\sin\phi' + p_{y'}\cos\phi')A_y(\theta') \\ &+ \tfrac{2}{3}(p_{x'z}\cos\phi' - p_{y'z}\sin\phi')A_{xz}(\theta') \\ &+ \tfrac{1}{6}\{(p_{x'x'} - p_{y'y'})\cos2\phi' - 2p_{x'y'}\sin2\phi'\}\{A_{xx}(\theta') - A_{yy}(\theta')\} \\ &+ \tfrac{1}{2}p_{z'z'}A_{zz}(\theta')]. \end{aligned} \qquad (3.16)$$

Now, defining cross sections L, R, U and D (using Eqn. 3.15) as scattering to the left (+x' direction; $\phi' = 0°$), right (-x' direction; $\phi' = 180°$), up (+y' direction; $\phi' = 90°$) and down (-y' direction; $\phi' = 270°$) one can define three asymmetries:

$$A1 = \frac{2(L-R)}{L+R+U+D} = \frac{\frac{3}{2}p_{y'}A_y + \frac{2}{3}p_{x'z'}A_{xz}}{1 + \frac{1}{2}p_{z'z'}A_{zz}}$$

[5] There are a total of seven independent moments: two vector and five tensor.

$$A2 = \frac{2(U-D)}{L+R+U+D} = \frac{-\frac{3}{2}p_x A_y + \frac{2}{3}p_{y'z'}A_{xz}}{1 + \frac{1}{2}p_{z'z'}A_{zz}}$$

$$A3 = \frac{(L+R)-(U+D)}{L+R+U+D} = \frac{\frac{1}{3}(p_{x'x'} - p_{y'y'})(A_{xx} - A_{yy})}{1 + \frac{1}{2}p_{z'z'}A_{zz}}. \qquad (3.17)$$

Rotation of the four detectors about the z' axis by an angle of 45° (giving L', R', U' and D' for $\phi' = 45°,225°,135°,315°$ respectively) changes the form of the asymmetry $A3$. In this configuration then

$$A3' = \frac{(L'+R')-(U'+D')}{L'+R'+U'+D'} = \frac{\frac{1}{6}p_{x'y'}(A_{xx} - A_{yy})}{1 + \frac{1}{2}p_{z'z'}A_{zz}}. \qquad (3.18)$$

If one adds a detector at $\theta' = 0°$, its yield is an azimuthally independent quantity, and an additional cross section B can be defined: $B = B_0[1 + \frac{1}{2}p_{z'z'}A_{zz}]$. An additional asymmetry may be generated with the form,

$$A4 = \frac{\Sigma}{B} = \left(\frac{\Sigma_0}{B_0}\right) \cdot \frac{1 + \frac{1}{2}p_{z'z'}A_{zz}(\theta')}{1 + \frac{1}{2}p_{z'z'}A_{zz}(0°)}, \qquad (3.19)$$

where $\Sigma = L + R + U + D$ and Σ_0/B_0 is the ratio of unpolarized cross sections at angles $\theta'$and at 0°.

Polarization transfer measurements for deuterons

There are several observations to be made at this point. First, in order to completely determine the scattered-beam polarization state one would need an additional set of L,R,U,D detectors at a different scattering angle. This would allow

the separate determination of the $p_{y'}$, $p_{x'z'}$ and of $p_{x'}$, $p_{y'z'}$ moments in the ratios A1 and A2. Therefore, a minimum of eight detectors plus one detector rotation (of $\phi' = 45°$) would be needed. Addition of a 0° detector (B) would allow a supplemental determination of $p_{z'z'}$. The polarimeter we designed for the present work has only five detectors (L,R,U,D at $\theta' = 25°$ and B). We have, therefore, sacrificed the complete description for compactness and simplicity. This compromise, however, is not particularly harsh. As was stated previously, along with cross section and analyzing powers a complete determination of all scattering amplitudes can be made with the measurement of two (properly chosen) PTO. This requires a maximum of only two outgoing moments which must be measured. Anything more provides only redundant information for consistency checks.

One of the stated goals for this work was to use polarization transfer measurements to provide better information about the deuteron-nucleus tensor interaction. Given this then we needed to find specific PTO which could provide the most interesting information. To these ends $K_y^{z'z'}$ was found to be a good observable (details on this determination are in section 3.4). In order to determine $K_y^{z'z'}$ only the outgoing polarization moment $p_{z'z'}$ must be measured. The expression which relates this moment with the incoming vector and tensor polarizations comes from Eqn. 3.12, namely;

$$p_{z'z'}I = I_0\left[P^{z'z'} + \frac{3}{2}p_y K_y^{z'z'} + \frac{2}{3}p_{xz}K_{xz}^{z'z'} + \frac{1}{3}\left(p_{xx}K_{xx}^{z'z'} + p_{yy}K_{yy}^{z'z'} + p_{zz}K_{zz}^{z'z'}\right)\right] \qquad (3.20)$$

where I and I_0 are the polarized and unpolarized cross sections for the initial reaction. The polarization function $P^{z'z'}$ is the outgoing tensor polarization along the z' axis and is equal to A_{zz} in the center-of-mass frame for elastic scattering. In a typical double-scattering experiment Eqn. 3.20 will be simplified, based on knowledge of the incident

beam direction and polarization. If we orient the spin along the y axis and if the beam is both vector and tensor polarized then, substituting from Eqn. 3.14, expression 3.20 becomes

$$p_{z'z'}I = I_0\left[P^{z'z'} + \tfrac{3}{2}p_Z K_y^{z'z'} + \tfrac{1}{2}p_{ZZ}K_{yy}^{z'z'}\right] \qquad (3.21)$$

Coupling this equation with the equation for polarized cross section (also from Eqn. 3.12)

$$I = I_0\left[1 + \tfrac{3}{2}p_Z A_y + \tfrac{1}{2}p_{ZZ}A_{yy}\right] \qquad (3.22)$$

allows determination of both $K_y^{z'z'}$ and $K_{yy}^{z'z'}$ independent of cross section measurements, assuming that for a given scattering angle θ the outgoing polarization moment $p_{z'z'}$ has been measured in a polarimeter via the asymmetry $A4$, the incident beam polarizations are continuously monitored, and that the analyzing powers A_y, A_{yy} and $P^{z'z'}$ have been previously determined for the particular reaction.

The above descriptions are in a general form. So, in an analogous manner for any outgoing polarization moment measured any of the associated PTO can be determined depending on the incident beam polarization and spin orientation. A more complete description of the present PTO experiment will be given in Chapters IV and V.

3.4 The scattering matrix and polarization observables

The transition matrix for elastic scattering

In section 3.2 we defined the relationship between the scattered beam polarization state (ρ_f) and its initial state (ρ_i) through introduction of the 3×3 scattering matrix $M(E,\theta)$. From this relation all the polarization observables can be written as a linear combination of products of the scattering matrix amplitudes (Eqn. 3.11). It is a useful exercise to take a closer look at the relationship between these amplitudes and observables in order to understand why some observables are more sensitive to particular potentials in the optical model. Just as important is the determination of which PTO actually provide new information not available from analyzing power and cross section measurements.

The scattering matrix can take several forms. In general, it can be written as a linear combination of any complete set of 3×3 matrices. It is particularly useful here to expand it in terms of the irreducible spherical tensor operators for spin 1 (analogous to Eqn. 3.6). Then, [Lop77]

$$M(E,\theta) = \sum_{kq} M_{kq}\tau^{\dagger}_{kq} = \begin{pmatrix} M_{00}+\sqrt{\frac{1}{2}}M_{20} & \sqrt{\frac{3}{2}}(M_{11}-M_{21}) & \sqrt{3}M_{22} \\ -\sqrt{\frac{3}{2}}(M_{11}+M_{21}) & M_{00}-\sqrt{2}M_{20} & \sqrt{\frac{3}{2}}(M_{11}+M_{21}) \\ \sqrt{3}M_{22} & -\sqrt{\frac{3}{2}}(M_{11}-M_{21}) & M_{00}+\sqrt{\frac{1}{2}}M_{20} \end{pmatrix} \tag{3.23}$$

Inversion of Eqn. 3.23 gives the scattering amplitudes:

$$M_{kq} = \frac{1}{3}\mathrm{Tr}(M(E)\cdot\tau_{kq}). \tag{3.24}$$

While this form of the matrix is general for any frame where the y axis is parallel to

$\boldsymbol{k}_{in}\times\boldsymbol{k}_{out}$, values of the amplitudes are dependent on the specific reference frame. For consistency, the above matrix will be said to be in the S (incident) frame. One of the advantages of this form for the scattering matrix is that the amplitudes behave like spherical tensors under rotations (i.e. elements of order k=0,1,2 preserve their order under rotations). In addition, these elements exhibit the same properties as the τ_{kq} when symmetry restrictions are imposed. For instance, parity manifests itself through the relation, $M_{kq} = (-1)^{k+q}M_{k-q}$.

Time-reversal invariance in general provides a relation between the M_{2q}. However, the exact form of this relation is dependent on the reference frame used. It takes a particularly simple form when M is rotated into the center-of-mass frame. In this case we make a counter-clockwise (+) rotation of M by θ_{cm} and we obtain

$$M'(\mathrm{CM}) = d^{(1)}(\theta_{cm})M \quad , \tag{3.25}$$

where $d^{(1)}(\theta_{cm})$ is the rank-1 reduced rotation matrix (see Appendix C). In this frame, invariance under the time-reversal transformation requires that $M'_{21} = 0$ in order for $M(\boldsymbol{k}_{out},\boldsymbol{k}_{in},\mathrm{S}) = M(-\boldsymbol{k}_{in},-\boldsymbol{k}_{out},-\mathrm{S})$. Since the amplitudes rotate like spherical tensors of rank k then $\{M'_{2q}\} = d^{(2)}(\theta_{cm})\{M_{2q}\}$, thus

$$M'_{21} = M_{21}\cos\theta_{cm} + \sqrt{\tfrac{3}{8}}\,M_{20}\sin\theta_{cm} - \tfrac{1}{2}M_{22}\sin\theta_{cm} = 0. \tag{3.26}$$

As a result, in the incident reference frame the time reversal constraint takes the form,

$$M_{21} = \tfrac{1}{2}\left[M_{22} - \sqrt{\tfrac{3}{8}}M_{20}\right]\tan\theta_{cm} \ . \tag{3.27}$$

Reference frames for observables

The exact forms of the rotation matrices are given in Appendix C. They can be used to rotate the scattering matrix or the individual amplitudes. Relationships between the observables defined in different reference frames can also be made. This is particularly important in the calculation of PTO because in principle they are not "in" any reference frame but rather they connect two different frames. While there are various methods of calculating the PTO from the relations given in Eqn. 3.11, two methods are particularly straight forward. The first method involves the calculation of PTO in the incident frame S. For example,

$$K_y^{zz}(\theta) = \frac{\mathrm{Tr}(MS_yM^\dagger S_{zz})}{\mathrm{Tr}(MM^\dagger)} \tag{3.28}$$

relates the polarization moment p_y to p_{zz} in the same incident frame. One can then make a rotation of the S frame PTO to the scattered frame S´ (CM or lab). The PTO connecting p_y in the incident frame to $p_{z'z'}$ in the scattered frame is then given by (see Appendix C)

$$K_y^{z'z'} = K_y^{zz}\cos^2\theta + K_y^{xx}\sin^2\theta + K_y^{xz}\sin 2\theta, \tag{3.29}$$

where θ is either the CM or lab scattering angle. A second method for calculating $K_y^{z'z'}$ directly requires the rotation of the scattering matrix into the appropriate outgoing frame. For M' defined in Eqn. 3.25 we can write

$$K_y^{z'z'}(\theta) = \frac{\mathrm{Tr}(MS_yM^\dagger S_{z'z'})}{\mathrm{Tr}(MM^\dagger)} \tag{3.30}$$

where again θ can be either the CM or lab scattering angle.

There are several useful identities for the observables when the scattering matrix is in the CM frame:

$$P^{ij}(\theta_{cm}) = (-1)^{N_x} A_{ij}(\theta_{cm}) \qquad \text{(polarization = } \pm\text{analyzing power)}$$
$$K_{ij}^{l'm'}(\theta_{cm}) = K_{lm}^{i'j'}(\theta_{cm}). \tag{3.31}$$

However, actual measurement of observables takes place in the laboratory frame. In this frame the relations of Eqn. 3.31 do not hold, but we can make use of them indirectly. Take for example the measurement of $K_y^{z'z'}(\theta_{lab})$ as outlined in section 3.3. One must know the polarization function $P^{z'z'}(\theta_{lab})$ for the reaction. We can write this function as a linear combination of the $P^{i'j'}(\theta_{cm})$ (analogously with Eqn. 3.29) giving,

$$P^{z'z'}(\theta_{lab}) = P^{z'z'}(\theta_{cm})\cos^2\delta + P^{x'x'}(\theta_{cm})\sin^2\delta - P^{x'z'}(\theta_{cm})\sin 2\delta, \tag{3.32}$$

where $\delta = \theta_{cm} - \theta_{lab}$. Substituting Eqn. 3.31 we get,

$$P^{z'z'}(\theta_{lab}) = A_{zz}(\theta_{cm})\cos^2\delta + A_{xx}(\theta_{cm})\sin^2\delta + A_{xz}(\theta_{cm})\sin 2\delta. \tag{3.33}$$

Hence, for deuteron elastic scattering the polarization functions are just linear combinations of the analyzing powers . In the case of scattering from heavy nuclei the difference between center-of-mass and lab frames is very small and can often be neglected (i.e. $P^{z'z'}(\theta_{lab}) \approx A_{zz}(\theta_{lab})$) particularly at forward angles where analyzing powers are in general quite small.

Sensitivity of the optical potential to polarization observables

For the optical model potential the spin dependent forces are very weak relative to the central interaction, so one can in principle treat the spin-dependent terms perturbatively in evaluating the transition matrix for elastic scattering. Hooten and Johnson showed [Hoo71] that by doing this one can derive some general results about the sensitivity of the M_{kq} to the different optical model potential components.

We expand the optical model potential as

$$V = V_C + V_{sd} = \sum_{kq} V_{kq} \tau^{\dagger}_{kq} , \tag{3.34}$$

where $V_C = V_{00}$ is the central part and V_{sd} is the spin-dependent part of the interaction. The $k = 1,2$ terms then correspond to the spin-orbit and tensor potentials respectively. A scattering matrix between plane-wave states, ϕ, is written to first order in V_{sd} as

$$\begin{aligned} <\phi(\mathbf{k}_{out},\mathbf{S}')|M|\phi(\mathbf{k}_{in},\mathbf{S})> &= <\phi(\mathbf{k}_{out},\mathbf{S}')|M_C|\phi(\mathbf{k}_{in},\mathbf{S})> \\ &+ <\psi_c^{(-)}(\mathbf{k}_{out},\mathbf{S}')|V_{sd}|\psi_c^{(+)}(\mathbf{k}_{in},\mathbf{S})> + \text{...(higher order in } V_{sd}). \end{aligned} \tag{3.35}$$

Here M_C is the spin independent term corresponding to V_C and $|\psi_c^{(\pm)}(\mathbf{k},\mathbf{S})>$ represents the distorted waves generated by this unperturbed potential. If one takes this wave function to be separable in the form $|\psi_c^{(\pm)}(\mathbf{k},\mathbf{S})> = |\chi_c^{(\pm)}(\mathbf{k})>|1\mathrm{m}>$ where $|1\mathrm{m}>$ represents the internal deuteron wave function in spin substate m, then to first order in V_{sd} the following approximations can be made:

$$\begin{aligned} M_{00} &\approx <\phi(\mathbf{k}_{out},\mathbf{S}')|M_C|\phi(\mathbf{k}_{in},\mathbf{S})> \\ M_{kq} &\approx <\chi_c^{(-)}(\mathbf{k})|V_{kq}|\chi_c^{(+)}(\mathbf{k})> \qquad k\neq 0 . \end{aligned} \tag{3.36}$$

By writing the scattering matrix as an expansion of spherical tensor operators for spin-1, we see a correspondence of the different order amplitudes (k=0,1,2) to the presence of the central, vector and tensor forces respectively in the deuteron-nucleus interaction. In general therefore, observables which include terms involving the M_{2q} should exhibit the most sensitivity to the tensor interaction. It should be noted also that M_{00} being associated with the central interaction is also considerably larger than the other amplitudes and when present it will strongly influence the form of the observable. It is advisable therefore to look for terms involving products such as $M_{00}M^{*}_{2q}$. These terms effectively enhance the sensitivity of an observable to the tensor interaction.

When writing out the expansion of observables in terms of matrix-element products, the exact form will depend on the reference frame in which the matrix and operators are defined; however, because the M_{kq} behave like spherical tensors under rotations, they remain simple linear combinations of the same order elements. Hence, observations in the preceding paragraph remain true in any reference frame. With this in mind, it can be shown [Hoo71] that for the polarized single scattering observables the dominant terms in their expansion (in terms of matrix amplitudes) are:

$$\begin{aligned}
\frac{d\sigma(\theta)}{d\Omega} &\propto |M_{00}|^2 + \{\, |M_{kq}|^2 \,\} \qquad (k\neq 0)\\
A_y(\theta) &\propto \mathrm{Im}(M_{00}M^{*}_{11})\\
A_{xx}(\theta);A_{yy}(\theta);A_{zz}(\theta) &\propto \mathrm{Re}(M_{00}M^{*}_{2q})\\
A_{xz}(\theta) &\propto \mathrm{Re}(M_{11}M^{*}_{2q}).
\end{aligned} \tag{3.37}$$

It is clear from these expansions that the tensor analyzing powers will provide the

strongest sensitivity to the tensor interaction. In fact, of the four analyzing powers A_{xz}, while being very small, shows the strongest sensitivity to the presence of a tensor potential. This is because additional terms in the other TAP complicate the correspondence to individual potentials, while A_{xz} has only terms involving M_{2q}.

Polarization transfer observables

What one would like to gain from polarization transfer measurements is new information about the scattering matrix as well as sensitivity to the tensor interaction. Given the driving terms in Eqn. 3.37, the most obvious choice is to look for a PTO with terms involving $\mathrm{Im}(M_{00}M^*_{2q})$. One PTO which has such terms is $K_y^{z'z'}$. We can expand this observable in terms of the S frame scattering amplitudes by substituting the relations for K_y^{zz}, K_y^{xx} and K_y^{xz} (Eqn. 3.11) into Eqn. 3.29. The final expression is then

$$K_y^{z'z'} = \frac{1}{\Sigma}[\ -2\sqrt{3}\,\mathrm{Im}(M_{00}M^*_{11}) + 6\sqrt{3}\,\mathrm{Im}(M_{00}M^*_{21}) + 6\,\mathrm{Im}(M_{11}M^*_{22}) + 5\sqrt{6}\,\mathrm{Im}(M_{20}M^*_{11}) - 6\sqrt{6}\,\mathrm{Im}(M_{20}M^*_{21})\ ], \tag{3.38}$$

where

$$\Sigma = 3[\ |M_{00}|^2 + |M_{20}|^2 + 2|M_{11}|^2 + 2|M_{21}|^2 + 2|M_{22}|^2\ ]. \tag{3.39}$$

The term $6\sqrt{3}\,\mathrm{Im}(M_{00}M^*_{21})$ is in fact the dominant term in the expansion when its coefficient is included. The other term of consequence is $\mathrm{Im}(M_{00}M^*_{11})$. It is the same driving term in the expression for the vector analyzing power A_y and is a significant contributor to the form of $K_y^{z'z'}$. We can remove this spin-orbit sensitivity by looking at the observable combination $K_y^{z'z'} - 1/2A_y$ which from here on will be called K_1 for convenience. An example of an optical model calculation for both $K_y^{z'z'}$ and K_1 are

shown in Figure 3.2 with and without a T_r-type tensor potential. One can easily notice that the term $\mathrm{Im}(M_{00}M_{11}^{*})$ generating the large oscillations in $K_y^{z'z'}$ are removed in the observable K_1. Details of the calculations will be discussed in Chapter VI.

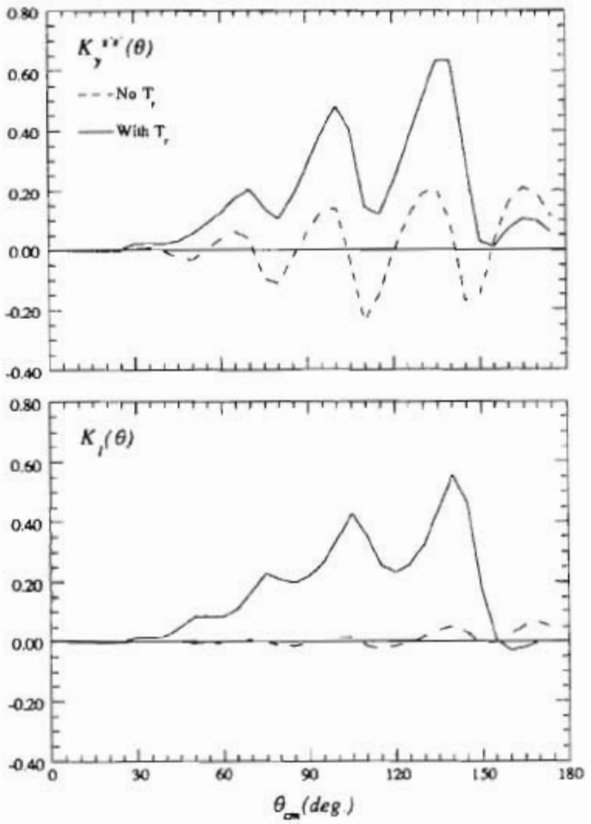

Figure 3.2 - Optical model calculations of PTO for $^{90}Zr(d,d)^{90}Zr$ at 15 MeV. Potentials used come from [God78].

It is useful to define two other PTO-analyzing power observable combinations which are important depending on which measurement scheme is used. Using Eqns. 3.21 and 3.22, if the incident deuteron beam is purely vector polarized then only A_y, $K_y^{z'z'}$ and K_1 can be measured. If the beam is purely tensor polarized, then A_{yy}, $K_{yy}^{z'z'}$ and $K_2 \equiv K_{yy}^{z'z'} + 1/2A_{yy}$ can be measured. K_2 is also sensitive to the tensor interaction but it is very small. Finally, if the incident beam is both vector and tensor polarized with $p_Z = p_{ZZ}$, then the PTO $3K_y^{z'z'} + K_{yy}^{z'z'}$ or the PTO-AP combination $K_A \equiv 3K_1 + K_2$ is measured, the latter having primarily sensitivity to the tensor interaction with the major spin-orbit contributions removed. Details of the measurement schemes for these observables will be given in Chapters IV and V.

Chapter IV

The Polarimeter

4.1 Polarimeter design

Polarimeters for polarization transfer

As we have seen in Chapter III, polarization analysis of a deuteron beam can be a complicated undertaking. When deuterons are produced with a polarized-ion source and the quantitization axis can be oriented as needed, the task of measuring the polarization state is simplified considerably. There have been, in the past, a number of *polarization monitors* designed to measure polarizations of an incident deuteron beam [God76, Ste80a, Ton80] during an experiment. However, once the beam has been scattered in some type of reaction wholly new considerations must be made for the beam polarization measurement. First, the flux of deuterons entering the *polarimeter* is reduced drastically compared to the primary beam, so its efficiency is of primary concern. In addition, there are a host of other experimental problems to overcome, depending on the type of experiment being done, and on how complete the determination of the scattered polarization state needs to be. Because of these problems, there have been only a few attempts at polarization transfer measurement with deuterons. For the tandem accelerator energy range (10-16 MeV) only a few polarimeters have been designed to make polarization measurements of scattered

deuterons [McI67, Mit73, Ste80b, Grü82, Ulb84, Grü87]. Most of these are quite specialized in their purpose and complex in design.

The present polarimeter differs in design from previous polarimeters in several ways. We have sacrificed the complete description of the scattered polarization state provided by the polarimeters of Grüebler *et al.* [Grü82,87] in order to make it significantly more compact and simpler to operate. These features allow the simultaneous use of two polarimeters during an experiment. The polarimeter described in [Mit73,Ohl72a] is similar in concept to the present design, but it requires degrading the energy of the scattered deuteron beam to reach the S-wave $3/2^+$ resonance of the $^3He(d,p)^4He$ reaction at 430 keV. The increased cross section at this energy helps attain a higher efficiency. We have avoided this beam degradation in the present design to allow more flexibility in the energy range in which it can be used and in principle to avoid the loss of vector polarization information which occurs with low-energy S-wave deuterons.

Reaction choice and design considerations

At low energies (<30 MeV) there are notably only two scattering reactions used as secondary polarization standards in the measurement of deuteron beam polarizations. They are $^4He(\vec{d},d)^4He$ elastic scattering and the $^3He(\vec{d},p)^4He$ reaction. Both have been extensively studied at a range of energies, and angular distributions of all the analyzing powers have been measured with reasonable accuracy [Grü71,75,79, Har72, Ohl73, Bro78, Ton80]. In the case of double scattering (polarization transfer) experiments, however, all the studies to date have used the $^3He(\vec{d},p)^4He$ reaction. While its cross section is smaller than that for elastic scattering, the loss in efficiency is compensated by its very large Q-value

(18.35 MeV). This provides the invaluable discrimination of resulting protons from the large number of low energy background sources present in these low count rate experiments. In addition, both the tensor and vector analyzing powers are relatively large over a wide energy range. Finally, because of the large Q-value, the incident deuterons can be stopped before reaching the detector while (d,p) protons can easily be detected.

Based on the reaction choice, we designed a high pressure ^{3}He gas cell to increase the effective analyzer target thickness. We also extended the active length of the gas cell utilizing a vane-type design to collimate the protons for the appropriate scattering angle. A cross section of the entire polarimeter assembly including gas cell and detectors is pictured in Figure 4.1.

The gas cell itself was constructed from a single rectangular block of aluminum (11 cm×4.5 cm×4.5 cm). It was bored out down the center and on each side to allow insertion of four vane collimators and one 0° collimator. With the 0° degree collimator in place this gives an effective gas cell length of 6.1 cm. The cell has been designed to hold very high pressures of ^{3}He (up to 30 atm). This required the use of relatively thick window foils particularly for the four large side exit windows. For each of the five exit windows, 6 mil (0.1524 mm) stainless steel (SS) foils were used. The purpose of these foils was two-fold; first, they were adequate to withstand the high pressures but also they kept the elastic deuterons and other low energy reaction products from passing through into the detectors. For the entrance window a 2 mil (0.0508 mm) SS foil was used. This foil provided minimal degradation (<2 MeV) of incident deuterons while still holding pressures up to 30 atm[1].

Care had to be taken when sealing the gas cell for use at these pressures. We wanted these windows easily removable so no epoxy was used. Instead, 3 mm thick

---

[1] This was the highest pressure at which it was tested. No foil ever broke in the tests.

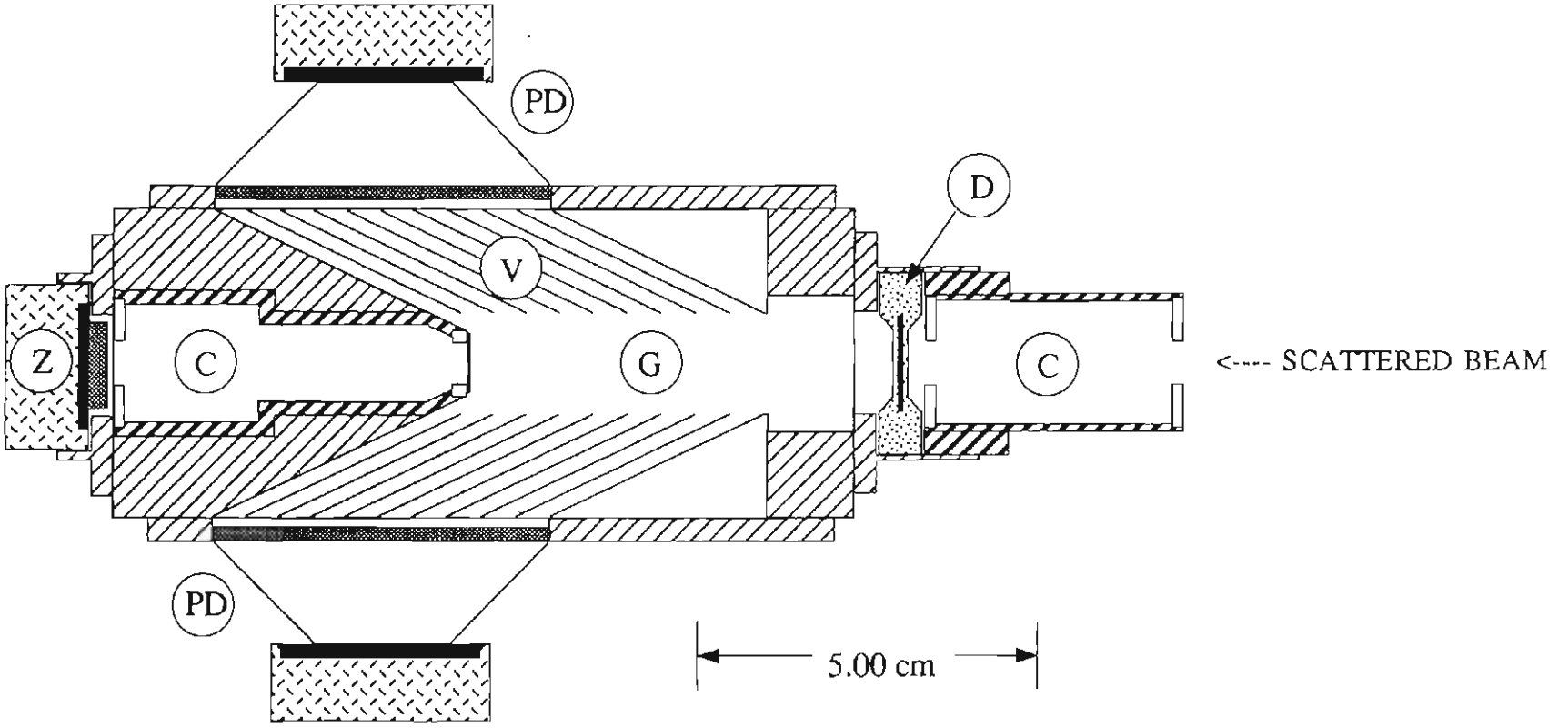

Figure 4.1 - Polarimeter Schematic: The polarimeter consists of a ^{3}He gas cell (G) collimated at 25° with tantalum vanes (V) into four CsI(Tl) detectors coupled to photodiodes (PD). The passing, ΔE (D), and 0° (Z) detector collimators are denoted by (C).

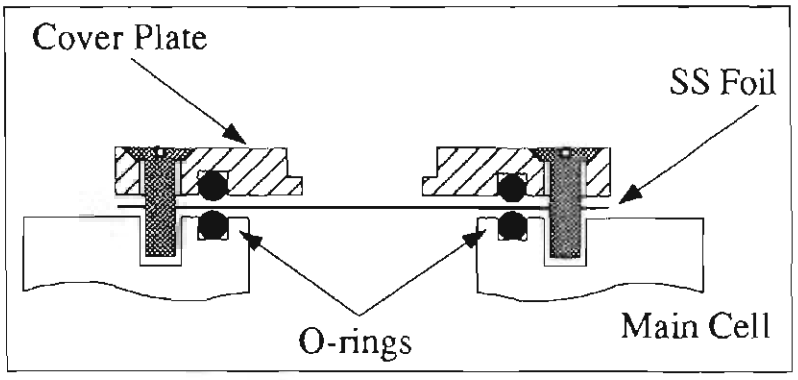

Figure 4.2 - Double O-ring seal for polarimeter exit windows

aluminum cover plates were used and screwed down on the cell block. Both the cover plate and the cell had O-ring seals. In this way the window foils were held in place with a double O-ring seal (see Figure 4.2). The O-ring on the cover plate simply provided extra pressure on the lower seal. Tests made without the second O-ring did not work at all for the higher pressures (> 7 atm). While at these higher pressures, ^{3}He gas slowly diffused out of the cell (≈2-5 psi/week). This was not the case for heavier gases like N_2. After 6-8 months under high pressure we noticed some loosening of the seals to the point where pressure had to be relieved and the seals remade.

To avoid tampering with the gas cell seals, we decided to leave detectors outside the cell, but to save space the detector collimators were placed inside the cell. Both the side vane collimators and the 0° collimator are removable, however. This was done to allow some flexibility in the use of the gas cell for different experiments. In principle, the vane collimators can be constructed for any angle between 25° and 90°. We chose 25° for two reasons. First, all the analyzing powers (A_y, A_{yy}, A_{xz} and A_{zz}) are at their largest at this angle in the energy range of interest. Second, the current polarization monitor used for incident deuteron measurements [Ton80] is also

calibrated at this angle[2] and could provide useful cross checks (see section 4.3).

The vane collimators consist of nine 0.368 mm thick tantalum vane elements. Protons passing through a single vane would not then be energetic enough to exit the cell window. The vane spacing allows for a maximum ±3.8° angular acceptance for the 25° detectors. The 0° collimator consists of two circular 1/4" diameter slits positioned on a 4.9 cm long barrel. This provides a maximum angular acceptance of 7.38° for the 0° detector. A tantalum foil on the front 0° circular slit stops the incident deuterons while allowing (d,p) protons to pass through.

Detector considerations

Most of the difficulty in a double scattering experiment comes from dealing with the small count rate due to the low efficiency of the polarimeter. So, in addition to using a high pressure extended gas cell we also wanted to place the polarimeter in close proximity to the target, preferably within the existing scattering chamber. This provides the largest solid angle for the polarimeter. It also, however, produces the largest possible background problems. At a result, the detectors used must not only have a large area (1×5 cm^2) but also must be capable of tolerating the high beam associated neutron and gamma fluxes for long periods of running time.

Based on these requirements, the use of silicon surface-barrier detectors was ruled out. The size and thickness requirements (>2000 μm) made detector costs too prohibitive. Silicon surface-barrier detectors are known to be highly susceptible to radiation damage from the high neutron fluxes in the chamber. Phototubes and traditional scintillators as alternative detectors proved to be too bulky. Hence, we chose to use fast response PIN-type silicon photodiodes in place of phototubes. We

---

[2] The monitor of [Ton80] was actually calibrated at 24.5° but its total angular acceptance fell within the range of the present polarimeter's larger acceptance.

coupled them to CsI(Tl) scintillators rather than plastics because the light output was better matched for the diodes. Side detectors were constructed from either two 10×10 mm^2 photodiodes (Hammamatsu model S1723-04) or a single 10×20 mm^2 photodiode (model S2344) coupled via a lucite light guide to a 50×10 mm^2 CsI(Tl) ($\approx$2 mm thick) crystal. For the 0° detector a single photodiode (S1723-04) coupled directly to 10×10 mm^2 crystal ($\approx$4 mm thick) was used. Given the construction of each of the detectors, the 0° detector gave better overall resolution because of better light collection efficiency. Typical energy resolution for these detectors was about 7-10% FWHM when measured with the 5.5 MeV alpha-particle peak in the decay of ^{241}Am (see Figure 4.3a,b).This resolution, given the analyzing reaction Q-value, was more than adequate for the purposes of the experiment. Note also in Figure 4.3a that the bare photodiodes are also sensitive to direct gamma-rays. This would prove to be a significant background contribution to overcome (see section 4.2).

We found it useful to add a sixth detector to the polarimeter. It was placed in front of the entrance window for the purpose of identifying the elastically scattered deuterons from the target. For this purpose a compact detector was needed with reasonably good resolution, hence we chose a 300 μm silicon transmission detector. It, of course, took a horrible beating and was somewhat count-rate limited ($\approx10^4$counts/sec), but it provided both the particle discrimination necessary and an additional timing coincidence requirement with each of the the other five detectors. Our experience was that a new passing ΔE detector would work uncooled for about 2 weeks of running time before poor resolution or breakdown made it unusable.

The gas cell and detectors are mounted on an isolated frame which is in turn mounted inside the scattering chamber. The entire polarimeter assembly (not including the 3.81 cm long entrance collimator) comprises a volume of only $12\times12\times12$ cm^3 (see Figure 4.4). This is very compact and allows the use of two such devices in the scattering chamber simultaneously.

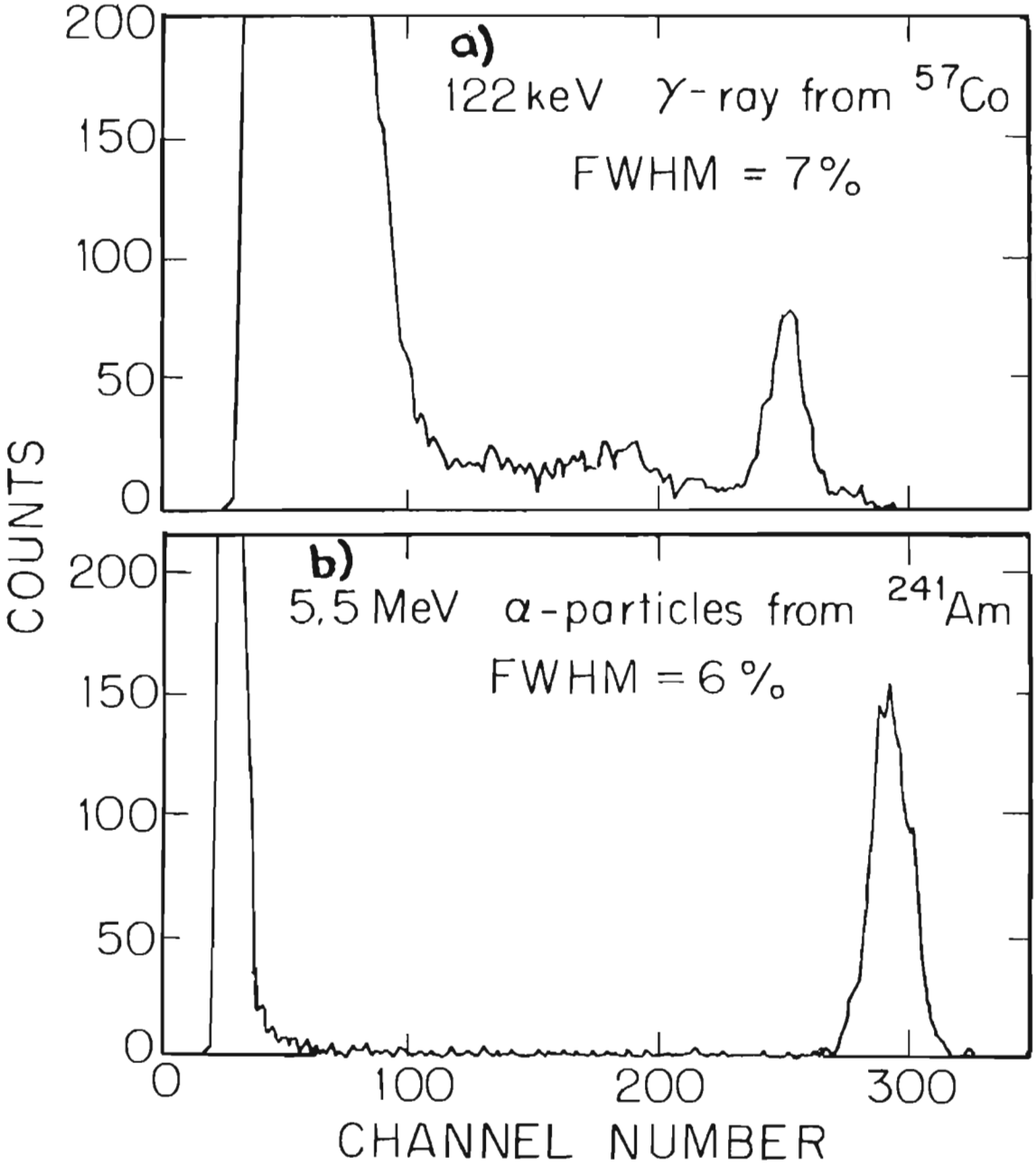

Figure 4.3 - Energy spectra from both a bare photodiode (a) and a photodiode coupled to a CsI(Tl) crystal (b).

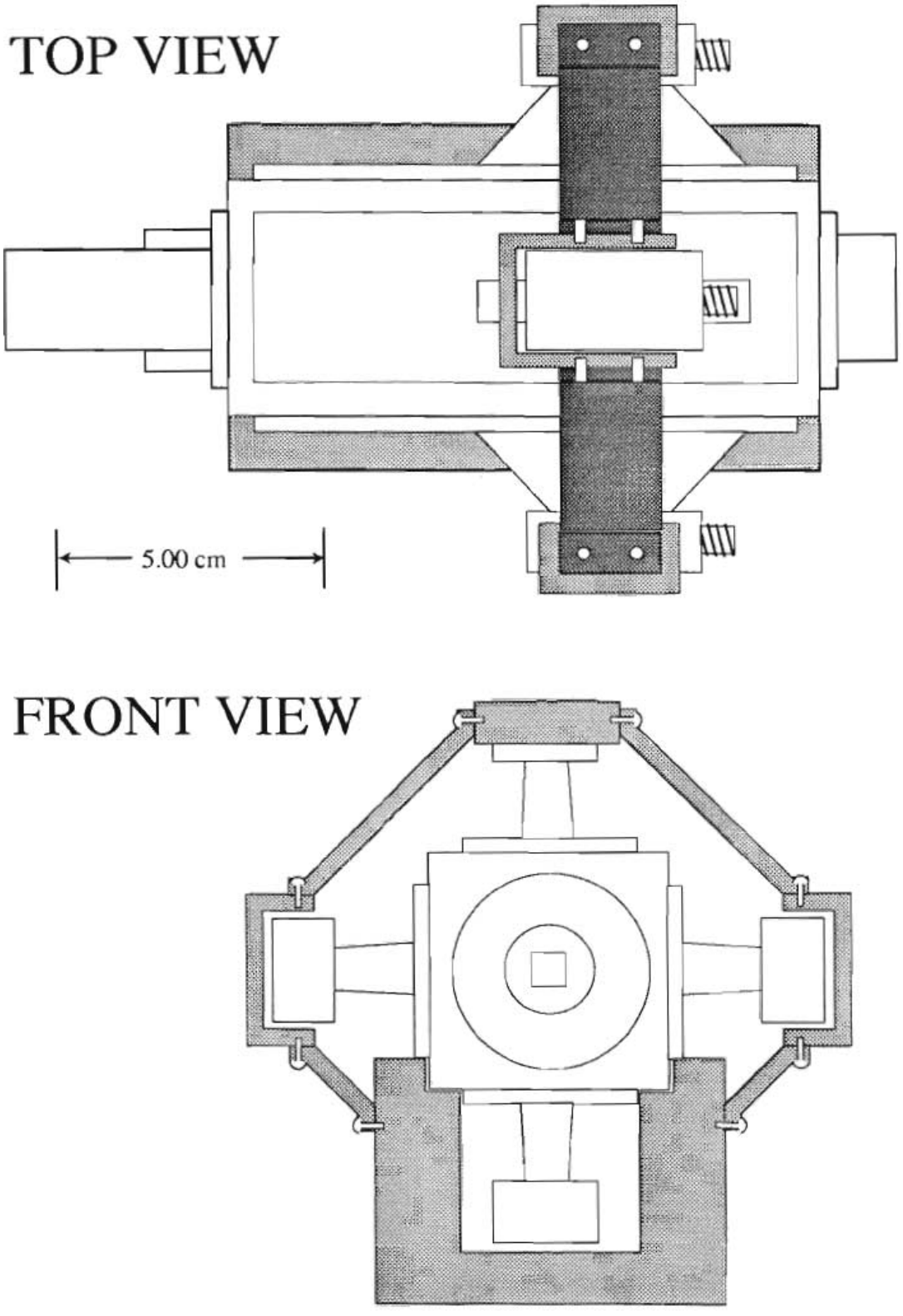

Figure 4.4 - Diagram of the complete polarimeter assembly.

4.2 Polarimeter operation and performance

We describe in this section the general experimental data acquisition techniques for polarization transfer measurements using the present polarimeters, while details of the experimental data and analysis are discussed in Chapter V. Figure 4.5 shows the general setup for a polarization transfer experiment with two polarimeters symmetrically placed left and right of the incident beam direction. The entrance collimators for each device consist of a square 0.635 cm slit placed 11.6 cm from the target, thus providing an angular acceptance for each polarimeter of ±1.57°. A polarization monitor downstream simultaneously measured the incident beam polarization.

During an experiment the major hurdle to overcome is the discrimination of $^3He(d,p)^4He$ protons from what seems at times an insurmountable background, and it involves the one drawback to our choice of detectors. The primary disadvantage of the photodiode/CsI detector is its sensitivity to the gamma rays present in the scattering chamber, not only from the CsI crystal but from direct interaction with the photodiodes as well. Unfortunately, while the $^3He(\vec{d},p)^4He$ protons deposit the largest energy in the scintillator, the signals from the gamma rays still show up as a continuum throughout the detector spectrum. To separate this gamma ray background from protons of interest we used the difference in the response of CsI(Tl) crystal to protons and gamma rays [Big61]. This pulse shape discrimination (PSD) proved to be a very effective way to improve identification of protons of interest. Figure 4.6 shows a schematic diagram of the electronics used in the operation of the polarimeters. Detector signals are accepted by a standard preamplifier (Ortec 142A) and sent to a fast timing amplifier (Ortec 442). Both the amplifier and preamplifier were located at the target chamber in order to bring in the owest noise signal possible. The amplified

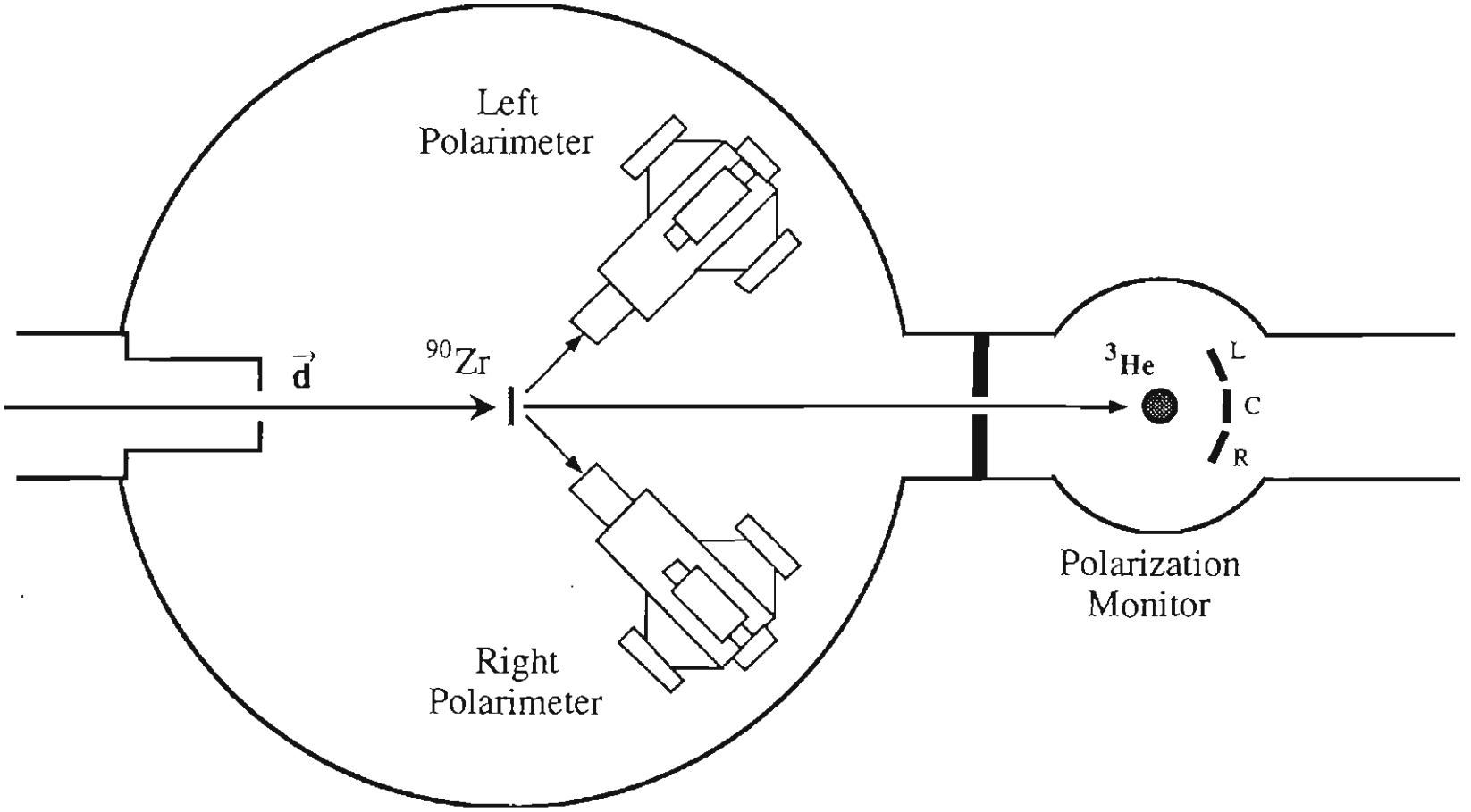

Figure 4.5 - Scattering chamber set-up for polarization transfer experiments.

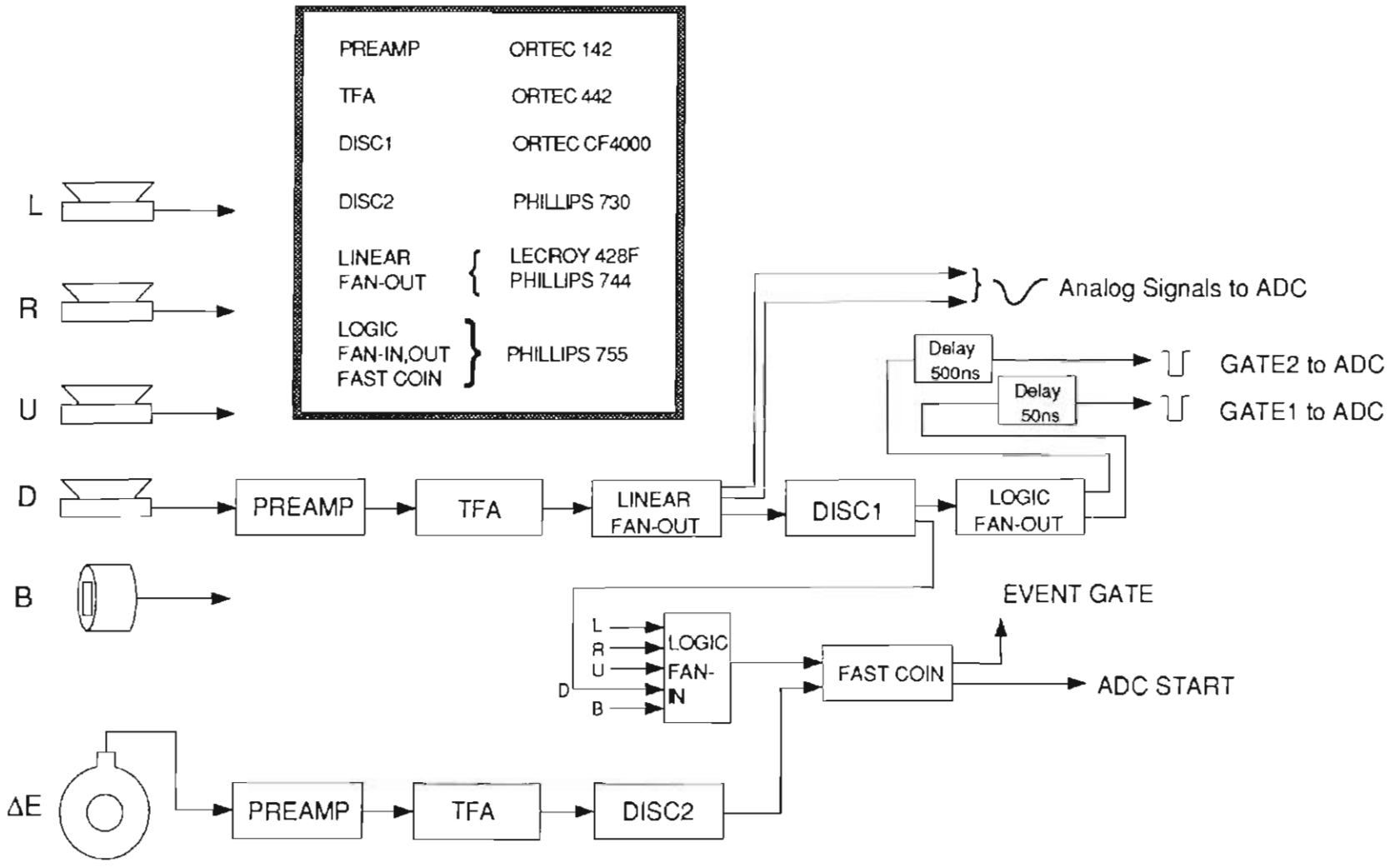

Figure 4.6 - Electronics schematic for polarization transfer data acquisition.

lsignal then provided both the energy information and PSD information. The ΔE detector signal was processed by a similar amplifier and then fed into a leading edge discriminator with both upper and lower thresholds (Phillips 730). In this manner the photodiode/CsI detectors could be gated with ΔE detector signals by setting up a window corresponding exclusively to elastically scattered deuterons.

The heart of the signal processing is the PSD electronics. A LeCroy single-gated ADC (Model 2249SG) accepts on two separate inputs identical fast analog signals from a linear fan-out fed by the fast amplifier. Each of these pulses is gated at different times with respect to the leading edge of the pulse, approximately 500 ns apart (see Figure 4.7). The ADC then digitizes the analog signals for a time equal to the width of each gate. The two digitized energy signals for each detector are then stored in two dimensional spectra (Figure 4.8a,b) where each axis corresponds to the integrated energy signal for their respective gates. One should note in these figures that both the gamma and the proton bands can be clearly distinguished. Also, the resolution of the 0° detector is somewhat better than the side detector spectrum because of better light collection efficiency and smaller noise in the single photodiode

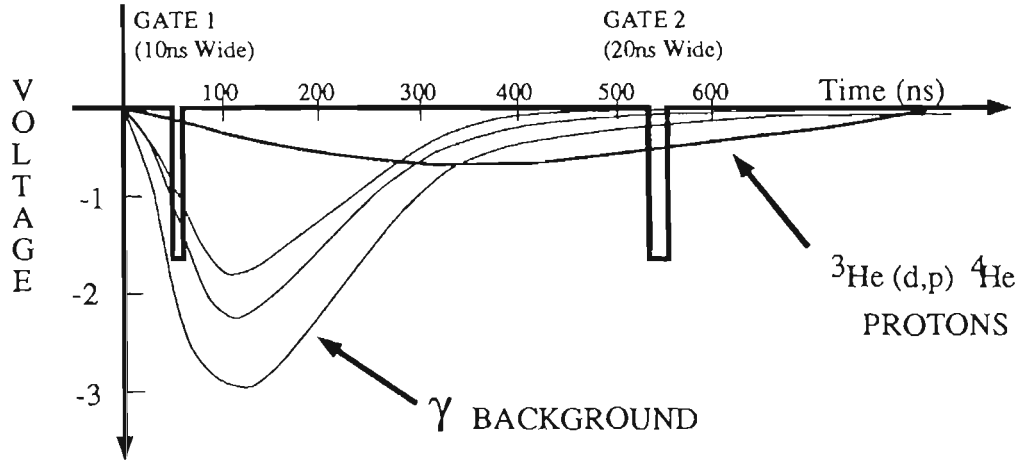

Figure 4.7 - Fast amplifier output for CsI/PD detectors is shown along with the two gates used for generating the PSD.

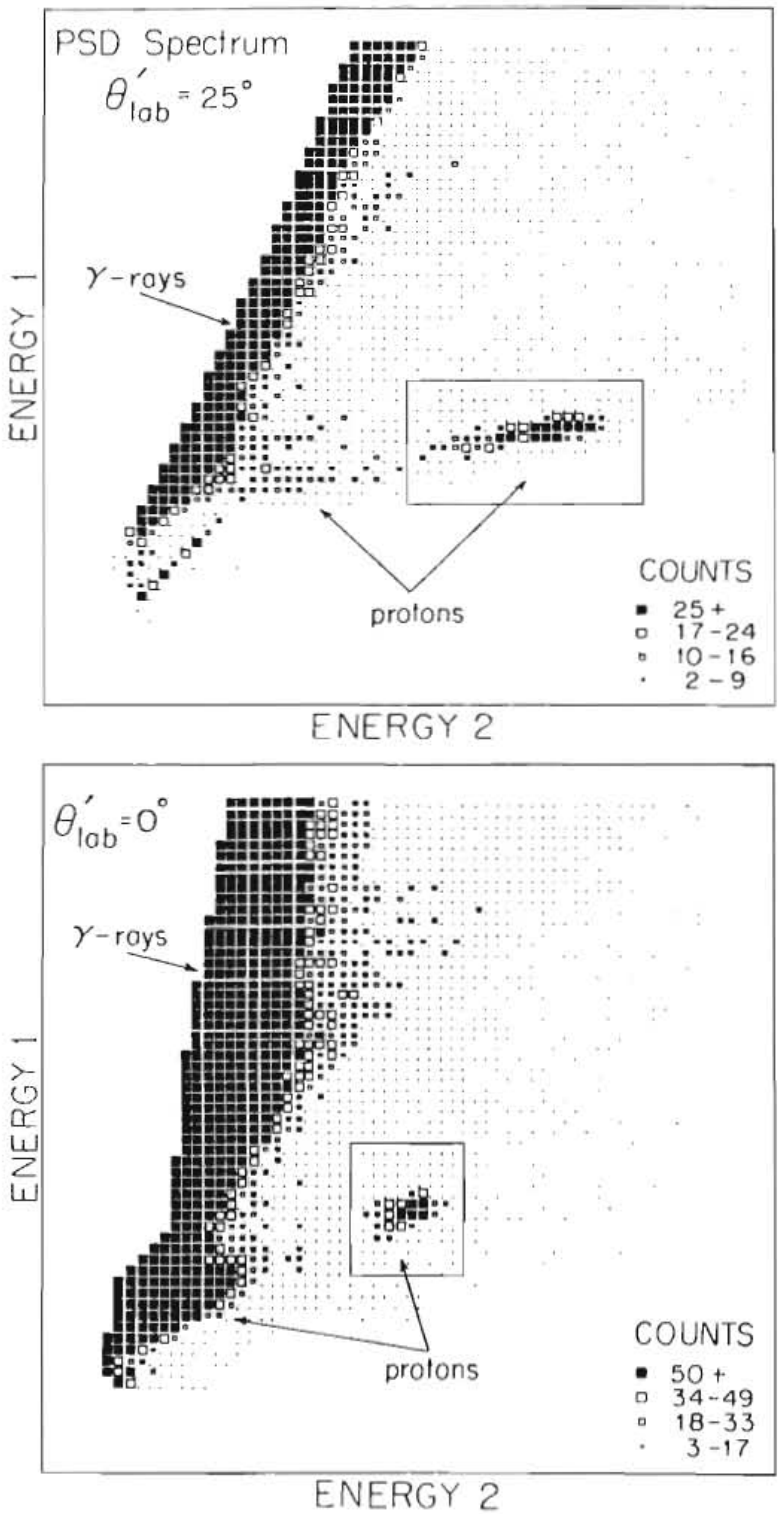

Figure 4.8 - Pulse shape discrimination (PSD) spectra for the side (25°) and 0° CsI/photodiode detectors. $^3He(d,p)^4He$ protons are indicated by the rectangular gate surrounding them.

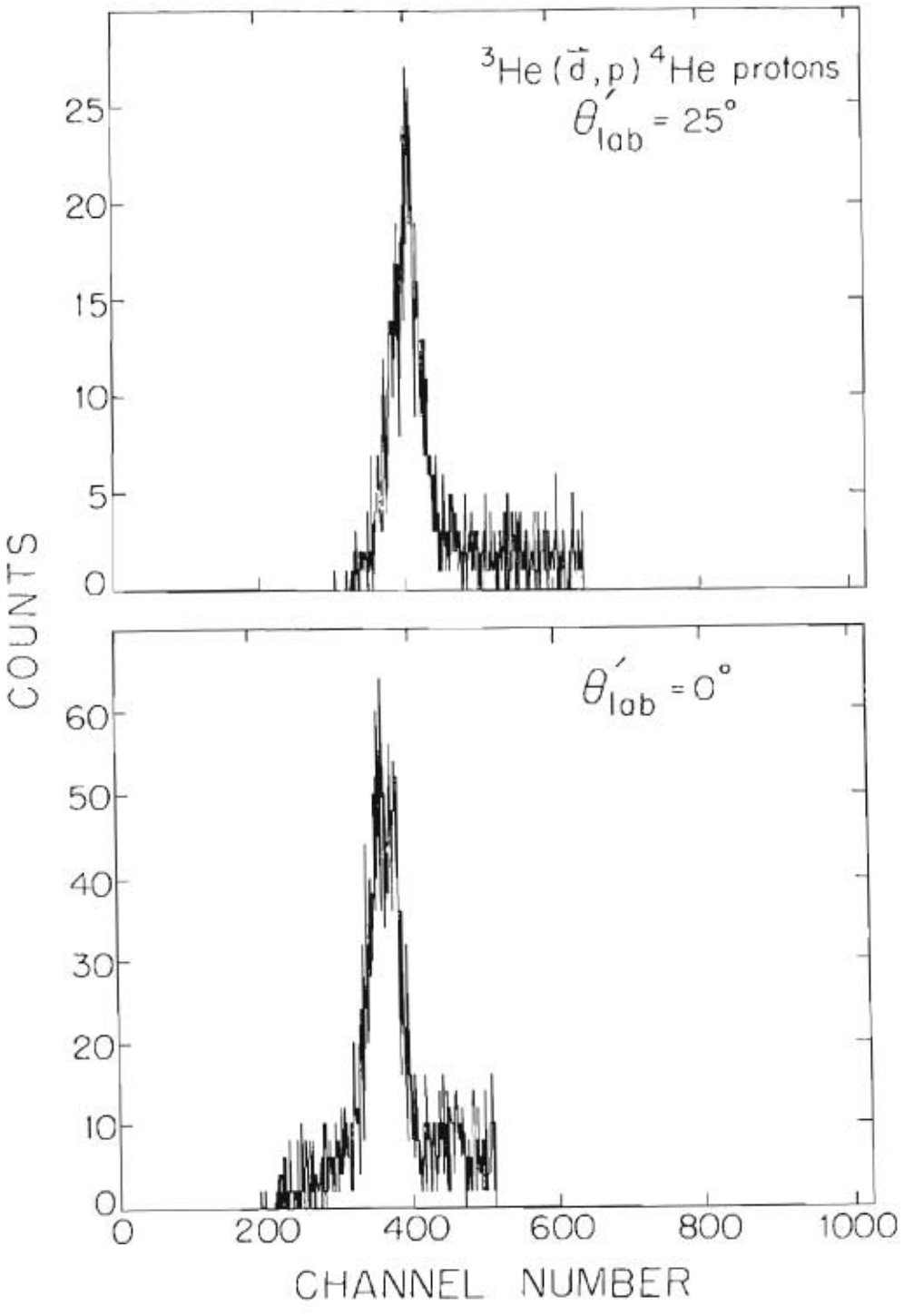

Figure 4.9 - Energy spectra for the side (25°) and 0° CsI/photodiode detectors corresponding to a projection of gated protons onto the ENERGY 1 axis in the PSD spectra. See section 5.3 for details on the two-dimensional gates used for this projection.

(Figure 4.8b). In both detectors one can see a separation of the lower energy protons. In the 0° detector these originate from (d,p) reactions in the Zr target which pass directly through the polarimeter. For the side detector, (d,p) protons arise from deuterons interacting with the entrance window. The energy spectra of the polarimeter detectors are gated in software by the proton bands in respective PSD spectra, and the resulting energy spectra are shown in Figure 4.9a,b for the side and 0° detectors. The spectra shown were accumulated in approximately 24 hours using a 1 mg/cm^2 ^{90}Zr target and 150 nA of polarized beam. The count rate under these conditions was slightly less than 1 count/minute per detector with the polarimeter placed at 30° with respect to the beam direction.

It should be noted here that operation of the polarimeter is currently limited by the resolution and count rate tolerated in the ΔE detector. Its resolution must be sufficient to discriminate against elastically scattered deuterons from any contaminant isotopes in the target as well as from the inelastic deuterons from the isotope of interest. With these conditions the choice of suitable targets for study is somewhat limited.

4.3 Polarimeter calibration and modeling

Polarimeter calibration experiments

In order to use the polarimeter for the determination of the polarization moments of the scattered deuterons, the analyzing powers A_{ij} (Eqns. 3.17-3.19) for the $^3He(d,p)^4He$ reaction must be determined with adequate precision. While the $^3He(d,p)^4He$ reaction has been extensively studied in the energy range of interest [Grü73,Ton80], the geometrical arrangements and deuteron energy spreads applied in

previous experiments and those of the present polarimeter are significantly different. Hence, a series of calibration experiments were performed aimed at the determination of the effective values of A_y, A_{xz}, A_{yy}, and A_{zz} at θ'=25° and 0° for the present polarimeter.

Polarized beam was produced in the Lamb-shift polarized ion source at TUNL and accelerated using the 8 MV FN tandem Van de Graaff. A Wien filter placed immediately following the ion source allowed orientation of the spin axis in any arbitrary direction. The analyzing power data were taken at five incident deuteron energies, corresponding to a deuteron energy range of 5-12 MeV within the gas cell. This measurement involved collecting data for three different orientations of the incident beam spin axis. Following the Madison Convention [Bar70] for the angles β and ϕ as defined in section 3.1, the analyzing power data were taken with incident spin along the y axis ($\beta = 90°$ $\phi = 0°$), the z axis ($\beta = 0°$), and the xz axis ($\beta = 45°,135°$ $\phi = 270°,90°$). The measurements were performed also for two different spin directions (i.e. with spin up (+) and down (-) along the direction of the spin quantization axis). For each axis and incident energy, data were also taken in alternating spin *states* [Hae67] (see also section 5.2). Polarized beam in state 1 had both vector and tensor components $p_Z = p_{ZZ} \approx 0.5$ (from a theoretical maximum of 1.0) and in state 2 was purely tensor polarized with $p_Z = 0$ and $p_{ZZ} \approx -1.0$ (theoretical maximum for p_{ZZ}=-2.0). Figure 4.10 shows the associated analyzing powers that may be measured for each spin orientation. It can be seen that the five independent analyzing powers are overdetermined through such a procedure.

Y AXIS 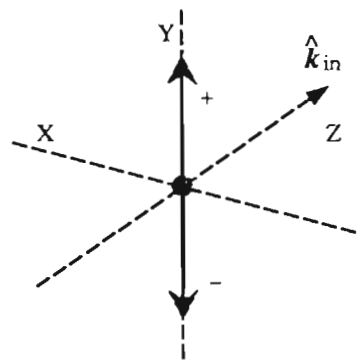	$A_y(25°)$ $A_{yy}(25°)$ $A_{zz}(25°)$ $A_{zz}(0°)$
Z AXIS 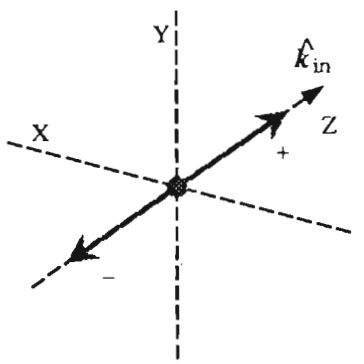	$A_{zz}(25°)$ $A_{zz}(0°)$ All Others Are Zero
XZ AXIS 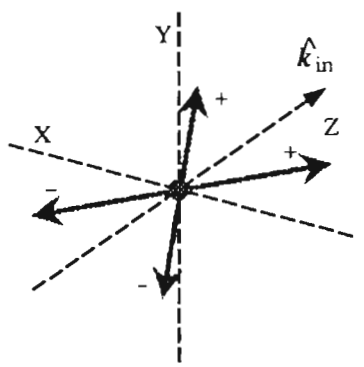	$A_{xz}(25°)$*

Figure 4.10 - Measurable analyzing powers for different incident spin orientations.

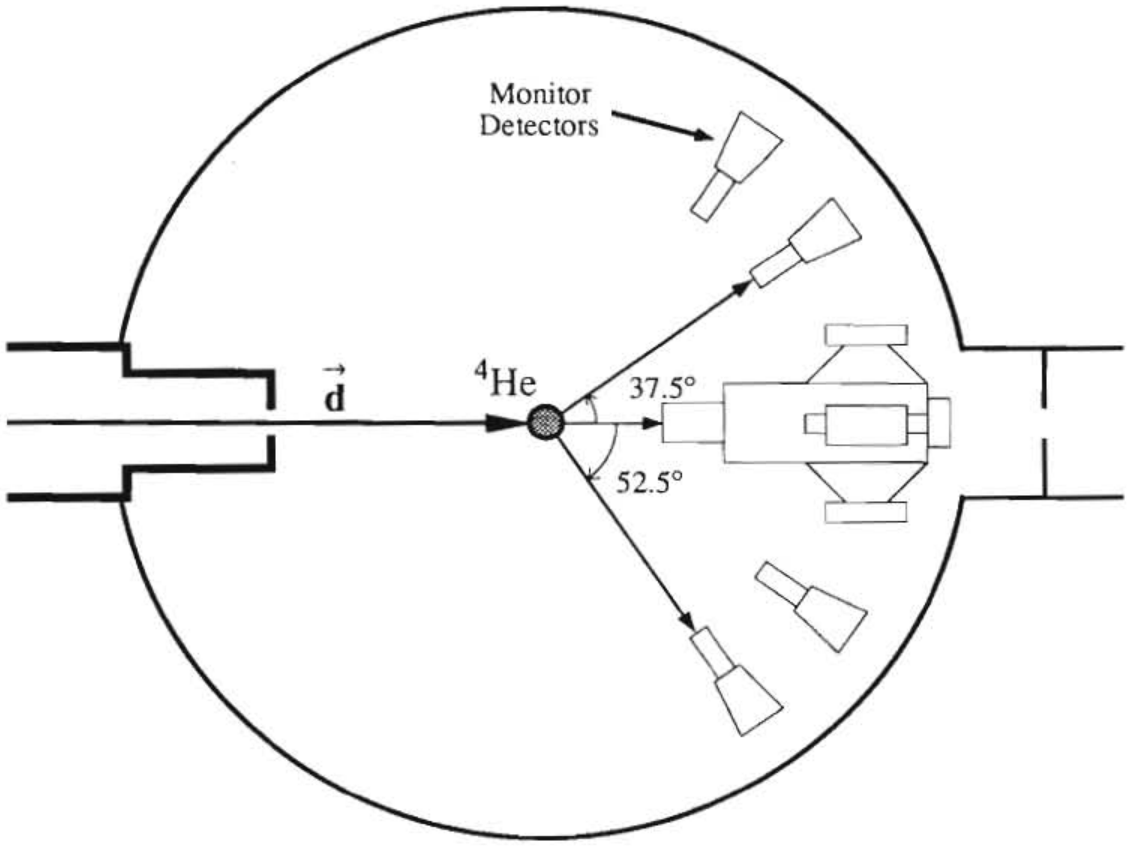

Figure 4.11 - Scattering chamber set-up for polarimeter calibration experiments

To facilitate the calibration measurements, the polarimeter was placed in the direct beam in the scattering chamber (see Figure 4.11). When the polarimeter was oriented in this manner the ΔE detector was removed and replaced with a degrading foil of equivalent thickness. The incident beam current was reduced to the order of 1 nA to limit the count rate in the detectors to manageable levels. The polarimeter gas cell assembly was electrically isolated from the detectors and the chamber to allow integration of the total beam current hitting the polarimeter. To insure an uniform illumination of the polarimeter's entrance collimator we routinely rotated into the beam a thin plastic scintillator with a 0.635 cm diameter hole and monitored the beam focus.

The incident polarization of the beam was continuously monitored via the

$^4He(\vec{d},d)^4He$ reaction at two angles, 37.5° and 52.5° (Figure 4.11). A similar technique was used for calibration of the beam-line deuteron polarization monitor [Ton80]. This is the same monitor used in determining incident beam polarizations during the normal operation of the present polarimeter. Analyzing power data for the $^4He(\vec{d},d)^4He$ reaction compiled in [Ton80] were used in the evaluation of the analyzing powers in the present calibration experiments. Compiled values of A_y, A_{yy}, and A_{zz} for $^4He(\vec{d},d)^4He$ given there were fitted over the entire energy region of interest (calibration information for the deuteron elastic scattering is given in Appendix D). The uncertainty in this fit directly affects the precision of the beam polarization (p_Z and p_{ZZ}) measurements. Beyond statistics, the primary error in p_Z comes from both the uncertainty in and magnitude of A_y. To a lesser extent the uncertainty in A_{yy} and A_{zz} affects the error in p_{ZZ}. The accuracy of the calibration curves for A_y and A_{yy} is about 3%.

Systematic errors such as false asymmetries in the polarimeter introduced by beam fluctuations during spin flips were minimized using the refocusing techniques described earlier. They are more important in the determination of yields in the $^4He(\vec{d},d)^4He$ monitor detectors, and were found to be good to 3% from comparison of yields in the left and right detectors. Overall, considering uncertainties in the $^4He(\vec{d},d)^4He$ analyzing powers and systematic and statistical errors, the incident beam polarizations were determined to better than 6%. It is important that incident polarizations be determined as precisely as possible because they limit the accuracy to which the $^3He(\vec{d},p)^4He$ analyzing powers and the overall polarimeter calibration can be determined.

In Figure 4.12 the results of the present calibration are shown in comparison with the previous calibration of the deuteron monitor of [Ton80]. The values of the analyzing powers determined in the present calibration are slightly shifted toward smaller absolute values. This is not unexpected because of the larger angular

acceptance of the detectors in the present polarimeter as well as the slightly different collimation angle. In addition, the large energy spread for deuterons passing through the high pressure gas cell contributes to the differences seen It is important to note though that the general shapes of the energy dependence of analyzing powers for both calibrations are similar. This allows one to have more confidence in constructing a new calibration curve and extrapolating somewhat beyond the energy range of the present calibration data. The error bars shown in Figure 4.12 reflect the statistical and systematic uncertainties described above. The compiled values are given in Appendix D.

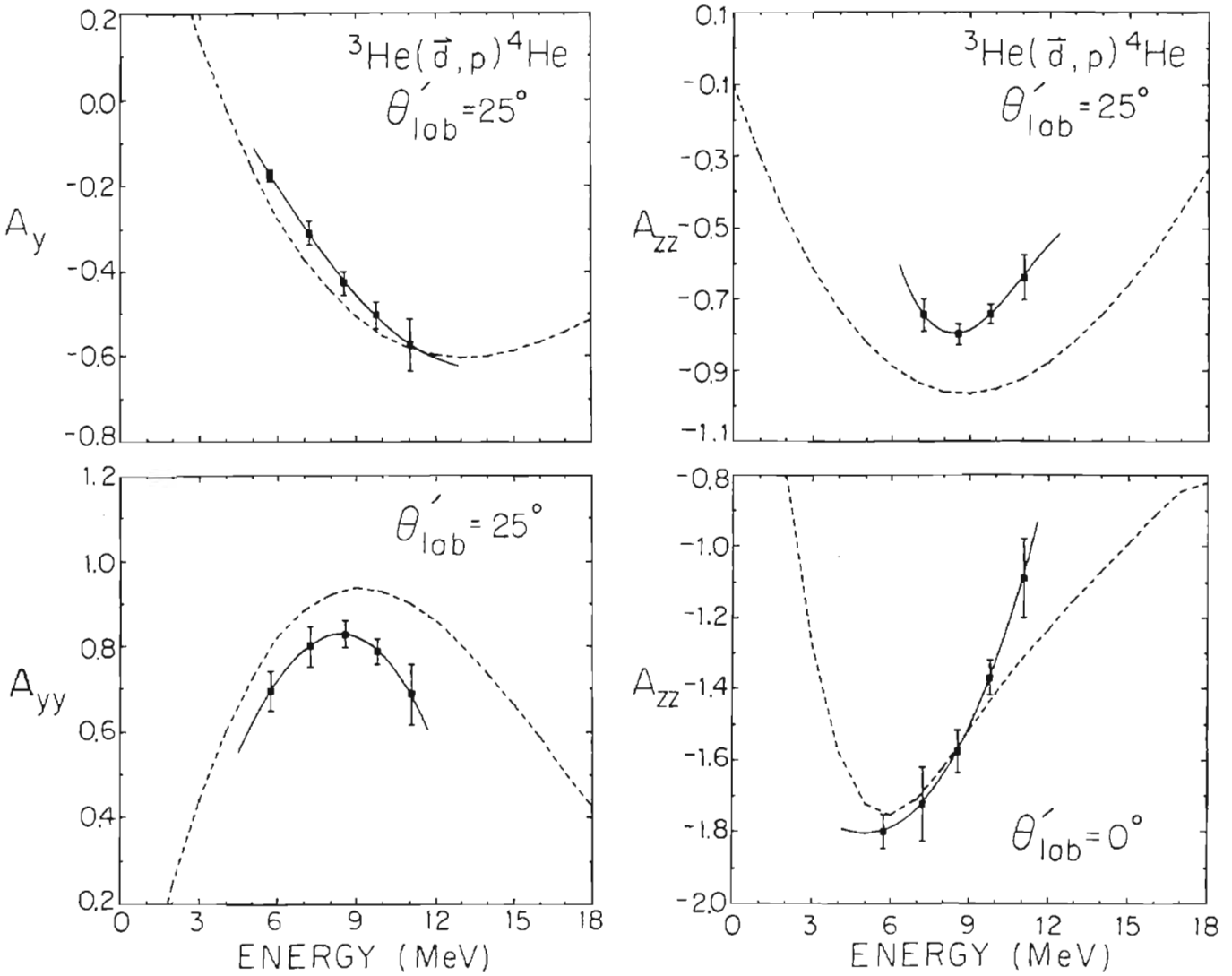

Figure 4.12 - The $^3He(\vec{d},p)^4He$ analyzing power data and calibration for the present polarimeter are shown. The dashed curve corresponds to the calibration of the polarization monitor from [Ton80].

Monte Carlo modeling of the polarimeter

An additional calibration of the present polarimeter was needed in order extract properly normalized polarization information. This involved understanding how the changing cross section and energy across the face of the polarimeter entrance collimator affect the subsequent polarization measurement. In terms of the present measurements of scattered polarization moment $p_{z'z}$, we needed to know how the unpolarized cross section ratio of side to 0° detectors (from Eqn. 3.19) changed for each scattering angle where polarization transfer measurements were made. The only way this information could be obtained was from Monte Carlo modeling of the polarimeter operation. In order to determine how accurate the computer model was, we compared it to direct beam measurements with various types of collimation.

The basic geometry of the polarimeter (described in section 4.1 and shown in Figure 4.1) was coded, including entrance collimator, gas cell dimensions and vane and 0° collimation. The modeling was done in two stages. First, deuteron trajectories were identified through the entrance collimator and gas cell and the scattering energy and position was determined, then based on known cross sections, the subsequent proton trajectories were determined and checked to see if they passed through either the vane or 0° exit collimators. Both proton and deuteron energy loss information were necessary input for the code although the deuteron energy loss data was the most important. This data was obtained through use of the energy loss code BABEL[3] [Bow82] and included calculations of energy loss of deuterons when passing the silicon ΔE detector, the stainless steel entrance foil and the ^{3}He gas cell. In addition to the energy loss, the effects of small-angle multiple scattering were considered for

[3] BABEL uses the relativistically correct Bethe formula for calculation of energy loss by splitting the target up into small elements. A similar technique was used to calculate deuteron energy loss through the gas cell. As long as the total energy loss does not approach the total particle energy the calculations are generally correct.

deuterons from the passing detector and entrance foil and for protons from the tantalum stopping foil at 0°. This had the general but significant effect of altering the particle trajectories to a slightly more diffuse pattern through the polarimeter. Information on multiple Coulomb scattering calculations were obtained from [Leo87]. The final piece of information necessary for the model calculations was relative cross section information for the $^3He(d,p)^4He$ reaction with respect to angle and energy. This data was extracted from cross section measurements made by Grüebler *et al.* [Grü71,73] which included angular distributions of cross sections (θ_{lab} = 25°-150°) in an energy range from E_d = 2.8-11.5 MeV. Also used were relative cross section information taken at TUNL in the same energy range for forward angles between 0° and 30° in the lab. These data were normalized to the data of [Grü73] at 11.5 MeV (see Appendix D).

The basic steps of the calculation consist of first generating a distribution of deuterons on the rear face of the entrance collimator with trajectories determined from an initial target position approximately 12 cm away. Each deuteron trajectory is then traced through the gas cell modified by the multiple scattering. This path is then binned with respect to deuteron energy. The integrated cross section vs energy data are used to determine the energy and subsequently the position of the scattering. The outgoing proton scattering angle is calculated from the differential cross section data. Finally, the proton path is followed and it is determined whether it hits one of the five polarimeter detectors.

Several test experiments were made in an attempt to provide some data with which to compare to the Monte Carlo predictions. One of the problems, however, is that it is difficult to produce an incident unpolarized beam that closely approximates the divergent nature of the scattered beam. Hence, we attempted two different types of experiments. In the first run the polarimeter was placed at 0° with the standard 0.635 cm square collimator. A 6.35μm Havar gas cell at 1 atm of air was used as a

target to disperse the beam similarly to the calibration experiment. Unfortunately, in this experiment there were serious problems with beam fluctuations on target which became evident through significant asymmetries in the polarimeter detectors. Two data points were eventually taken at energies corresponding to 5.7 and 6.8 MeV in the center of the polarimeter gas cell (see Table D.3 in Appendix D). The second run involved replacing the standard collimator with a 6.35 cm long 0.159 cm diameter collimator. This provided a very narrow parallel beam down the center of the polarimeter. Data points at three different energies were taken for this configuration (see Table D.3). Finally, there were several occasions when setting up for polarization transfer experiments that direct unpolarized beam was placed on the polarimeters at 0°. These data represent direct unscattered beam incident on the entrance collimator and are also listed in Table D.3.

Figure 4.13 shows the reference data along with the Monte Carlo calculations representing the three different entrance collimator configurations discussed above. It is interesting to note that while the calculations for the large square collimator are in agreement with the data (calcs B and C) the narrow collimator calculation (A) is approximately 15% too large. It is difficult to isolate where this discrepancy may come from. There are many places where adjustments can be made in the calculations either for the geometry or cross sections or energy loss. In general though the overall agreement with the data is good, and given that the PTO data was taken with the larger collimator no further renormalization of the Monte Carlo calculations were made.

Also shown in Figure 4.13 are the final calculations for the polarimeter cross section ratios at each incident energy and angle that the PTO data were taken. Even though deuterons incident on the ^{90}Zr target were always at 15 MeV, the combination of kinematics and energy loss through the target varied the scattered energy on the polarimeter. The calculations are tabulated in section 5.3, along with a description of

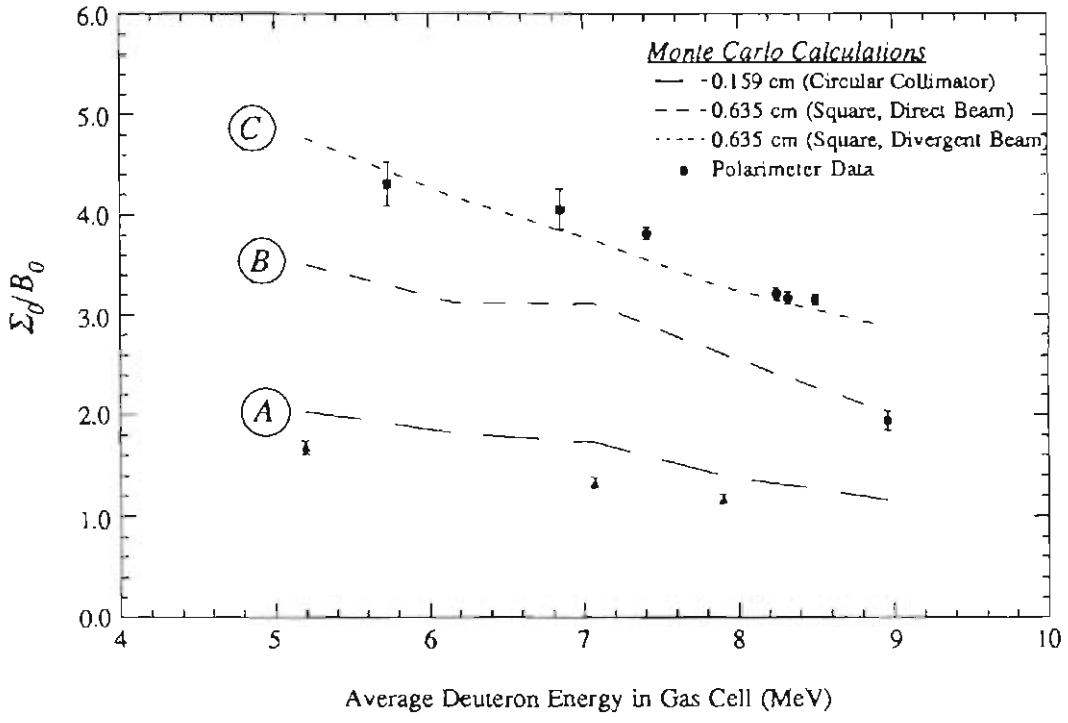

Figure 4.13 - Monte Carlo Calculations for polarimeter cross section ratio Σ_0/B_0 for several different entrance collimator geometries. Data for Calculation A are shown as triangles. The data for calculations B and C are the squares. The "Polarimeter data" points are Monte Carlo calculations for use in analyzing the polarization transfer data (see section 5.3).

the polarization transfer data analysis. Even with the effects of the $^{90}Zr(d,d)^{90}Zr$ cross section distribution across the face of the polarimeter the calculations are in reasonably good agreement with the predictions for uniformly scattered beam. Uncertainties shown for these points represent average deviations determined from multiple Monte Carlo calculations.

Chapter V

Data Acquisition and Analysis

5.1 Experimental considerations

Given the primary experimental goal of polarization transfer measurement for deuteron elastic scattering, it was necessary to determine not only which measurements were necessary, but also which ones we were best capable of measuring. In Chapter IV we discussed the general performance and operation of the polarimeters necessary for the PTO measurements. In this chapter we present details of the actual PTO experiments as well as details of other associated experimental measurements. All the present measurements that are discussed in this chapter were made at TUNL using the 8 MV FN Tandem Van de Graaff accelerator and either the direct extraction negative ion source (DENIS) or the Lamb-shift polarized ion source (PIS) [Cle74][1].

Target choice

Because of the difficulties in PTO measurements (primarily associated with the low count rates) we needed to choose a target for study that could satisfy rather specific criteria. Limitations of the polarimeter's passing detector resolution and the need for adequate separation of elastically-scattered deuterons required that the

[1] The Lamb-shift polarized source no longer exists since being decommissioned in the Winter of 1989 thus giving way to a new atomic beam polarized source. It shall be missed -- DJA

target be a thick self-supporting (rolled foil) with minimal contaminants. Also its lowest states excited from the (d,d′) reaction needed to be at least 1 MeV above the ground state and preferably not very strongly populated. These conditions would insure accurate identification of the elastically scattered deuterons from the target of interest. From a theoretical standpoint it was advisable to choose a "good optical model nucleus" (i.e. relatively heavy with a spin-0 g.s.) that perhaps had been studied fairly extensively in the past.

Table 5.1 - ^{90}Zr Targets	
A	1120 ± 25 μg/cm^2
B	≈ 3 mg/cm^2
C	≈ 10 mg/cm^2

The nucleus ^{90}Zr satisfied all of the above requirements. In addition, we were able to make several targets ranging in thickness from 1 to 10 mg/cm^2. This allowed us to offset the significant decrease in cross section at larger angles by using the thicker targets. Table 5.1 lists the three targets used in the various experiments described here. ^{90}Zr has been investigated previously at deuteron energies ranging from 5.5 MeV to 22 MeV [Har72, Knu73, Bak75, God79, Tak87]. Measured observables include angular distributions of the cross section, vector and tensor analyzing powers. There have been, however, no deuteron PTO measurements published to date on Zr or for that matter any other nucleus heavier than ^{4}He.

We chose a bombarding energy of 15 MeV for the present scattering experiments, the primary reason being that this was about the highest energy the TUNL tandem accelerator could operate without severely taxing its capabilities. Also at this energy a complete set of cross section and analyzing power measurements for $^{90}Zr(\vec{d},d)^{90}Zr$ were previously made at Los Alamos [Har72]. These provided useful comparisons with the present measurements.

Measurement choices

The TUNL Lamb-shift polarized ion source has three modes of operation for

polarized deuterons and are refered to as *states* 1, 2 and 3 [Hae67]. States 1 and 2 are created in the so called *strong field* in the argon canal and correspond to theoretical polarizations of $p_Z = p_{ZZ} = 1$ and $p_Z = 0$; $p_{ZZ} = -2$ respectively. State 3 requires careful adjustment of the magnetic field to create a purely vector polarized beam ($p_{ZZ} = 0$) with theoretical maximum $p_Z = {}^2/_3$. In addition, the spin axis can be flipped along the direction of the spin quantitization axis effectively alternating the sign of p_Z.

In Chapter III we showed that a PTO of interest for investigating the deuteron-nucleus tensor interaction was $K_y^{z'z'}$ (actually $K_1 = K_y^{z'z'} - 1/2A_y$). Its measurement requires use of an incident vector polarized beam, preferably with p_Z as large as possible. However, from Eqn. 3.21 one can see that there is an additional sensitivity to $K_{yy}^{z'z'}$ when the incident beam is tensor polarized. We chose to make the PTO measurements using state 1 polarized beam, thereby determining the combination $3K_y^{z'z'} + K_{yy}^{z'z'}$. While this increased the complexity of the experiments somewhat, we felt more comfortable relying on the $p_Z = p_{ZZ}$ condition of state 1 rather than chancing the arbitrary tensor contaminations possible when using state 3 beam. In addition, state 1 beam offers an effectively higher incident vector polarization which is very important to the experimental sensitivity of the PTO determination. A complete discussion of these measurements is given in section 5.3.

The polarization transfer determinations also require using analyzing power information for the same reaction, in particular (see Eqns. 3.21, 3.22) angular distributions of A_y, A_{yy} and A_{zz}. The Los Alamos data for d+^{90}Zr at this energy were limited to a forward angle of $\theta_{lab} = 40°$. We needed distributions starting from $\theta_{lab} = 25°$, Hence we made independent measurements of these analyzing powers at 15 MeV for the angular range $25° \leq \theta \leq 160°$. A general description of how these data were taken and the results are given in section 5.2.

To complete the polarized single-scattering data set we chose to use the existing cross section and A_{xz} measurements of [Har72]. The A_{xz} measurement is

particularly sensitive to systematic uncertainties and quite difficult to measure accurately. The use (at Los Alamos) of the rotatable *super-cube* provided in principle more accurate results than attainable at TUNL. Confidence in this decision is borne out somewhat in hindsight from the fact that duplicate measurements of the analyzing powers (A_y, A_{yy}, A_{xx}) were consistent within the specified uncertainties although the present measurement has a higher accuracy. A final note: the cross section measurements of [Har72] are only relative differential cross sections and hence had to be renormalized as described in section 5.2.

Finally, to complete the entire d+^{90}Zr scattering data set, differential cross sections for three states in the $^{90}Zr(d,p)^{91}Zr$ reaction were measured at 15 MeV. To our knowledge no other data has been published at this energy. The (d,p) channel is the largest contributing non-elastic channel in terms of cross section, and these data were taken primarily to provide necessary information for a coupled-channels analysis of the elastic scattering (see Chapter VI). Details on these measurements are discussed in section 5.4.

5.2 $^{90}Zr(\vec{d},d)^{90}Zr$ analyzing power measurements

Present Measurements

Angular distributions of the analyzing powers A_y, A_{yy} and A_{xx} were obtained for deuteron elastic scattering from ^{90}Zr in 5° steps from $\theta_{lab} = 25°$ to 160° using a standardized eight-step measurement scheme. This method was first used by Tonsfeldt [Ton80] and later refined and "perfected" by Bowsher [Bow89]. Detailed descriptions of the electronics for data acquisition and the software for data sorting and calculations for this scheme can be found in both references. The procedures used in the present measurements are very similar and are described here only briefly.

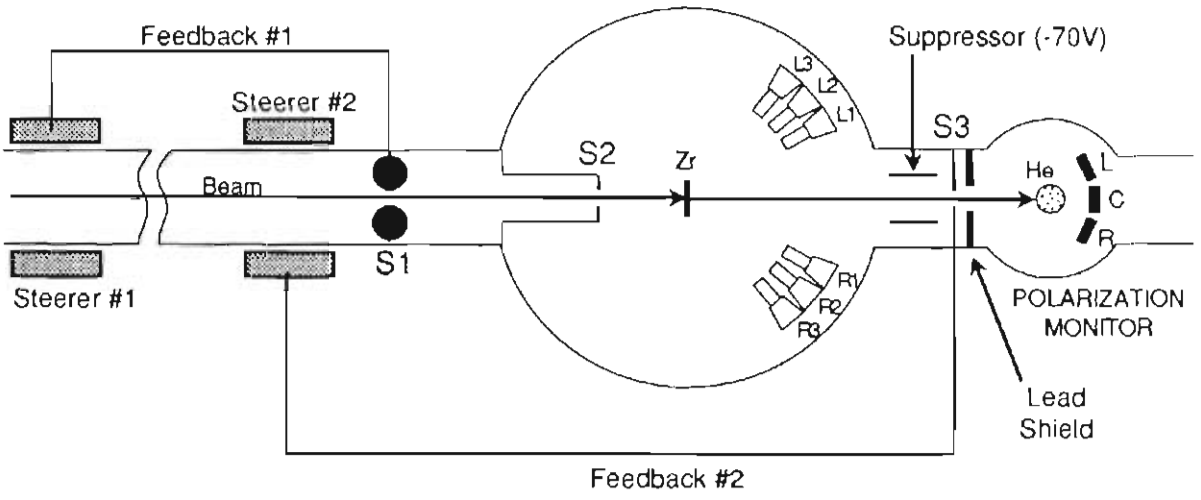

Figure 5.1 - Scattering chamber set-up for $^{90}Zr(d,d)^{90}Zr$ analyzing power measurements.

A schematic for the scattering chamber where the analyzing power measurements were made is shown in Figure 5.1. The entire chamber and polarization monitor assembly is rotatable allowing positioning of detectors at any azimuthal angle. Also the chamber detectors are placed on plates that allow a continuous range of detector angle θ. The beam positioning on target and into the monitor is generally defined by three different sets of slits (S1, S2, S3). There are two feedback steering systems which can be used to minimize beam wavering on target. During the actual experiment, feedback system #2 was not fully implemented (only vertical steering was controlled) because of a design problem with the split Faraday cup slits (S3) that allowed excessive electron crosstalk when well-focused beam was incident on the slits. The total charge on target was digitized using a Brookhaven Corporation integrator (BCI) and was taken as the sum of the total charge striking the S3 slits and that which passed through into the polarization monitor. The monitor charge integration was made separately using an Ortec 439 integrator. Average beam intensities on target during the run ranged from 10 nA to 90 nA depending on the detector positions.

Data were taken in two separate *sequences*. Sequence 1 included chamber

horizontal (i.e. detectors left and right of the target) measurements for the incident spin alternating between the four permutations of spin states 1 or 2 and spin direction up or down[2]. This provided determination of both A_y and A_{yy}. Sequence 2 data were taken with the chamber vertical (detectors up and down) and the with the same alternating sequence of spins. The combination of sequence 1 and 2 data allowed determination of A_{xx} and A_{zz}.

The polarization monitor [Ton80] simultaneously accumulated data that determined the overall incident beam polarization (p_Z and p_{ZZ}) for the run. The monitor used the $^3He(d,p)^4He$ reaction as an analyzer and three detectors: two at the left and right (at 24.5°) and one at 0°. The monitor also was able to rotate with the chamber providing, in effect, for the two sequences, left, right, up, down, and 0° measurements for each spin state. Typical values for the polarizations during the experiment were, for state 1: $0.49 \leq (p_Z, p_{ZZ}) \leq 0.56$, and for state 2: $-1.27 \leq p_{ZZ} \leq -1.10$.

Within the scattering chamber a total of six detectors was placed symmetrically about the incident beam. Detectors on each side were separated by 10° increments. Normal procedure for deuteron scattering experiments calls for the use of E-ΔE particle identification (PID) telescopes (i.e. one thin transmission silicon detector followed by a thick stopping detector) for each detector assembly; However, we simplified the setup somewhat by using PID telescopes only for the R1 and L1 detectors. For the other four detectors the ΔE detectors were replaced by 203 μ Al foils in which incident alpha particles from (d,α) reactions in the target were stopped. Then a single detector with an appropriate thickness stopped the deuterons while passing the protons from (d,p) reactions in the target, which only lost a fraction of their energy. Hence, elastic deuterons showed up as the highest energy peak in the

[2]During these measurements the spin quantitization axis was always in a direction perpendicular to the scattering plane (i.e. vertically). Up and Down refer to direction positive and negative along this axis.

spectrum. A consequence of this method, however, was to essentially lose any other spectroscopic information from other reactions in the target. To check the accuracy of this method, overlap measurements were made for the PID detectors with the other single/foil detector and were found to be generally consistent within calculated uncertainties.

Detector	Type	Thicknesses	Back Slits (wxh)	Acceptance
R1, L1	E-ΔE	2000μ-100μ	0.159cm × 0.953cm	±0.21°
R2, L2	Single/Foils	1000μ/203μ	0.318cm × 0.953cm	±0.42°
R3, L3	Single/Foils	1000μ/203μ	0.318cm × 0.953cm	±0.42°

Table 5.2 - Detector types and collimation for the $^{90}Zr(\vec{d},d)^{90}Zr$ experiment. All the back slits were 21.59 cm from the target

The ^{90}Zr target used for these experiments was first acquired by Varner [Var86] and used in proton scattering experiments (target A of Table 5.1). It is an isotopically enriched (≈97%) rolled foil. Varner determined the thickness to be 1120 ± 25 μg/cm^2. Its thickness was not remeasured at this time because first we believed that the self supporting target would not deteriorate, and secondly, we were primarily interested in analyzing power measurements. Also we found the target to be relatively free of contaminants, such as carbon build-up, even after several long polarization transfer runs.

The present analyzing power data for $^{90}Zr(\vec{d},d)^{90}Zr$ elastic scattering (A_y, A_{yy}, A_{xx}) are shown in Figure 5.2a. They are also tabulated in Table E-1 of Appendix E. These data include corrections for ADC dead time (which was usually less than 1-2%), background subtraction under the peaks, and differing BCI counts between the four polarization states. The error bars associated with the points include both statistical uncertainties and a systematic uncertainty estimated at an absolute ±0.011 for all analyzing power measurements. This estimate comes from observing

variations in the L/R ratio (i.e. where $L = (L1\uparrow \cdot L1\downarrow \cdot L2\uparrow \cdot L2\downarrow)^{1/4}$), which should be unity for equal solid angles and detector efficiencies between left-right pairs of detectors. In general, the statistical uncertainties were 1.5% or less.

Additional data

To supplement our analyzing power data we chose to use existing cross section and A_{xz} measurements done at Los Alamos [Har72]. These data are shown in Figure 5.2b. For the A_{xz} measurements they assigned an absolute uncertainty[3] of ±0.02 (statistical errors were quoted as less than 1%). The cross section measurements however were only relative. The Los Alamos group normalized their cross section data set to some unspecified optical model prediction. We felt it necessary to check this normalization by several methods to estimate its accuracy. First, we made cross section measurement checks at two angles (60°, 70°) using an unpolarized deuteron beam and the same target (target A) as used in the analyzing power experiments. At both angles the measurements agreed with the Los Alamos data to within 5%. In addition our own optical model calculations were made using the code OPTICS and the function minimization routine MINUIT (see Chapter VI for a description). Using the input data set including the cross sections of [Har72] and the present vector analyzing power (A_y), it was found necessary to renormalize these cross sections by a factor 1.022 to improve agreement with the calculations particularly at the forward angles[4]. As a result the cross section data shown are renormalized by a factor 1.022, and the error bars represent the 5% normalization uncertainty quoted by the experimenters.

---

[3] This assignment seems a bit arbitrary and optimistic in the Author's opinion considering the difficulty in minimizing systematic errors in A_{xz} measurements.

[4] An additional note, Goddard [God79] also used the entire LANL data set for ^{90}Zr. He also found it necessary to renormalize the cross sections by 1.03 to improve his optical model fits.

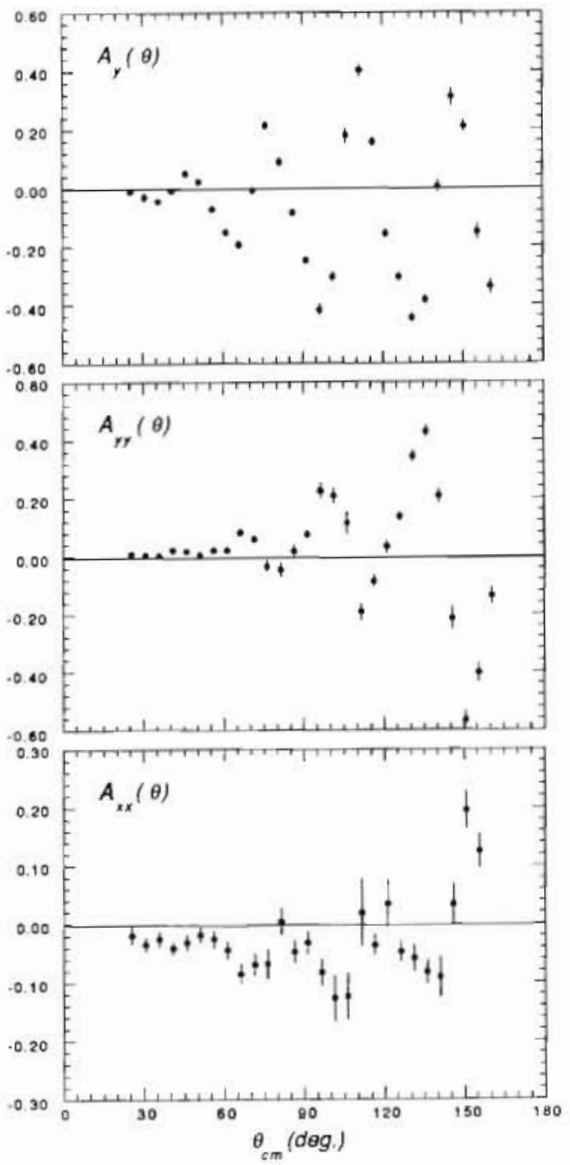

FIGURE 5.2a

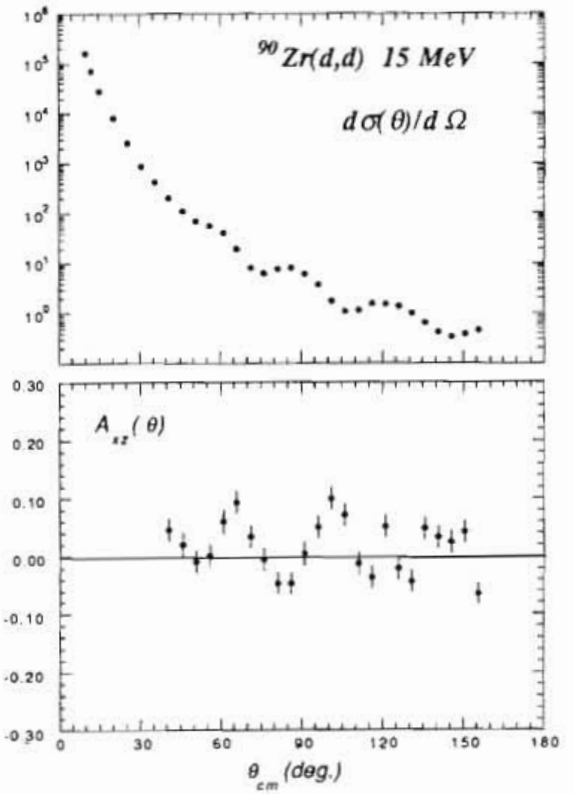

FIGURE 5.2b

Figure 5.2 - Polarized elastic single scattering data for deuterons on ^{90}Zr at 15 MeV. The data in Figure 5.2a were taken in the present experiments while the data in Figure 5.2b were aquired from [Har72].

5.3 $^{90}Zr(\vec{d},\vec{d})^{90}Zr$ polarization transfer measurements

Experimental Considerations

Data for the measurement of polarization transfer coefficients $K_y^{z'z'}$ and $K_{yy}^{z'z'}$ were obtained for deuteron elastic scattering at $E_d = 15$ MeV at forward angles $\theta_{Lab} = 25°, 30°, 35°, 50°$. The polarimeters used for the double scattering experiment and the general methods for PTO measurements are described in Chapter IV. In this section we discuss some of the specifics for the experiment, as well as some techniques used in the analysis of the PTO data.

The scattering chamber used for the present experiment is the same as the one shown in Figure 5.1, with the only modifications being the replacement of the left and right detector sets with left and right polarimeters. As we discussed in Chapter IV, the primary background concern for the polarimeters were γ-rays. Within the scattering chamber there are several "hot spots" where the γ-rays may be generated. These were the chamber slits S2 and S3 as well as the target rod in the chamber center. In order to reduce this background during the experiment, we removed the S2 slits and supporting snout. In addition, lead shielding (≈ 3.8 cm thick) was placed around the front and side faces of both polarimeters. This shielding significantly lowered the background coming from the target. At the back of the chamber a 2.5 cm thick circular lead plug with an ≈3 cm diameter hole to let the beam pass was placed directly in front of the suppressor ring. This helped to shield the polarimeter detectors from the beam dumping on the S3 slits (split Faraday cup). Even running with these modifications, we still found that the detectors in close proximity to the S3 slits (the right detector for the left polarimeter and the left detector for the right polarimeter) had a somewhat higher background. Also, after running with the same target for 24-36 hours (depending on the amount of beam), the activity in the target was high enough to cause significant deterioration of the pulse shape discrimination (PSD) spectra in

all the detectors.

The data were taken with a deuteron beam produced from the Lamb-shift polarized ion source in state 1 ($|p_Z| = |p_{ZZ}|$). The incident beam was oriented along the y axis perpendicular to the scattering plane. Throughout a run the spin direction of the beam was flipped "up" and "down" along this axis. This was done primarily to determine the polarization of the incident beam using the polarization monitor downstream of the target. Only the left and right detectors of the monitor were used and the polarization was calculated using the relation from [Ton80],

$$p_{ZZ}^{(1)} = \frac{2R_{12}}{3A_y - R_{12}A_{yy}} , \qquad R_{12} = \frac{L-R}{L+R} , \tag{5.1}$$

where $L = \sqrt{L\uparrow R\downarrow}$ and $R = \sqrt{R\uparrow L\downarrow}$. Because of the long runs needed to obtain good statistics for the PTO data the incident beam polarization determinations had generally very good statistics ($\approx$0.1%); however we have assigned a systematic uncertainty of 1.5% to these measurements based on fluctuations of the beam incident on the monitor as estimated through L/R ratio variations.

The primary scattered-beam polarization moment of interest in the present experiment was $p_{z'z'}$. This could be measured independently for each polarimeter via Eqn. 3.19. The polarimeters were normally placed at the same scattering angle on opposite sides of the incident beam in order to improve statistics. This was done at both 30° and 50°; however, problems with two detectors on the right polarimeter at 50° caused its data to be lost. Data at 25° and 35° were taken by the left and right polarimeters respectively. Once $p_{z'z'}$ was determined by the polarimeters, it could be related to the incident beam polarization by combining Eqns. 3.21 and 3.22 giving,

$$p_{z'z'} = \frac{P^{z'z'} + \frac{3}{2}p_z K_y^{z'z'} + \frac{1}{2}p_{zz}K_{yy}^{z'z'}}{1 + \frac{3}{2}p_z A_y + \frac{1}{2}p_{zz}A_{yy}} \qquad (5.2)$$

In principle, the polarization transfer coefficients $K_y^{z'z'}$ and $K_y^{z'z'}$ may be determined independently through the spin flipping procedure (this becomes a BCI and dead time sensitive measurement); however, the state 1 measurements of the PTO combination $3K_y^{z'z'} + K_{yy}^{z'z'}$ provided the more precisely determined quantity. Hence, these data which were used in subsequent calculations (see Chapter VI).

Analysis of raw polarimeter data

Throughout the PTO experiments data for both polarimeters were taken in event mode and stored on magnetic tape for later sorting. This proved to be very important in the subsequent data analysis, for both general background reduction as well as for background subtraction under the PSD peaks. These PSD spectra provided both the particle discrimination and energy information for the $^3He(d,p)^4He$ reaction in the polarimeters. Hence, it was important not to lose important information due to inadequate gate setting procedures during the run.

Because of the low count rate in the polarimeters under normal running conditions (≈1 count/min), setup procedures for the experiment included rotating each polarimeter into the incident beam, reducing the beam to low currents (≈1 nA) and then setting up the PSD timing and gates. This was done periodically throughout the run to check for possible drifts in the spectra. However, as long as the event mode gate was set large enough no data would be lost.

Offline re-sorted PSD data for all the detectors of one polarimeter (left at 50°) are shown in Figure 5.3. One can see that the general aspects of each spectrum are

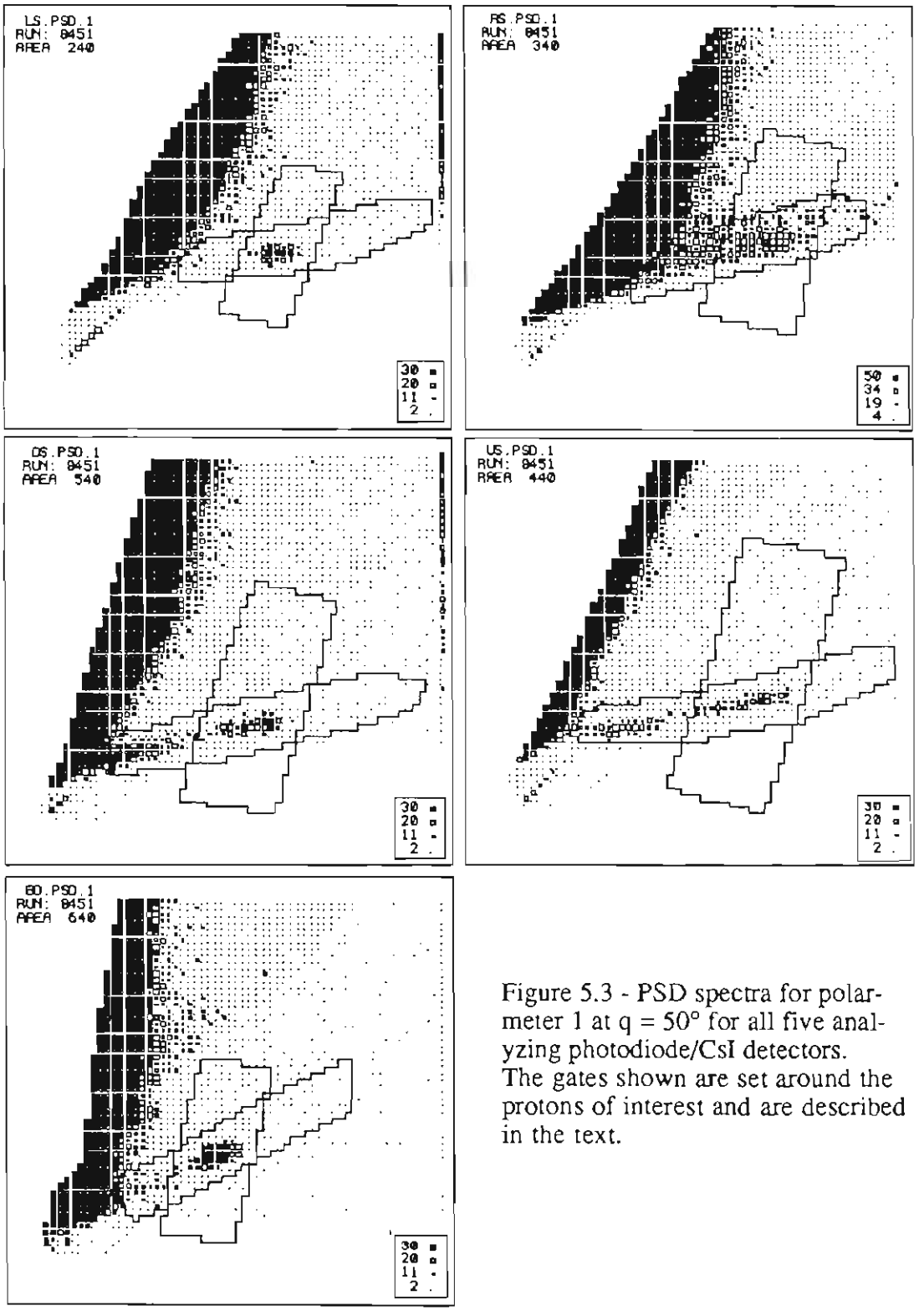

Figure 5.3 - PSD spectra for polarmeter 1 at q = 50° for all five analyzing photodiode/CsI detectors. The gates shown are set around the protons of interest and are described in the text.

the same, the large slope of the gamma band (fast pulses) and the low slope of the proton band (slow pulses). Variations depend on the detector resolution and the timing setup of the PSD electronics (see Chapter IV). Energy information from these spectra can be extracted by projecting gated areas onto one of the energy axes. However, whichever axis is used to extract proton peaksums, first requires proper setting of the gate around the protons of interest. Figure 5.4a shows the two types of gates used in the analysis. Gate 2 is a long gate set tightly around the entire proton band. This gate can be projected onto the Energy 2 axis and the resolution increased to give the resultant proton spectrum in Figure 5.4b. On the other hand Gate 1 is the type we determined to be the best for projecting onto the Energy 1 axis. It is defined by setting the vertical sides of the gate approximately parallel with the γ-ray band and making the gate wide enough to encompass the peak and long enough to provide substantial background levels on either side of the peak. The Gate 1 projected energy spectrum is shown in Figure 5.4c.

In principle, sums for the $^3He(d,p)^4He$ proton peaks in both projected spectra may be extracted after a fitted exponential (for the Energy 2 spectra) or linear background (for the Energy 1 spectra) is subtracted. We found, however, that the Gate 1 projected spectra are more useful for a consistent and more accurate determination of the sums. This is primarily due to the better resolution provided by gating the proton pulses early in the ADC (see Chapter IV). The Energy 2 pulses produce poor energy resolution spectra, particularly for some of the side detectors. As a result the proton peaks in many of Energy 2 spectra are too spread out to get an accurate background subtraction. For the better resolution 0° detectors, sums could be extracted for both energy spectra and were generally found to have consistent peak sums within statistics.

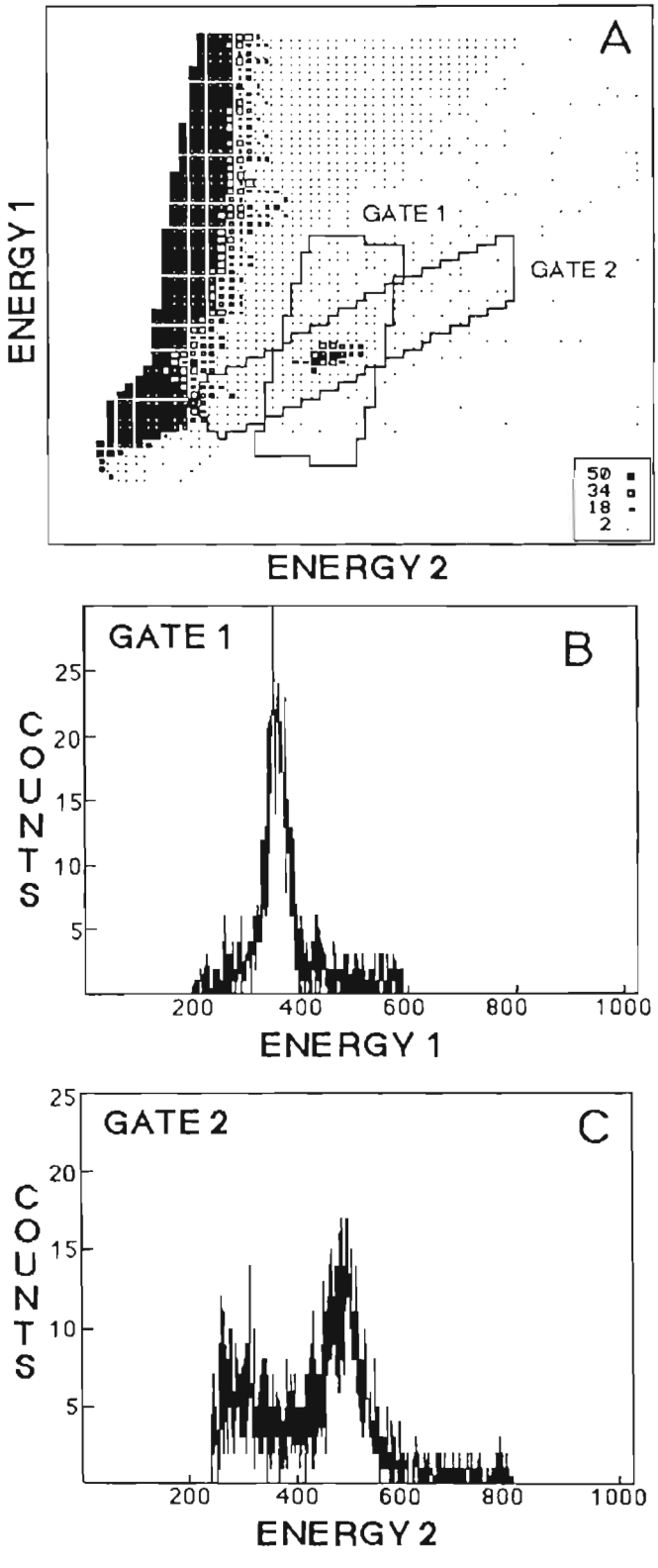

Figure 5.4 - Polarimeter 0° PSD spectrum (A) and the associated energy spectra (B,C) for the two types of gates used in the present analysis. Gate 1 was used for projection on the Energy 1 axis and Gate 2 for the Energy 2 axis.

Results of the PTO analysis

Table 5.3 below shows some of the information used to extract the polarization transfer data, including the targets used (see Table 5.1) and the scattered deuteron energy accounting for kinematics and energy loss through the target. This information was important for use in determining the unpolarized side to zero degree detector ratios (Σ_0/B_0) via Monte Carlo modeling (see section 4.3). These ratios along with the incident beam polarization information are also shown.

Angle(Lab)	POL	Target	Deuteron Energy	Σ_0/B_0	p_Z
25°	L	A	14.97 MeV	3.149 ± 0.030	0.583 ± 0.016
30°	L,R	B	14.81 MeV	3.209 ± 0.030	0.511 ± 0.016
35°	R	B	14.77 MeV	3.166 + 0.030	0.582 ± 0.018
50°	L	C	14.42 MeV	3.817 ± 0.035	0.548 ± 0.016

Table 5.3 - Information used for analysis of polarization transfer calculations. L and R in POL refer to which polarimeters took data at that angle (left or right). Targets are listed in Table 5.1. Uncertainties for Σ_0/B_0 represent estimated errors from multiple Monte Carlo calculations. Uncertainties in the incident beam polarization p_Z include both statistical and estimated systematic errors.

As stated earlier, the most direct PTO measurements are those of the combination $3K_y^{z'z'} + K_{yy}^{z'z'}$. Theoretically, the observable most sensitive to the tensor interaction is K_A (defined in section 3.4) for which the analyzing power combination $(3A_y\text{-}A_{yy})/2$ is added. Data for K_A are shown in Figure 5.5, and, for curiosity, the extracted measurements of $K_y^{z'z'}$ are also shown in Figure 5.5. The primary uncertainties in these data come from statistical errors as well as estimated uncertainties in the determination of the unpolarized cross section ratios. While the relative error for K_A is smaller than for $K_y^{z'z'}$, both data sets suggest a positive trend with increasing angle no matter what renormalization is used.

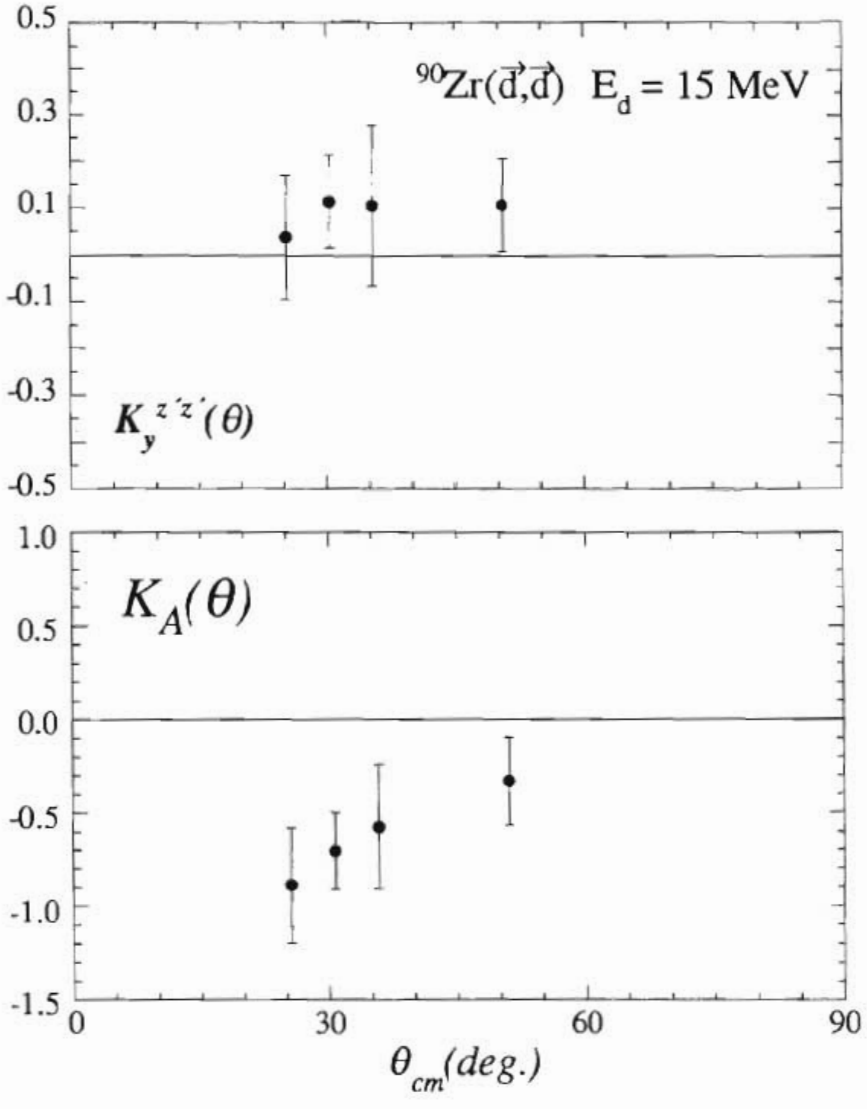

Figure 5.5 - Measured polarization transfer observables $K_y^{z'z'}$ and K_A for deuteron elastic scattering from ^{90}Zr at 15 MeV. The error bars are discussed in the text.

5.4 $^{90}Zr(d,p)^{91}Zr$ cross section measurements

Absolute differential cross sections were obtained for the $^{90}Zr(d,p)^{91}Zr$ reaction at 15 MeV for states $(E; j^{\pi})$ in ^{91}Zr of (0.0 MeV; $\frac{5+}{2}$), (1.2 MeV; $\frac{1+}{2}$) and (2.0 MeV; $\frac{3+}{2}$). These data were taken using the DENIS source at TUNL and the same scattering chamber shown in Figure 5.1. The only differences in the (d,p) experimental setup were that the polarization monitor was replaced by a Faraday cup and only two left-right detector pairs were used instead of three. Angular distributions were taken in 5° steps ranging between laboratory angles of 25° and 125°. The detectors used in this experiment were all E-ΔE telescopes, in order to discriminate the protons from other charged particles and to insure good energy resolution spectra. Table 5.4 lists the detector specifics and geometry for the experiment. A typical detector spectrum is shown in Figure 5.6. Most of the low-lying states for ^{91}Zr up to 3.5 MeV in excitation are identified by numbers. The states whose cross sections were extracted are circled and labeled.

Detector	Type	Thickness	Back Slits (w×h)	Acceptance	Solid Angle
R1, L1	E-ΔE	2000μ-1000μ	0.238cm × 0.953cm	±0.57°	8.946×10^{-4}sr
R2, L2	E-ΔE	2000μ-1000μ	0.238cm × 0.953cm	±0.57°	8.946×10^{-4}sr

Table 5.4 - Detector types and geometry for the $^{90}Zr(d,p)^{91}Zr$ experiment. All the back slits were 15.88 cm from the target. Solid angles refer to individual detectors.

Target A (of Table 5.1) was used for the cross section measurements. From the spectrum in Figure 5.6 one can see that the protons are relatively free from any contaminants and the background under the peaks is quite small. The peak corresponding to $E^* = 2.0$ MeV was generally well separated from neighboring states however there were some angles where peak fitting was necessary for some

detectors (back angles θ = 110°-125°). Even at those angles the corrections were generally less than 20%. Other corrections applied to all of the data included adjustments for ADC dead time. This was generally in the range of 2-3% but was sometimes as high as 8-10% at the most forward angles. There was also a small correction (0.6%) to the solid angles for each detector because of the rounded corners for the slits used directly in front of the detectors. Finally, elastic scattering data were also taken at two angles (θ = 60°, 70°) and elastic cross sections determined. These cross sections were found to be about 5% less than the previously used elastic cross sections shown in Figure 5.2b. Therefore in order for the (d,p) cross sections to be consistent with the elastic cross sections we renormalized the (d,p) data by a factor 1.055.

The cross section data for $^{90}Zr(d,p)^{91}Zr$ at E_d = 15 MeV are shown in Figure 5.8 for the three states discussed above. Values are tabulated in Table E.3 in Appendix E. The error bars are smaller than or equal to the size of the points. They include statistical uncertainties as well as estimated uncertainties for background subtractions, target thickness (≈2%) and solid angles (≈ 1.2%). They also include an 2.5% systematic uncertainty estimated from repeated measurements made during the run. From the observations discussed above we assign an overall 5-6% normalization uncertainty for these data.

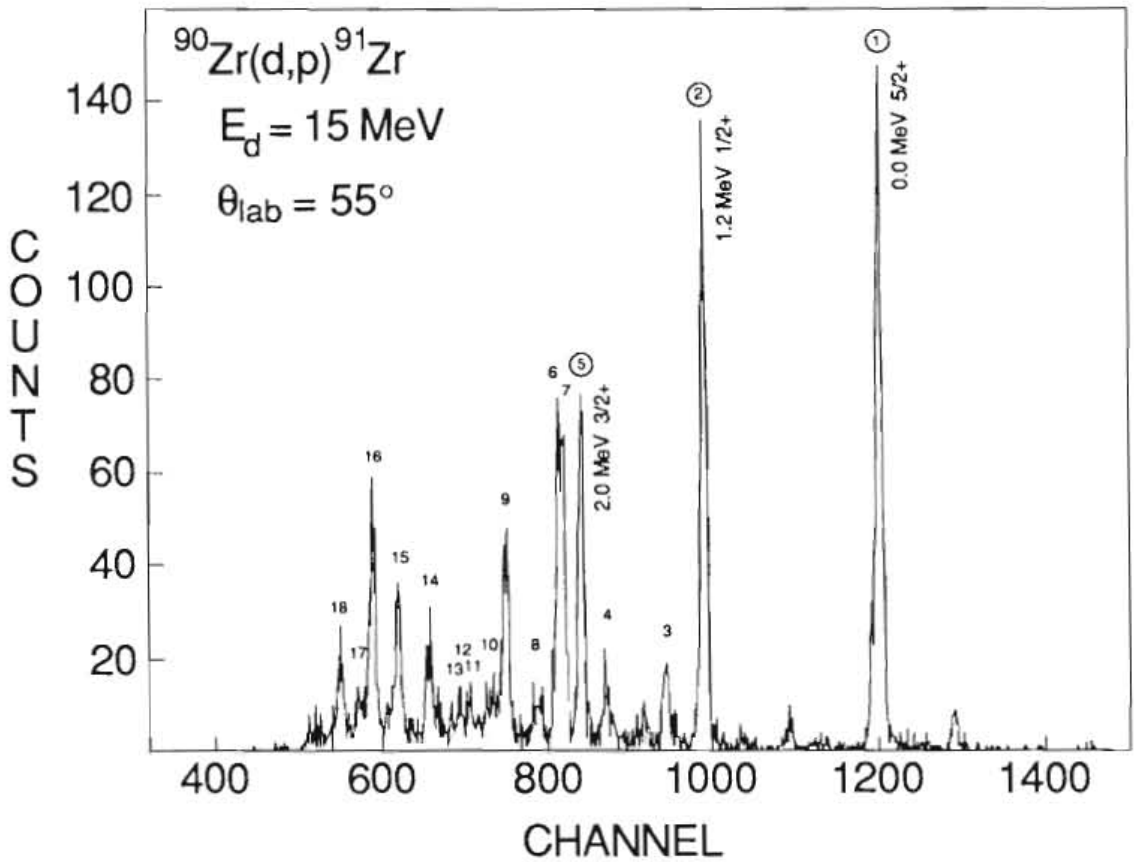

Figure 5.6 - Proton spectra for the $^{90}Zr(d,p)^{91}Zr$ reaction. Numbered peaks correspond to levels in ^{91}Zr. Cross section data were extracted for the labeled peaks.

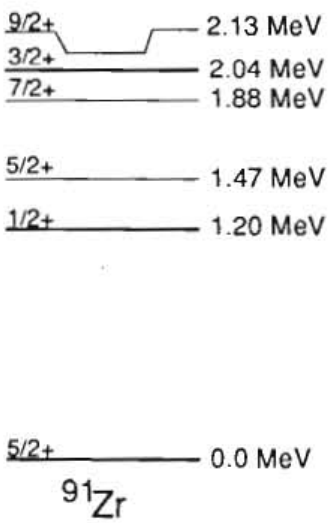

Figure 5.7 - The six lowest energy levels in ^{91}Zr corresponding to labels 1-6 in Figure 5.6.

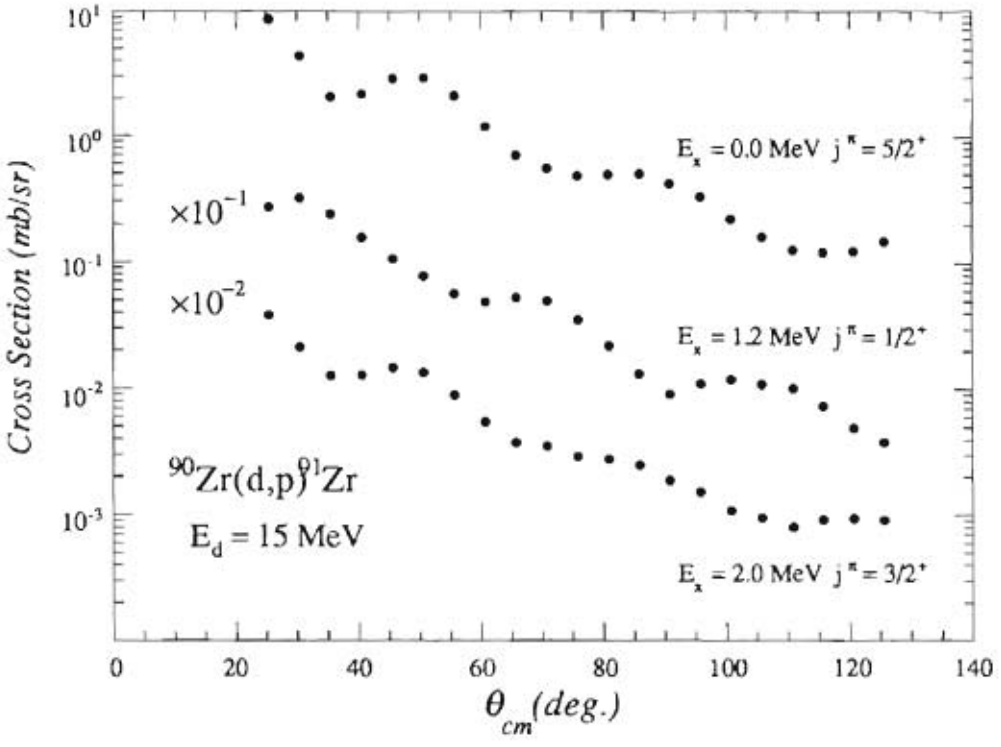

Figure 5.8 - $^{90}Zr(d,p)^{91}Zr$ cross section data at E_d = 15 MeV for the three states in ^{91}Zr corresponding to $(E; j^{\pi})$ of (0.0 MeV; $\frac{5^+}{2}$), (1.2 MeV; $\frac{1^+}{2}$) and (2.0 MeV; $\frac{3^+}{2}$). Errors are smaller than the size of the points.

Chapter VI

Calculation of $^{90}Zr(\vec{d},\vec{d})^{90}Zr$ Observables through Optical Model Analysis and an Investigation of Tensor Spin Dependence in the Coupling of $^{90}Zr(d,p)^{91}Zr$ Channels

6.1 Introduction

In this chapter more detailed investigation is made of the role of the deuteron-nucleus tensor interaction in the elastic scattering of deuterons from ^{90}Zr. This will be done in two ways. First, in section 6.2, a traditional phenomenological approach is taken by an optical model analysis of the scattering. From the folding model considerations and the historical perspective on the role of tensor potentials discussed in Chapter II we consider only the T_r-type tensor potential and not T_p or T_L. A consistent phenomenological form is then established for the T_r potential that gives reasonable predictions for both tensor analyzing powers and the polarization transfer data. In section 6.3 the analysis is extended to a more quantitative level by including explicitly some of the more significant inelastic channels and determining the spin dependent potential generated for the elastic channel due to this coupling. For deuterons scattering from ^{90}Zr at 15 MeV, we are primarily interested in the $^{90}Zr(d,p)^{91}Zr$ channel as it constitutes the dominant inelastic process at this energy. Also, because ^{90}Zr has a closed neutron shell, these neutron transfer channels are somewhat enhanced, which makes it particularly interesting nucleus with which to study these effects.

Computer codes

Three different computer codes were used for the calculations described in this chapter. These were the optical model codes OPTICS [Var86] and DDTP [God79] and the finite-range coupled-channels code FRESCO [Tho88].

Both OPTICS and DDTP calculate the elastic scattering of a spin-one projectile from a target whose spin is ignored, given a complex nuclear optical model potential as described in Appendix A. The primary difference between these two codes is that OPTICS does not allow inclusion of the tensor interaction. It does however provide searching functions on all other optical model parameters through use of the function minimization routine MINUIT [Var86]. In this manner, central and spin-orbit potentials could be optimized for the given data set. DDTP, on the other hand, is a code specifically written for deuteron elastic scattering from nuclei for which all three tensor potential types (T_r, T_p, T_L) may be included. In addition, for the T_r potential, it contains specific radial form factors derived from folding model (FM) calculations [Kea73] which are meant to approximate the FM predictions for T_r. These potential forms (see Appendix A) were used exclusively in the present analysis in determining the complex T_r potential necessary to fit the TAP and PTO data.

FRESCO is a general-use code which uses iterative techniques to perform coupled-channels calculations in finite-range DWBA. It allows coupling between multiple mass partitions and for any number of excitations of both target and projectile states within these partitions. In addition, when coupling between different mass partitions (such as (d,d) and (d,p) channels) is present, FRESCO can calculate the non-orthogonal components of the interaction kernel. As will be discussed later (section 6.3) these terms should not be ignored. Finally, FRESCO also allows input of radial form factors which may in turn be associated with a T_r-type spin operator for

the deuteron optical potential. To our knowledge this is the first attempt to use FRESCO in an analysis of the tensor interaction via the optical potentials or through finite-range coupling.

One of the first concerns that arises when we attempt to use multiple codes in the data analysis is the consistency of the calculations between the different codes. While all three codes used various methods for setting up integration parameters and numerical tolerances, we attempted to provide each code with an identical deuteron elastic scattering input data set with no T_r potential included. The corresponding transition matrix amplitudes when converted to compatible forms were very similar. The observables calculated (cross section and A_y) were virtually identical, differing by only 1% or less. Figure 6.1 shows results of the cross section and vector analyzing power A_y calculations for all three codes. Similar tests were made comparing both DDTP and FRESCO calculations when including a T_r-type potential. Again the codes provided essentially identical results for all the spin-dependent observables, including tensor analyzing powers and PTO.

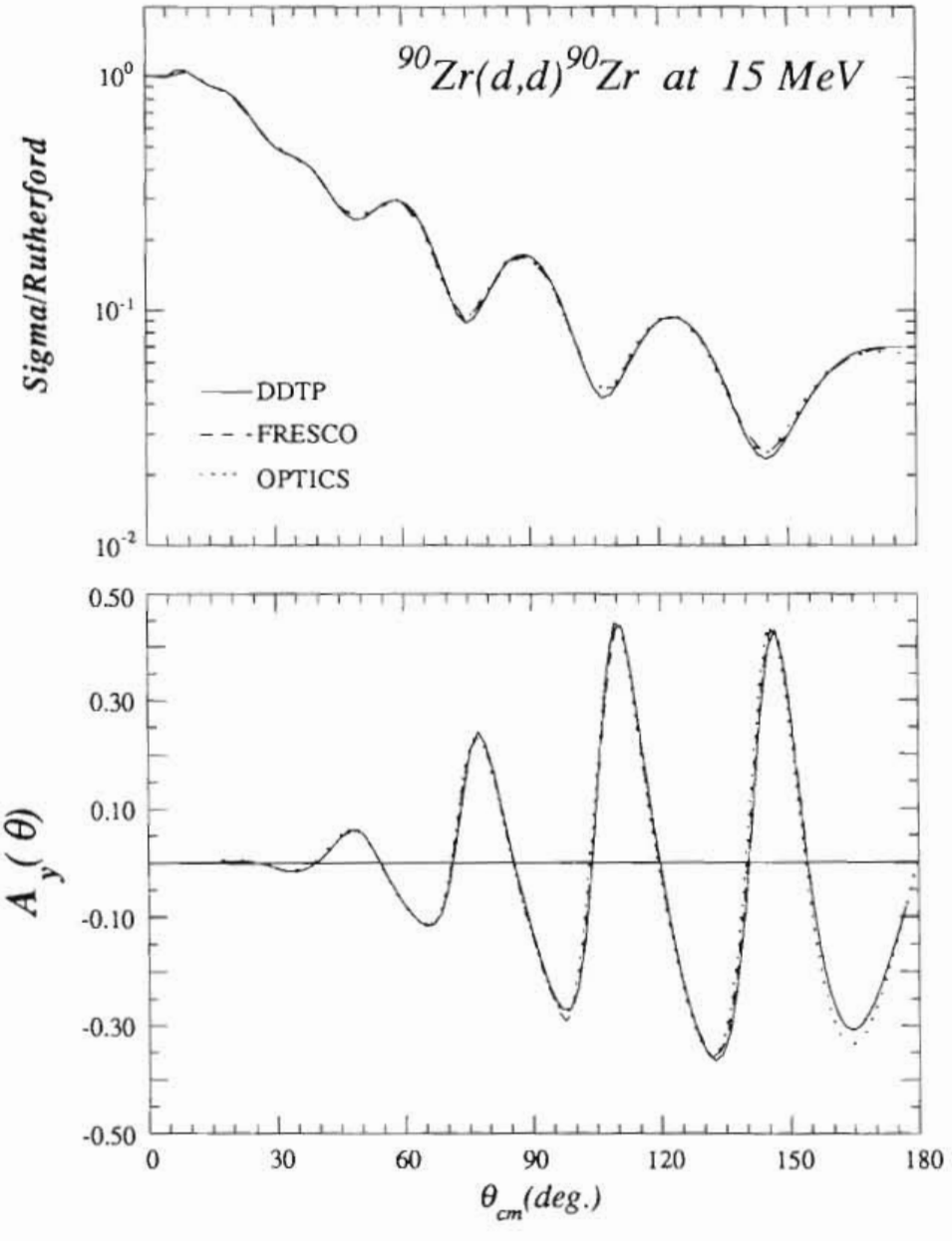

Figure 6.1 - Comparison of cross section and analyzing power calculations for three different computer codes. Data sets for these calculations do not include tensor potentials.

6.2 Optical model calculations

In Chapter II we discussed some of the more puzzling aspects of the deuteron-nucleus interaction. Among these was the apparently large discrepancy between the folding model predictions for the parameterization of the tensor interaction and those that adequately reproduced the data [God79,Tak87]. This was particularly true for the real part of the T_r potential, where it was generally determined to be significantly weaker (V < 2 MeV) than FM predictions (see TR5 in Table 6.1). One of the problems, however, in determining consistent phenomenological potentials for the T_r interaction is establishing those observables that are most sensitive to its presence while being relatively insensitive to changes in other parameters. Previous analyses have relied primarily on angular distributions of A_{xz} to establish the T_r potential, thus effectively using *one* observable to determine at least *six* parameters. With the addition of the PTO K_A in the present analysis we now have two independent observables with which to extract a reasonable form for T_r.

One of the first things to accomplish through the present optical model analysis was to try to establish the roles of the real and imaginary parts of the tensor interaction and to determine their effects on the tensor potential sensitive observables A_{xz} and K_A. In particular, it would be interesting to determine whether it is possible to generate a real T_r potential with a more significant strength (i.e. > 2 MeV) that can provide at least qualitative agreement with A_{xz} and K_A. Finally, one would like to understand how sensitive any parameterization of T_r is to changes in the other components of the optical model potential. That is, can one make relatively general statements about the effects of the T_r potential on the tensor sensitive observables even with significant changes in the central and spin-orbit parameterizations?

In Figure 6.2 are shown all the measured elastic observables for $^{90}Zr(\vec{d},\vec{d})^{90}Zr$ at E_d = 15 MeV along with optical model calculations including and not including a T_r potential. The calculations are from DDTP using a potential modified from an original "best fit" potential by Goddard [God78] for $^{90}Zr(\vec{d},d)$ also at 15 MeV. The present potentials shown result from searches on the central and spin-orbit parameters using OPTICS/MINUIT and minimizing χ^2 for the cross section and vector analyzing power distributions. The T_r potential used is the same as was determined by Goddard. These potentials are listed in Table 6.1 and are labeled as DD1 and TR1 (which from here on will be labeled DD1/TR1) and DD1/NOTR. One should note the sensitivity of both A_{xz} and K_A to the presence of the T_r potential. The TAP A_{xx} also shows some sensitivity; however, A_{xx} and A_{yy} differ from A_{xz} and K_A in the fact that much of their structure is generated and can be modified through changes in the non-tensor potential parameters. For A_{xz} and K_A the T_r parameterization is primarily responsible for their characteristic features.

	REAL			IMAGINARY		
POTENTIAL	DEPTH (MeV)	RADIUS (fm)	DIFFUSE (fm)	DEPTH (MeV)	RADIUS (fm)	DIFFUSE (fm)
DD1 - Central	87.56	1.214	0.816	17.95	1.371	0.615
Spin-Orbit	5.15	0.70	0.54	2.07	0.71	0.35
DD2 - Central	92.83	1.187	0.762	13.71	1.299	0.788
Spin-Orbit	4.45	0.60	0.44	2.39	0.64	0.28
TR1 [God79]	0.50	1.70	1.20	1.70	1.33	0.73
TR2	4.00	1.40	0.45	2.00	1.21	0.70
TR3	3.00	1.40	0.45	2.00	1.34	0.65
TR4 [Tak87]	1.64	1.31	0.41	3.14	0.92	1.36
TR5 [Kea73]	≈7.00	≈1.14	≈1.00	≈1.00	≈1.34	≈0.65

Table 6.1 - Deuteron optical potentials for 15 MeV (DD1) and 12 MeV (DD2). Both are derived from [God78]. TR2 and TR3 are T_r potentials determined in the present analysis for 15 MeV and 12 MeV respectively. The term NOTR in the text refers to the absence of a T_r potential.

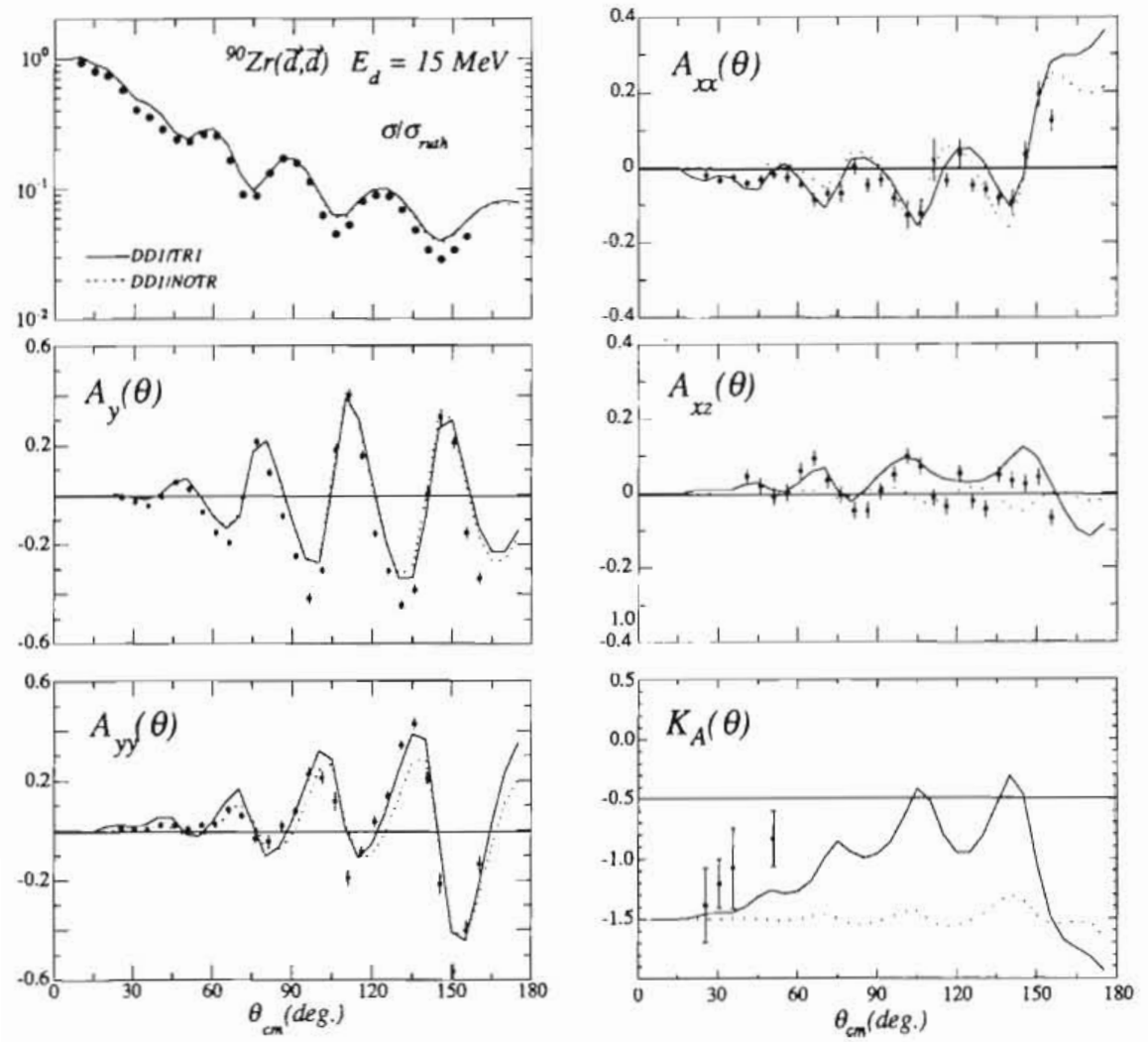

Figure 6.2 - Deuteron elastic scattering from ^{90}Zr at 15 MeV. Calculations are from optical model potentials with (solid) and without (dashed) a complex T_r tensor potential using the code DDTP. The observables A_{xz} and K_A show the strongest sensitivity to the presence of this potential. The T_r potential used in this calculation (TR1) was that determined by Goddard [God78].

The real T_r potential for TR1 is very small and plays little role in the overall structure of the tensor sensitive observables. In order to determine if a real T_r could play a more significant role, an extensive search was made on the parameters of the real and imaginary T_r potentials. The resulting potential is shown in Table 6.1 for TR2. Figure 6.3 shows calculations for both A_{xz} and K_A using DD1/TR2 and the effects of a pure real T_r, a pure imaginary T_r and the two potentials combined. From these calculations, there are some particularly interesting features to note. First, the real T_r potential does quite well in reproducing the gross features of both the A_{xz} and K_A data. For both observables, however, the general trend is to become increasingly positive. This is desirable for the K_A data but not so for A_{xz}. The imaginary T_r potential on the other hand generates exactly the opposite effect for A_{xz} (it becomes increasingly negative) while producing,for K_A, a positive trend, similar to the real T_r effects. The net result gives exactly what is needed to improve quantitatively the fit to the data. For A_{xz}, the two T_r terms interfere to produce a final prediction in good agreement with the data, while for K_A the two terms essentially add linearly to bring the calculations closer to the data. Why this occurs is in large part due to the similarity of the two potentials. Figure 6.4 shows the radial dependence for the potential TR2. This parameterization has resulted in a very similar radial dependance and diffuseness for both the real and imaginary T_r potentials. Given this particular geometry then the two observables play supplementary roles. K_A establishes the total (Real + Imaginary) strength of the T_r interaction while A_{xz} is more sensitive to the relative strengths.

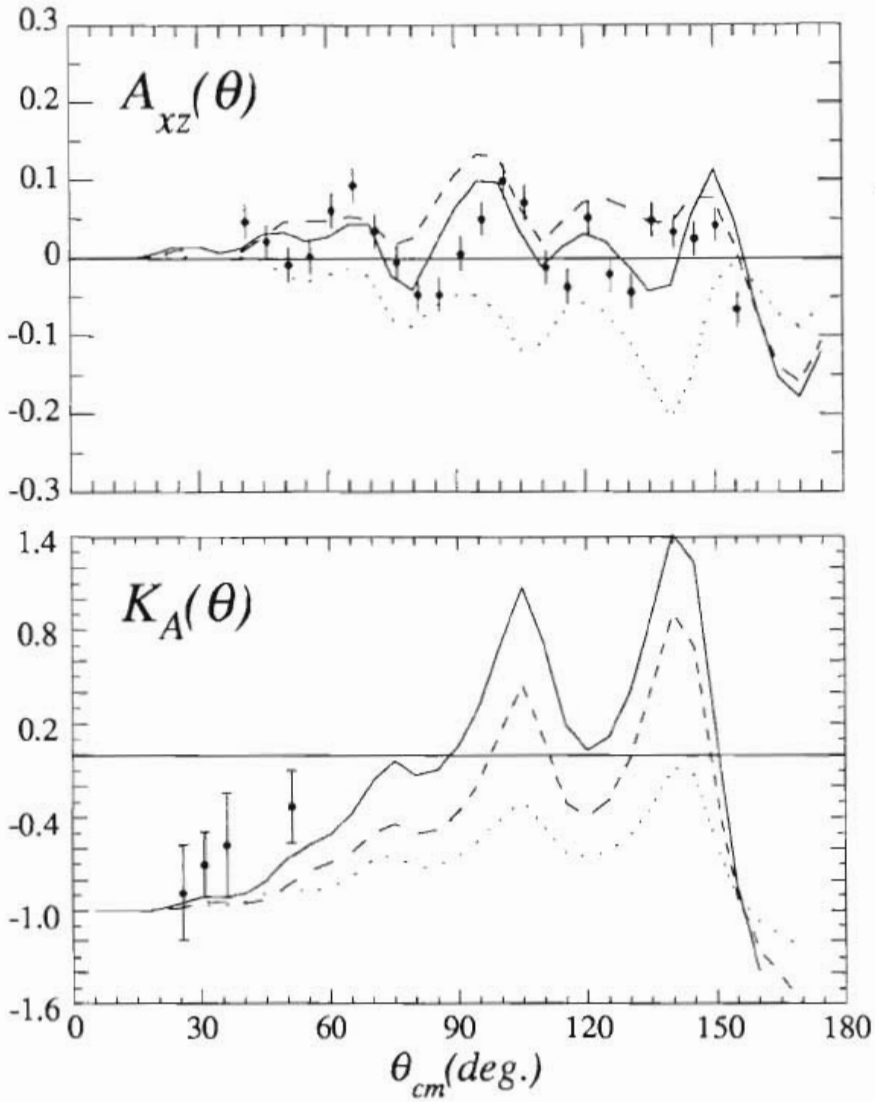

Figure 6.3 - T_r sensitive observables A_{xz} and K_A for $^{90}Zr(\vec{d},\vec{d})^{90}Zr$ at 15 MeV are shown along with optical model calculations using DD1 and the pure real (dashed), pure imaginary (dotted) and combined (solid) tensor potentials of TR1.

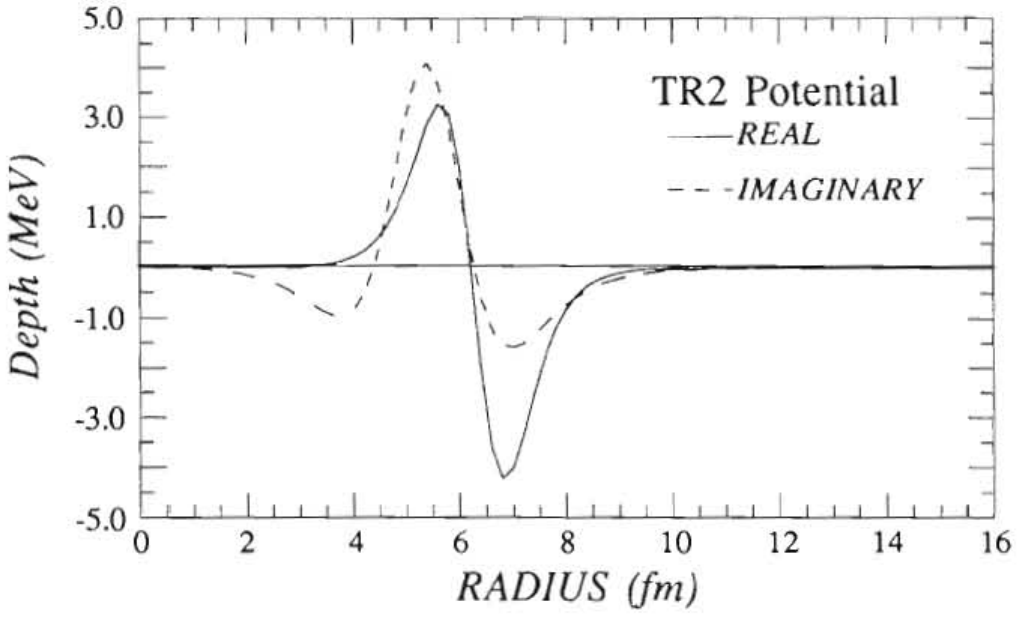

Figure 6.4 - Real and imaginary radial forms for the tensor potentials of TR2.

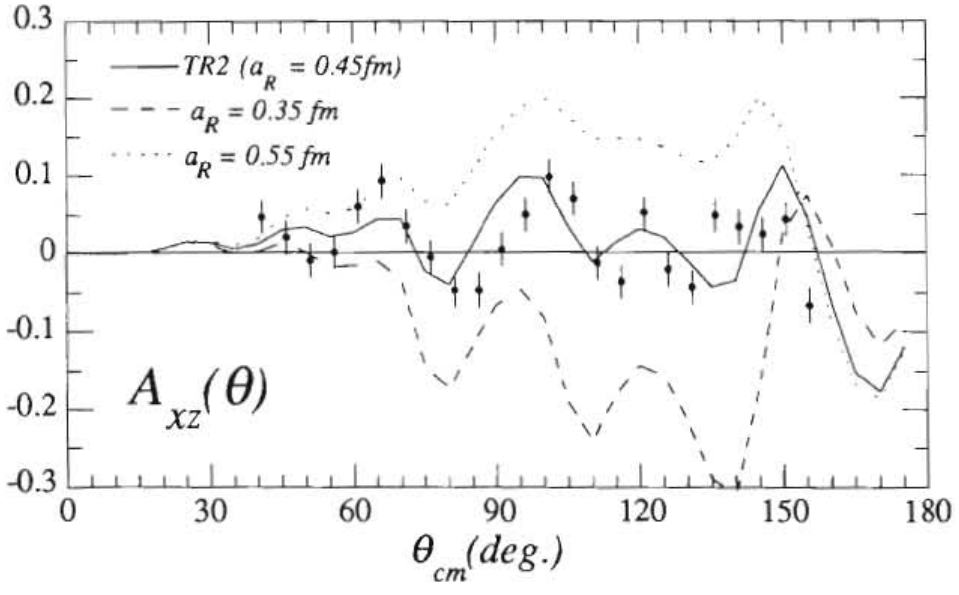

Figure 6.5 - Effects of variations in in the diffuseness parameter (a_R) for the real T_r potential. The effects are similarly detrimental for changes in the real potential radius.

Taking a closer look at the T_r potential of TR2, we see that it differs from TR1 in that is successfully establishes the real part of T_r as the dominant potential. However, it differs significantly from both TR1 and folding model predictions (TR5) in that the real diffuseness is considerably smaller, making the real TR2 potential significantly more surface-peaked in nature. The imaginary potentials for both TR1 and TR2, however, are at least in qualitative agreement with folding model predictions. One may then ask how significant the particular geometry of TR2 is for fitting the tensor observables. Through the searches involving the real T_r potential we have found that both A_{xz} and K_A are very sensitive to the real geometry, particularly if the real T_r potential is > 2 MeV. Based on these searches, we assign an uncertainty of ±0.05 fm for the real diffuseness of TR2 and ±0.07 fm for the real radius. Changes much greater than these values result in a significant deterioration of the fit. Figure 6.5 shows this deterioration in calculations for A_{xz} using real T_r potentials with varying diffuseness parameters. For K_A the predictions also get worse but it is not as sensitive. This stems largely from the fact that A_{xz} relies on the interference between real and imaginary strengths. There is a little more flexibility in the parameterization for the imaginary part of T_r, but we hesitate to assign any uncertainties because, as will be discussed in section 6.3, coupling to inelastic channels also seems to play an important role in the form of the imaginary T_r potential.

Up to now the discussion has centered around the scattering of deuterons from a single target and at one energy. One would like to test the consistency of this parameterization for T_r over a range of targets and energies. However, while that type of analysis is beyond the scope of this dissertation, some efforts were made to determine if the general trends for the real and imaginary parts of T_r were consistent despite changing the parameterizations of central and spin-orbit potentials. Results of this investigation indicated that although the fits for other elastic observables

worsened and some sensitivity to changes in central and spin-orbit parameterizations were seen in A_{xz}, the K_A predictions showed very little change at all. Overall though, for both A_{xz} and K_A, the same general dependences described earlier were seen for both the real and imaginary parts of T_r.

Taking this type of analysis one step further, we attempted to fit A_{xz} data for $^{90}Zr(\vec{d},d)^{90}Zr$ at 12 MeV using essentially the same real T_r potential as for 15 MeV (no PTO data is available at 12 MeV). Figure 6.6 shows A_{xz} data at 12 MeV from [God78] along with calculations for the real, imaginary and combined T_r potentials of DD2/TR3 in Table 6.1. We were able to keep the geometry of the real T_r term essentially the same and subsequently adjust the imaginary T_r term to provide a reasonable description of the data. This is particularly encouraging because it builds confidence in a consistent behavior of parameters for the deuteron-nucleus tensor interaction with changing energies.

On a final positive note, it should be mentioned that a comprehensive analysis of polarized deuteron elastic scattering at 22 MeV from a variety of targets was done recently [Tak87] using the same DDTP code and employing a T_r type potential to fit A_{xz} data. They found the same surface peaked trend for the real T_r potentials in a variety of targets. In addition, for deuteron scattering from ^{90}Zr, the final "best fit" real T_r potential (TR4) was very similar to the present real TR2 parameterization, although is was significantly weaker in strength. Their imaginary T_r potential was, however, significantly different from either the present 12 MeV or 15 MeV parameterizations. Considering both the present analysis and the analysis of Takei *et al.*, however, the trends of the potentials show a general decrease in the imaginary T_r radius with increasing energy, while the imaginary diffuseness increases with increasing energy.

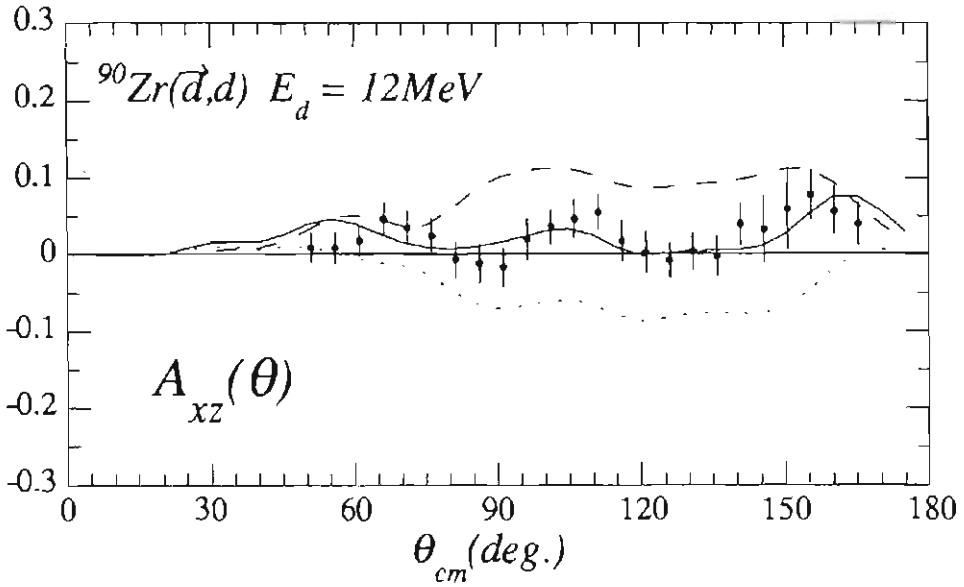

Figure 6.6 - A_{xz} for deuteron elastic scattering from ^{90}Zr at 12 MeV. Optical model calculations represent the pure real (dashed), pure imaginary (dotted) and combined tensor potentials of TR3 (non tensor parameters are given by DD2).

Intuitively, the trends seen for the tensor interaction are encouraging. For the imaginary T_r potential, as the energy of the incident deuteron increases, one would expect first that contributions from competing inelastic processes would change but also that they would be increasingly important toward the nuclear interior. For the real T_r potential there is a consistent form which does not seem to be significantly energy dependent. While this potential form does not agree with folding model predictions, its apparently weak energy dependence is consistent with the FM.

Postscript to the optical model analysis

One of the limitations in a phenomenological investigation of this type is the ambiguities that exist for the potential parameterizations. It is difficult to prove

whether one prescription can provide a better physical interpretation than another. The preceding analysis gives an alternative prediction for the d + ^{90}Zr T_r interaction with a more consistent energy dependance than that determined by Goddard [God78]. In both analyses, however, there is agreement that the folding model prescription for the deuteron-nucleus tensor interaction does not describe the data well.

There are other questions to consider pertaining to these analyses. First, both have used a T_r potential form that was derived to approximate the folding model T_r interaction. Altering the parameterizations for this form to describe the data may not generate a potential which is appropriate to describe the tensor interaction. Other, more general, potential forms should be considered. This has been attempted recently in an analysis of deuteron elastic scattering from ^{40}Ca at 52 MeV [Erm87]. Ermer *et al.* used a model-unrestricted Fourier-Bessel expansion of the central and spin-orbit optical potentials. This method frees one from the use of restricted potential forms like the Woods-Saxon shape and allows the determination of the potential radial shapes deep within the nuclear interior. In this manner, Ermer *et al.* were able to reproduce very well the complicated structure of the cross section and vector analyzing power at 52 MeV. It would be useful to see an extension of this work to include the tensor interaction.

Another complication that exists for low-energy deuteron scattering experiments is the limitation of the deuteron ability to probe the nuclear potential. At 15 MeV the effective wave length of the deuteron is only about 5 fm, so its ability to probe potential structures within a 3 fm range (see Figure 6.4) is limited. An advantage to making experiments at slightly higher energies is that one increases the sensitivity of the probe. At 52-56 MeV the incident deuteron wavelength is doubled. Data at these energies are, however, somewhat limited, particularly for the analyzing power A_{xz}. This comes from difficulties in orienting the spin when using cyclotrons for acceleration of the beam. Recently, tensor analyzing power data was taken at

56 MeV for deuteron elastic scattering from several targets including ^{90}Zr [Mat86]. They parameterized the tensor interaction, using the same prescription as the present analysis, with DDTP. They found the real T_r potential to be very large in comparison with lower energy analyses (2-5 MeV), while the imaginary T_r potential was very small (0.1-0.6 MeV). In order to gauge the sensitivity of polarization transfer measurements to the tensor interaction at 56 MeV, we performed an optical model calculation for d+^{90}Zr using the potential parameters given in [Mat86]. The results are shown in Figure 6.7 for A_{xz} and K_1 ($K_y^{z'z'}$ - $1/2A_y$). The calculation using the complex T_r potential gives a reasonably good description of the A_{xz} data, particularly at forward angles. It is interesting to note for this parameterization that the imaginary T_r is primarily responsible for the generation of the strong oscillatory pattern in both observables even though it is very weak (0.248 MeV). It is apparent though that the PTO exhibits a strong sensitivity to the T_r potential used, and including even just a few data points could provide useful information on the adequacy of their potential parameterization.

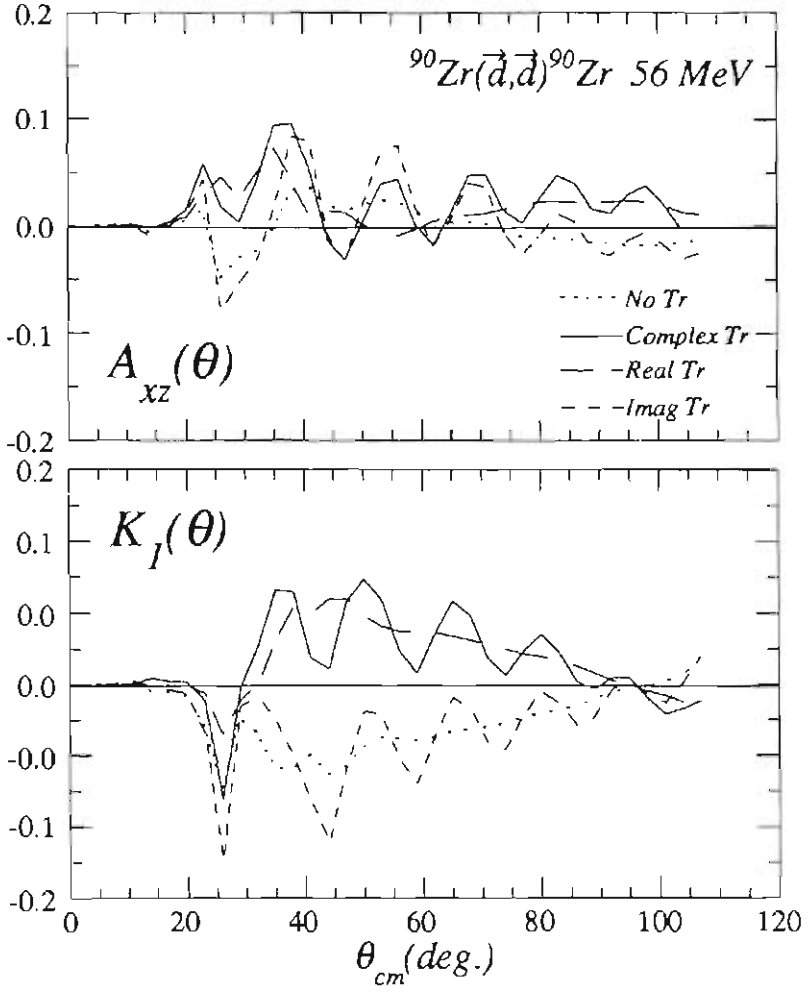

Figure 6.7 - Calculations of the T_r Sensitive Observables A_{xz} and K_I for $^{90}Zr(\vec{d},\vec{d})^{90}Zr$ at 56 MeV are shown using potentials from [Mat86]. In both observables the real T_r (long dash) and Imaginary T_r (dashed) "add" to generate the combined T_r potential fit (solid curve). This complex T_r curve represents a reasonably good fit to the A_{xz} data of [Mat86] at forward angles ($\theta < 60°$).

6.3 Coupled reaction channel calculations

Motivation for coupled channels

In the preceding section we found that we were unable to provide a reasonable description of the tensor sensitive observables using a real T_r potential predicted by the folding model. In addition, there was a significant variation of the imaginary T_r potential parameterizations with energy. This leads one to ask how important incorporating additional degrees of freedom for the deuteron is to generation of an effective potential for the elastic scattering channel. To this point we have only touched on the possible significance of reaction channel coupling (see section 2.3). In general though, coupling to additional channels has the same effect as adding *complex* and *non-local* terms to the elastic scattering potential. Furthermore, if one includes spin degrees of freedom, the effective potential generated may include both vector and tensor components. This, of course, depends on the nature of the coupled inelastic channel states. By using the FRESCO code and observing the effects on the tensor observables A_{xz} and K_A we have the means to study the importance of these non-local contributions to the deuteron-nucleus tensor interaction.

The most dominant non-elastic states for deuteron scattering from ^{90}Zr at 15 MeV are the neutron stripping, (d,p), channels. Given the significant role this channel seems to play at sub-Coulomb energies for the elastic tensor interaction ([Tos87] and section 2.3), we have attempted here to study quantitatively the effects of (d,p) coupling at 15 MeV. Cross sections for the three strongest states were extracted (see section 5.4) for use in the present analysis. The CC calculations then treat explicitly these states along with the elastic channel. Details of the properties of these states including excitation energy (E_x), spin (j), parity (π), neutron angular momentum transfer (l_n), neutron separation energy (S_n) and the single particle states in ^{91}Zr are given in Table 6.2. Also shown in Table 6.2 are the optical potentials for

the p + ^{91}Zr partition and the neutron-bound state geometry used for the present analysis. This information was taken from the global nucleon potential analysis of Varner [Var86].

E_x (MeV)	j^π	l_n	S_n (MeV)	SP-states
1) 0.00	5/2+	2	7.194	$2d_{5/2}$
2) 1.20	1/2+	0	5.994	$3s_{1/2}$
3) 2.03	3/2+	2	5.154	$2d_{3/2}$

p + ^{91}Zr Optical Potential -- V_0 = 51.97 MeV r_0 = 1.196 fm a_0 = 0.69 fm
W_D = 8.58 MeV r_{WD} = 1.23 fm a_{WD} = 0.72 fm
V_{SO} = 5.94 MeV r_{SO} = 1.07 fm a_{SO} = 0.65 fm

Table 6.2 - Details for the ^{90}Zr(d,p)^{91}Zr states used in the coupled-channels analysis of the deuteron elastic scattering. The neutron bound state potential geometries used were identical to the proton potential geometries.

Details of the coupled-channels calculation

The coupled reaction channels(CRC) code FRESCO [Tho88] is unique in that it allows for finite-range transfer interaction coupling. This is done through an iterative technique where the stored non-local interaction kernels for each iteration are used to integrate the wave functions, which are in turn used to generate the source terms (interaction kernel) for the next iteration. The iterations are continued until there is convergence of the transition amplitudes. As an example, if we consider the coupled-channels calculation for elastic (d,d) on ^{90}Zr coupled to neutron transfer (d,p), then the first iteration (d,d)-->(d,p) (given incident deuteron potentials and information in Table 6.2) simply calculates the *one-step* DWBA for the (d,p) states. The second iteration (d,d)-->(d,p)-->(d,d) recalculates the elastic channel scattering including the *two-step* neutron transfer and subsequent pick-up reaction. Three iterations would modify the original (d,p) calculation and so on. An indication that this iterative method

has converged comes when, for instance, the elastic scattering amplitudes for four iterations are essentially the same as those for six iterations. For particularly strong couplings between states many iterations may be needed for convergence.

One of the complications that arises when coupling between two different mass partitions like $d + {}^{90}Zr$ and $p + {}^{91}Zr$ is that the basis sets for calculation of wave functions are not orthogonal to each other. In order to make a correct calculation of a coupling between these partitions, one must include the effects of direct overlap of deuteron and bound-state neutron wavefunctions independent of the n-p interaction. The problem is that the effects these non-orthogonal terms have by including them in the calculation is not necessarily intuitively understood. In the past, these terms have been ignored with the hope that their effects would be small, but primarily because of the increased computing problems that arise when incorporating them into a coupled-channels calculation. FRESCO allows inclusion of a non-orthogonality supplement to the finite-range coupled-channels (FRCC) calculation[1]. Although this significantly increases the time for a given calculation, we can get an idea of their relative importance for determination of a spin-dependent potential. The parameterization of the non-orthogonal supplement used in the present calculations was provided by Tostevin [Tos90].

Finally, in order to make a quantitative study of deuteron-nucleus tensor interaction in the CC framework, one must provide FRESCO with a realistic deuteron wavefunction that includes both S- and D-state components. Without the deuteron D-state there can be no significant tensor interaction generated through the coupling. As a T_r operator form is generated by including a deuteron D-state, so is the possibility of tensor effects being generated via $l_n = 2$ transfer reactions; however, the coupling

[1]Including non-orthogonal terms in the coupled channels calculation increases the calculation time about a factor of three. Normal CPU time on a VAX station 3200 goes from ≈1.5 hours for the normal coupled-channels calculation to almost 5 hours.

sensitivity is suppressed if the D-state is not present in the n-p interaction. This stems primarily from hierarchies in the angular momentum algebra for the interaction. For the present calculations we used the Reid soft-core potential [Rei68] for the n-p interaction to generate the S- and D-state wavefunctions.

Results of the FRCC calculations

Preliminary to the CC calculations we first made a series of finite-range DWBA calculations (one iteration) for the $^{90}Zr(d,p)^{91}Zr$ states. Using the information on these states included in Table 6.2 and the deuteron optical potential DD1/TR2 described in Table 6.1, the spectroscopic factors for each state were adjusted to bring the calculations into agreement with the cross section data. Figure 6.8 shows the results of DWBA calculations, along with the data for all three states. The corresponding spectroscopic factors used for (d,p) states 1, 2 and 3 were 0.72, 0.61 and 0.58, respectively. One can see from the figure that there is reasonably good agreement for the cross section data for states 1 and 3. State 2 calculations exhibit some discrepancies. This is probably an indication of possible deficiencies in the deuteron optical potential; However, as stated previously, it is the $l_n = 2$ transfer states which are expected to provide the largest contribution to the effective elastic tensor interaction through coupling.

Given the above determined coupling strengths a series of FRCC calculations was done to determine iteration criteria for convergence. We found that there was satisfactory convergence for the elastic observables at *four* iterations, both for calculations including and excluding non-orthogonal corrections to the coupling. Results of the full CC calculations along with the optical model calculation using DD1/TR2 are shown in Figure 6.9.

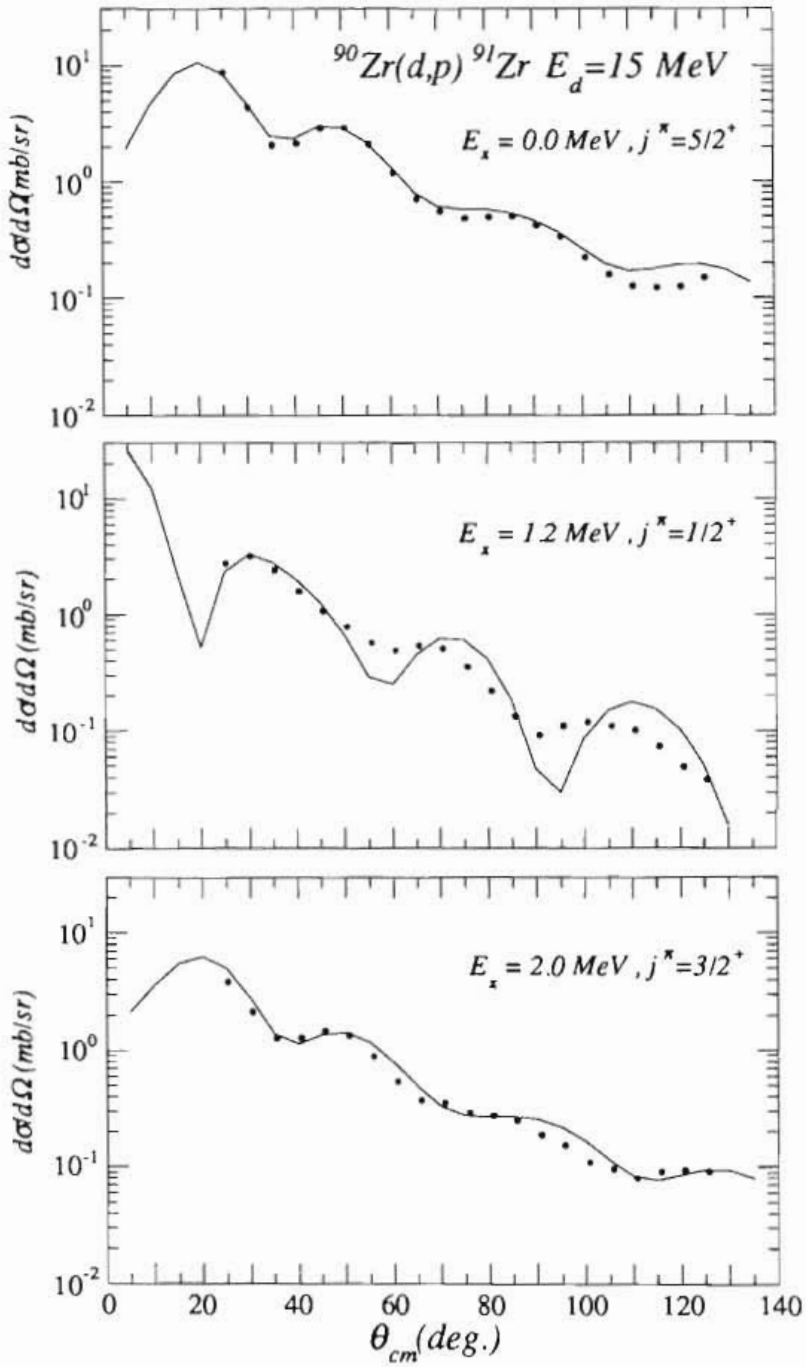

Figure 6.8 - Cross section measurements are shown for three states corresponding to excitations of 0.0, 1.20 and 2.04 MeV for the $^{90}Zr(d,p)^{91}Zr$ reaction at 15 MeV. Finite-range DWBA calculations using FRESCO are represented by the solid curve. The deuteron-nucleus potential used in the calculation is DD1/TR2.

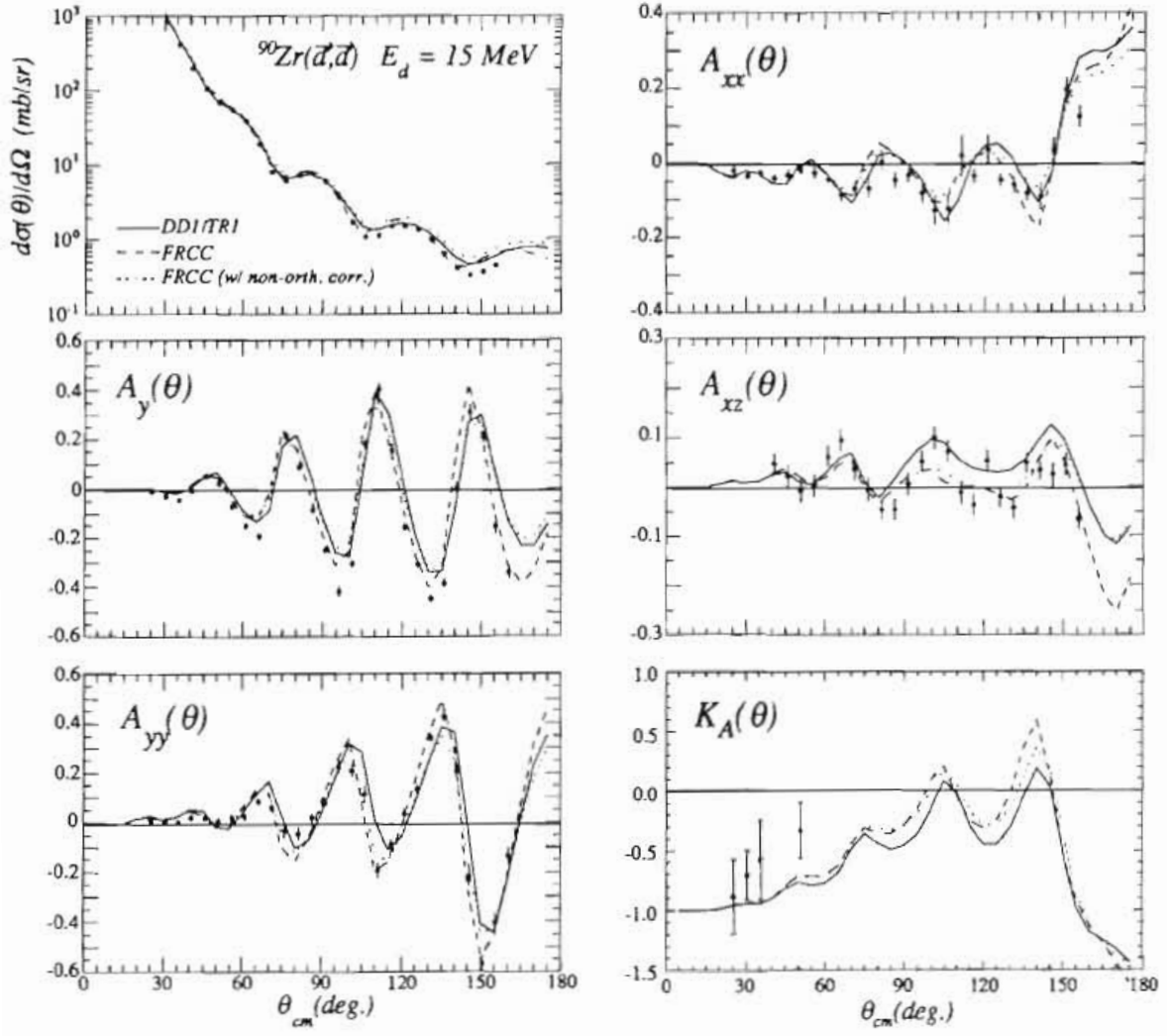

Figure 6.9 - Deuteron elastic scattering from ^{90}Zr at 15 MeV. Calculations include an optical model prediction (solid curve using DD1/TR1) as well as finite range coupled-channels (FRCC) calculations with and without non-orthogonality corrections (dotted and dashed curves respectively). Note that A_{xz} is most affected by the coupling.

There are several interesting points to note from these calculations. Firstly, the effects of (d,p) coupling are in general small. Changes in most observables are only on the order of 10%. What is more interesting is the effect of including non-orthogonal corrections. This seems to contribute additional corrections to observables on the same order as the coupling itself. The largest change, being the reduction in cross section, is not particularly unusual, in that it is expected when explicitly including inelastic channels. Also, it does not necessarily represent generation of any large spin-dependent potentials. More to the point, one should look specifically at the tensor observables A_{xz} and K_A. While K_A does not show a large change with coupling, the A_{xz} calculation does show a significant change in its general structure.

In order to understand better the type of tensor potential being generated through coupling, additional calculations were performed removing the explicit T_r potential for the deuteron optical potential. In this manner any changes in A_{xz} and K_A predictions could be associated primarily with the coupling. Figure 6.10 shows the CC calculations for both A_{xz} and K_A as well as an optical model calculation using the input potential DD1/NOTR. Here one can see more specifically the tensor effects due to the coupling. The first thing to note is that the non-orthogonality corrections seem to enhance the overall tensor interaction generated. By this we refer to the shift towards increasing negative values for A_{xz} and positive values in K_A. If we examine this structure of both observables more closely this tensor effect can be associated with an imaginary T_r potential using a geometry very similar to that of TR2 in Table 6.1 but only having about 15-20% of its strength. This is particularly encouraging because since these contributions are small perturbations to the direct elastic scattering potential one should essentially be able to add the coupled-channels tensor potential to any explicit T_r potential included in the elastic channel.

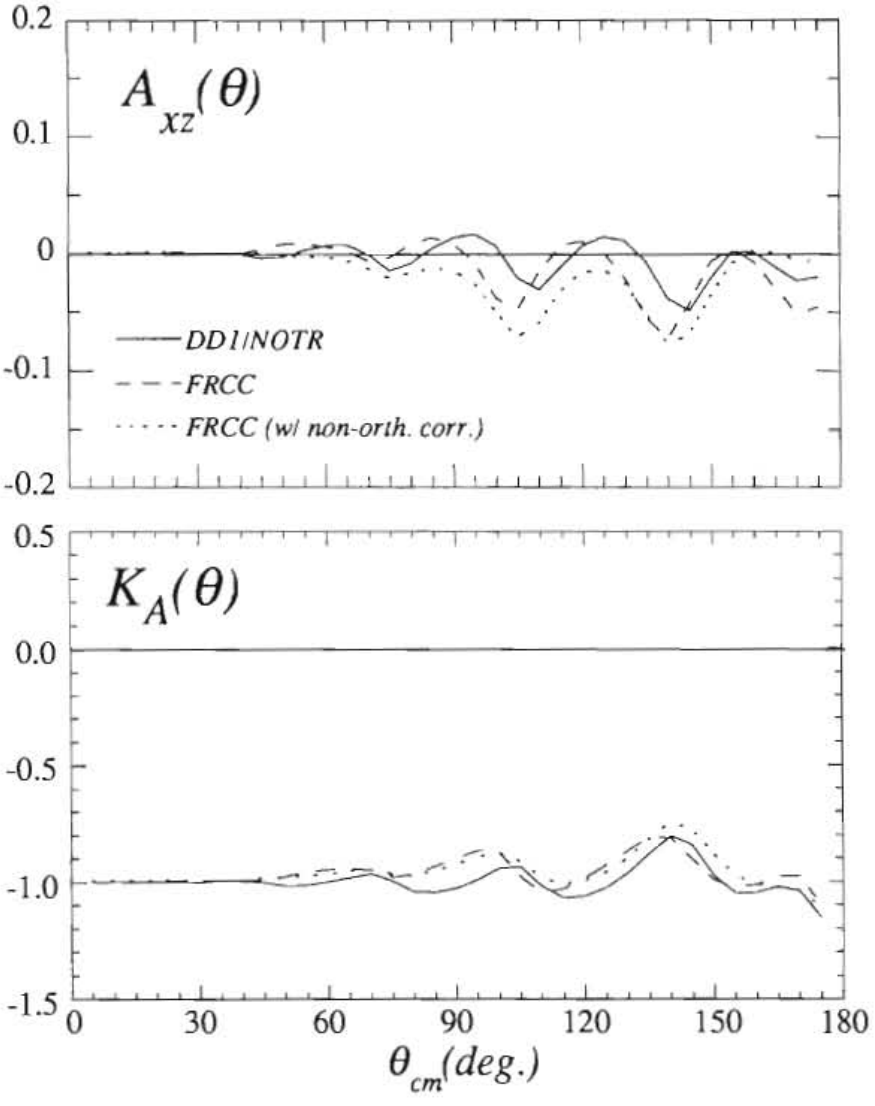

Figure 6.10 - T_r sensitive observables A_{xz} and K_A for $^{90}Zr(\vec{d},\vec{d})^{90}Zr$ at 15 MeV are shown, along with an optical model calculation using DD1/NOTR (solid curve), as well as finite-range coupled-channels calculations (coupling to the (d,p) channel) with and without non-orthogonal corrections (dotted and dashed curves respectively).

Effects of other inelastic processes

Up to now not much has been said about contributions from other inelastic processes. We have concentrated on the (d,p) channels because they are the most strongly excited. Given the effects of (d,p) coupling, one may also expect some contributions from coupling to (d,n) channels. They have a comparable Q-value and cross section on ^{90}Zr targets at this energy. Also ^{90}Zr has a 2^+ state at approximately 2 MeV of excitation which is capable of contributing to an effective tensor interaction through the two step process (d,d´)-->(d´,d).

Information available to attempt these types of calculations is somewhat limited. To our knowledge no data exist for $^{90}Zr(d,n)^{91}Nb$ at 15 MeV. However, information was found for this reaction at 12 MeV [Hor72]. Forward-angle cross sections and spectroscopic information for several states in ^{91}Nb were determined in this analysis. The most prominent identifiable state determined under 3 MeV of excitation was the ground state for ^{91}Nb ($j^\pi = 9/2^+$, $l_n = 4$, spect. factor = 0.97). Its cross section was still approximately 2-4 times smaller than the strongest (d,p) cross sections at 15 MeV.

Nevertheless, we attempted a FRCC calculation coupling the (d,n) to the elastic (d,d) using the information in [Hor72] and interchanging the roles of the neutron and proton potentials given in Table 6.2. DD1/NOTR was used for the incident deuteron potential once again. Figure 6.11 shows, for the tensor observables A_{xz} and K_A, FRCC calculations with and without non-orthogonality corrections, as well as a simple optical model calculation (DD1) with no T_r potential included. Interestingly, in these calculations we see an effect of the same order of magnitude but different in nature to the (d,p) coupling effects. In this case there is a large phase shift generated and only a minimal "off-axis" trend in the calculation . The "off-axis" trend

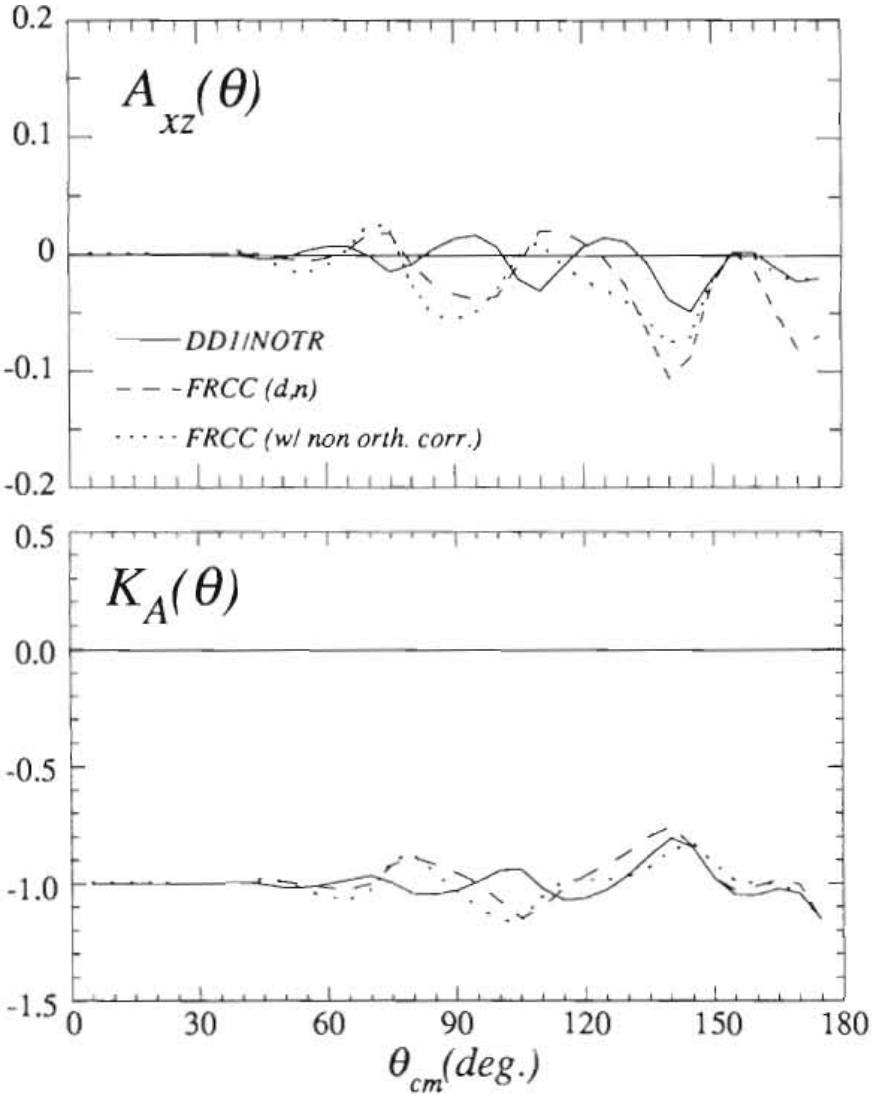

Figure 6.11 - T_r sensitive observables A_{xz} and K_A for $^{90}Zr(\vec{d},\vec{d})^{90}Zr$ at 15 MeV are shown, along with an optical model calculation using DD1/NOTR (solid curve), as well as finite-range coupled-channels calculations (coupling to the (d,n) channel) with and without non-orthogonality corrections (dotted and dashed curves respectively).

is consistent with the (d,p) coupling effects. However, unlike the (d,p) calculations, the phase shift can be generated not only with an effective T_r potential but also with changes in the other optical potential parameters. So, while it is somewhat less clear what role (d,n) coupling plays for the elastic scattering spin-dependent potentials, it nevertheless has a measurable effect which probably should not be ignored.

The question of coupling to excited states in ^{90}Zr is significantly less complicated than for the transfer reactions. One does not have to worry about non-orthogonality corrections or iterative convergence. Using FRESCO, all states defined in the d + ^{90}Zr mass partition may be blocked together and coupled exactly. Using this procedure we made several calculations in order to gauge the magnitude of the effects for the elastic channel. Information for these calculations was obtained from [Bak75] who made both elastic and inelastic scattering measurements for ^{90}Zr at 15 MeV. They measured cross sections for the 2.18 MeV 2^+ state in ^{90}Zr that were at least an order of magnitude smaller than the (d,p) cross sections for the same energy; therefore, we did not expect to see a large contribution from coupling to this intermediate state. Our calculation used a rotational model deforming the Coulomb and elastic central and spin-orbit potentials. The deformation parameter $\beta_2 = 0.045$ was taken from [Bak75]. The results give no substantial contribution to any of the elastic scattering observables. As this was the most prominent excited state for ^{90}Zr at this energy, it is expected that including other states should lead to similar or smaller effects.

As a final note to this discussion on inelastic processes, it seems advisable to comment on some aspects that were not investigated. The most significant of these is deuteron break-up, (d,np). In Chapter II some discussion of the history and problems associated with including deuteron break-up effects was made, and while there has been much evidence that (d,np) may make significant corrections to the elastic scattering channel, the calculations are very difficult to do properly. In principle

FRESCO could be used to attempt such calculations using a method similar to the CDCC (coupled discretized continuum channels) technique of [Yah82]. Using this method, however, one must define continuum states within a specified energy bin and associate a spin and parity (j^{π}) to it. Then, using a similar iterative technique to the present (d,p) and (d,n) calculations, the effect on the elastic channel of coupling to these "discretized" states may be calculated. Although the break-up cross sections at 15 MeV are not as large to those at 56 MeV [Ise89] their contribution to the deuteron-nucleus interaction added in with (≈20%) contributions from other inelastic processes should in general be significant (not just for the tensor interaction) and important to a full understanding of the deuteron-nucleus reaction mechanism.

Chapter VII

Summary and Conclusions

7.1 Summary and conclusions

We have measured and analyzed in the course of this work angular distributions of a number of polarization observables for the elastic scattering of 15 MeV deuterons from ^{90}Zr. The measurements include the vector analyzing power A_y and tensor analyzing powers A_{yy}, A_{xx} and A_{zz}. Also included is the first measurement of polarization transfer observables for deuteron scattering from a heavy nucleus (A > 4). The PTO of interest determined for the present experiments was the combination $3K_y^{z'z'} + K_{yy}^{z'z'}$. Making these polarization transfer measurements required the design, construction and calibration of two compact and efficient deuteron polarimeters. These polarimeters used the $^3He(d,p)^4He$ reaction as an analyzer and a vane-type design scattering into five detectors (to the left, right, up, down and 0°) to measure the polarization of the elastically scattered deuterons.

In addition to the elastic scattering observables, absolute cross section distributions for the $^{90}Zr(d,p)^{91}Zr$ reaction at 15 MeV have been measured corresponding to states in ^{91}Zr of (E(MeV), j^π) = (0.0, 5/2$^+$), (1.20, 1/2$^+$) and (2.04, 3/2$^+$). These states represent the strongest non-elastic channels for deuteron scattering on ^{90}Zr at this energy. These data, along with additional information involving deuteron induced reactions on ^{90}Zr at both 12 MeV and 15 MeV [Har72,

Hor72, Bak75, God79], were used in an attempt to better establish the role and possible origins of the deuteron-nucleus tensor interaction.

The data were analyzed using two methods. First, an optical model analysis was done using the elastic observables to establish a consistent form for the real T_r potential at both 15 and 12 MeV. The form that was determined was substantially stronger than that used in previous analyses [God79]. The present analysis also differs from previous work in that tensor analyzing power data (primarily A_{xz}) as well as PTO data were used almost exclusively to determine the T_r potential forms. In the present parameterization, these two observables provide supplementary information as well as the most sensitive information for establishing this potential. Results of our analysis indicate a real T_r potential which is primarily surface-peaked. This differs from more diffuse folding model predictions, which have been previously shown not to agree with the data [Kea73, God79]. It is, however, relatively consistent with previous determinations of T_r using only tensor analyzing power data at 22 MeV [Tak87]. Conversely, imaginary T_r potentials were found to vary somewhat with deuteron energy but are in qualitative agreement with folding model predictions. The changes in the imaginary T_r potential with increasing energy, which include a decreasing radius and increasing depth and diffuseness, can be interpreted as being primarily associated with competing non-elastic processes.

A second and more sophisticated approach to analysis of the data used coupled reaction channels calculations to provide a quantitative measure of the spin dependent potential generated for elastic scattering from coupling to inelastic channels such as (d,p). We found that coupling to (d,p) channels produced an effect which could be equivalently generated by an imaginary tensor potential approximately 15-20% of the strength and similar in geometry to that needed to fit the elastic observables. Also, by including non-orthogonality corrections to these calculations we found additional contributions to the tensor interaction which could not be ignored. Finally, in addition

to the (d,p) coupling, evidence was also found for contributions of similar magnitude from coupling to the (d,n) channel. The spin dependent nature of these contributions, however, was less apparent.

It is increasingly evident from the work presented here that if one is to make a more global determination of the deuteron-nucleus tensor interaction, additional scattering information, beyond just the tensor analyzing power measurements, in the form of polarization transfer observables can provide very sensitive constraints. It also appears that the numerous competing processes that occur when the deuteron and nucleus interact (such as stripping, pickup and break-up), although individually small, can combine to play a very significant role in shaping the effective elastic scattering potentials. This is particularly true for the deuteron-nucleus tensor interaction, since it is a relatively small contribution to the overall interaction. The fact that these non-elastic contributions are also dependent both on incident deuteron energy and the target used make the problem even worse. So at present, it is difficult to say exactly what type of tensor interaction one should use for deuterons scattering from a specific nucleus at a specific energy.

7.2 Epilogue: suggestions for future work

The design of the deuteron polarimeters used in this work stemmed initially from experimentalists' questions on the feasibility of making a polarimeter for *general* polarization transfer measurements in a simple and effective manner. Theoretical motivation for measurement of specific PTO unfortunately came later. In hindsight, it is the author's observation that the methods used to acquire this new information concerning the deuteron-nucleus tensor interaction were not ideal. That is not to say that this type of information is not important. It is very important and worthwhile to pursue in future projects; however, there are a number of caveats.

The natural extension of this work is to make further polarization transfer measurements at different energies and for different targets. This need not be as arduous a task as it appears to be at first glance. A number of simplifications to the experimental technique can be made. First, the polarimeter used in the present experiments was designed as a device capable of measuring a number of polarization transfer coefficients and in fact is not optimized for the present PTO measurements. If one is solely interested in measuring the tensor sensitive observable $K_y^{z'z'}$, then the polarimeter needs only a single 0° detector to determine the scattered moment $p_{z'z'}$ as well as a passing ΔE detector to identify the appropriate scattered deuterons. In this manner the entire polarimeter assembly could be compacted and more devices could be placed inside the existing scattering chamber. Data could be taken using a two spin state mode switching from pure vector polarized deuterons to unpolarized deuterons. Given the current operation modes for the new atomic beam polarized source at TUNL [Cle90] this would be the preferred operating method regardless of the polarimeter used.

Another extension of this work involves measurement not only of elastic polarization observables but also observables of a number of non-elastic channels as well. These might include polarization observables for (d,p) or (d,n), or even (d,^{3}He) and (d,t) channels. It is also reasonable to attempt measurements of deuteron break-up cross sections and analyzing powers, particularly for a number of energies for a given nucleus. All such information is useful in providing more quantitative information about the interaction of the deuteron with nuclei, and given the lingering deficiencies of the deuteron scattering analyses that exist today, there seems reasonable justification in undertaking those projects. What is particularly exciting about acquiring all this new information is that computer codes like FRESCO and the CDCC code [Yah82] are growing in sophistication and are able to handle increasingly realistic and complex systems both faster and more accurately than previously.

Appendix A

The Optical Potential For Deuteron Scattering

Compiled below are the parameterized forms for the deuteron optical potential used in code DDTP. Potential forms are not shown for the T_p and T_L type tensor potentials because they were not used in the present analysis (see section 6.2). Information about how DDTP can implement these potentials as well as more specific information on the general functions of the DDTP code can be found in [God78].

The elastic scattering of deuterons by a nucleus is assumed to be described by a complex local potential of the form

$$V(r,\mathbf{S}) = V_{Coul}(r) + [V_C(r) + iW_D(r)] + [V_{SO}(r) + iW_{SO}(r)]\mathbf{L}\cdot\mathbf{S} + [V_{T_r}(r) + iW_{T_r}(r)]T_r\,, \qquad (A.1)$$

where

$$T_r = (\mathbf{S}\cdot\boldsymbol{R})^2 - \frac{2}{3} \qquad (A.2)$$

and $\mathbf{S}$, $\boldsymbol{R}$ and $\mathbf{L}$ are the deuteron spin, position, and orbital angular momentum respectively. The Coulomb potential, $V_{Coul}(r)$, is taken to be the potential due to a uniformly charged sphere of radius $1.30A^{1/3}$ fm, where A is the atomic mass of the target. The six other radial functions $V_i(r)$ and $W_i(r)$ are the form factors corresponding to the real and imaginary parts of the central, spin-orbit and tensor potentials. A volume imaginary term to the central potential is not used in this

parameterization. The potential forms for each term were taken to be Woods-Saxon, or Woods-Saxon derivatives, each parameterized by a depth V_i, a radius R_i, and a diffuseness a_i. They are as follows:

$$V_C(r) = -V_1(1 + e^{x_1})^{-1} \quad \text{(Woods-Saxon)}, \tag{A.3}$$

$$W_D(r) = 4V_2\frac{d}{dx_2}(1 + e^{x_2})^{-1} \quad \text{(W-S derivative)}, \tag{A.4}$$

$$V_{SO}(r) = \lambda_\pi^2\frac{V_3}{r}\frac{d}{dr}(1 + e^{x_3})^{-1} \quad \text{(Thomas)}, \tag{A.5}$$

$$W_{SO}(r) = \lambda_\pi^2\frac{V_4}{r}\frac{d}{dr}(1 + e^{x_4})^{-1} \quad \text{(Thomas)}, \tag{A.6}$$

$$V_{T_r}(r) = -\lambda_\pi^2 V_5 r\frac{d}{dr}\left[\frac{1}{r}\frac{d}{dr}(1 + e^{x_5})^{-1}\right] \quad \text{(2nd derivative)}, \tag{A.7}$$

$$W_{T_r}(r) = 4\lambda_\pi^2 V_6 r\frac{d}{dr}\left\{\frac{1}{r}\frac{d}{dr}\left[\frac{d}{dx_6}(1 + e^{x_6})^{-1}\right]\right\} \quad \text{(3rd derivative)}, \tag{A.8}$$

where $x_i = (r - RA^{1/3})/a$ and $\lambda_\pi^2 = 2.0$ fm^2. Hence there are a total of 18 parameters which may be adjusted to produce the best agreement with the data.

The forms shown for the T_r potentials were derived from folding model calculations for the deuteron [Kea73]. They are expected to give a reasonably good approximation to the folding model T_r predictions with use of appropriate parameters. For the case of ^{90}Zr at 15 MeV approximate values for these parameters are,

$$V_{T_r}(r): \quad V_5 \approx 7 \text{ MeV} \qquad R_5 \approx 1.14 \text{ fm} \qquad a_5 \approx 1.0 \text{ fm}, \tag{A.9}$$

$$W_{T_r}(r): \quad V_6 \approx 1 \text{ MeV} \qquad R_6 \approx 1.30 \text{ fm} \qquad a_6 \approx 0.87 \text{ fm}. \tag{A.10}$$

Appendix B

Relationships Between Spherical and Cartesian Descriptions of the Operators and Observables for Spin-1 particles.

The relationship between the spin-1 Cartesian operators (S_i and S_{ij}) and the spherical tensor operators (τ_{kq}) are defined as follows:

$$\tau_{00} = 1 \ \ (3\times3 \ \textit{unit matrix}) \qquad S_x = \frac{-1}{\sqrt{3}}(\tau_{11} - \tau_{1\text{-}1}) = \frac{-2}{\sqrt{3}}\mathrm{Im}(\tau_{11})$$

$$\tau_{10} = \sqrt{\frac{3}{2}}S_z \qquad S_y = \frac{i}{\sqrt{3}}(\tau_{11} + \tau_{1\text{-}1}) = \frac{-2}{\sqrt{3}}\mathrm{Re}(\tau_{11})$$

$$\tau_{1\pm1} = \frac{-}{+}\frac{\sqrt{3}}{2}(S_x \pm iS_y) \qquad S_z = \sqrt{\frac{2}{3}}\tau_{10}$$

$$\tau_{20} = \frac{1}{\sqrt{2}}S_{zz} \qquad S_{xy} = \frac{-i\sqrt{3}}{2}(\tau_{22} - \tau_{2\text{-}2}) = \sqrt{3}\mathrm{Im}(\tau_{22})$$

$$\tau_{2\pm1} = \frac{-}{+}\frac{1}{\sqrt{3}}(S_{xz} \pm iS_{yz}) \qquad S_{xz} = \frac{-\sqrt{3}}{2}(\tau_{21} - \tau_{2\text{-}1}) = -\sqrt{3}\mathrm{Re}(\tau_{21})$$

$$\tau_{2\pm2} = \frac{1}{2\sqrt{3}}(S_{xx} - S_{yy} \pm 2iS_{xy}) \qquad S_{yz} = \frac{i\sqrt{3}}{2}(\tau_{21} + \tau_{2\text{-}1}) = -\sqrt{3}\mathrm{Im}(\tau_{21})$$

$$S_{xx} = \frac{\sqrt{3}}{2}(\tau_{22} + \tau_{2\text{-}2}) - \frac{1}{\sqrt{2}}\tau_{20} = \sqrt{3}\mathrm{Re}(\tau_{22}) - \frac{1}{\sqrt{2}}\tau_{20}$$

$$S_{yy} = \frac{-\sqrt{3}}{2}(\tau_{22} + \tau_{2\text{-}2}) - \frac{1}{\sqrt{2}}\tau_{20} = -\sqrt{3}\mathrm{Re}(\tau_{22}) - \frac{1}{\sqrt{2}}\tau_{20}$$

$$S_{zz} = \sqrt{2}\tau_{20}$$

(B.1)

The Cartesian operators are defined by,

$$S_i \qquad i=x,y,z$$
$$S_{ij} = \frac{3}{2}(S_iS_j + S_jS_i) - 2\delta_{ij}\mathbf{1} \qquad i,j=x,y,z \tag{B.2}$$

where

$$S_x = \frac{1}{\sqrt{2}}\begin{pmatrix} 0 & 1 & 0 \\ 1 & 0 & 1 \\ 0 & 1 & 0 \end{pmatrix} \quad S_y = \frac{1}{\sqrt{2}}\begin{pmatrix} 0 & -i & 0 \\ i & 0 & -i \\ 0 & i & 0 \end{pmatrix} \quad S_z = \begin{pmatrix} 1 & 0 & 0 \\ 0 & 0 & 0 \\ 0 & 0 & -1 \end{pmatrix} \tag{B.3}$$

are the matrix representations. The spherical tensor operators obey the relation

$$\tau_{kq} = (-1)^q \tau^{\dagger}_{k-q} \, . \tag{B.4}$$

The polarization moments for each representation are defined as the expectation value of the respective operators (i.e. $p_{ij} = \langle S_{ij} \rangle$ and $t_{kq} = \langle \tau_{kq} \rangle$).

The non-zero analyzing powers (defined in Eqns. 3.10 and 3.11) in each representation are related via the following expressions:

$$A_y = \frac{2}{\sqrt{3}} iT_{11} \qquad iT_{11} = \frac{\sqrt{3}}{2} A_y$$
$$A_{xz} = -\sqrt{3}T_{21} \qquad T_{21} = \frac{1}{\sqrt{3}} A_{xz}$$
$$A_{zz} = \sqrt{2}T_{20} \qquad T_{20} = \frac{1}{\sqrt{2}} A_{zz}$$
$$A_{xx} = \sqrt{3}T_{22} - \frac{1}{\sqrt{2}}T_{20} \qquad T_{22} = \frac{1}{2\sqrt{3}}(A_{xx} - A_{yy})$$
$$A_{yy} = -\sqrt{3}T_{22} - \frac{1}{\sqrt{2}}T_{20} \tag{B.5}$$

Appendix C

Rotation of the Scattering Matrix and Vector and Tensor Polarization Observables for Spin 1 Particles

The transition matrix for deuterons scattering from a spinless target (defined in section 3.4) can be represented by a 3×3 matrix which is a linear combination of the spin operators for spin 1 (see Appendix B). Both the transition matrix and the polarization observables (see Eqn. 3.11) are defined with respect to a specific reference frame. They may be related to observables in a different frame through rotation relations. In particular, the transition matrix $M(E,\theta)$ (see Eqn. 3.23) can be rotated into a new frame producing $M'(E,\theta')$ through operation by the rank-one rotation matrix $d^{(1)}(\psi)$ where

$$d^1(\psi) = \frac{1}{2}\begin{pmatrix} (1 + cos\ \psi) & \sqrt{2}sin\ \psi & (1 - cos\ \psi) \\ -\sqrt{2}sin\ \psi & 2cos\ \psi & \sqrt{2}sin\ \psi \\ (1 - cos\ \psi) & -\sqrt{2}sin\ \psi & (1 + cos\ \psi) \end{pmatrix} \tag{C.1}$$

and $M'(E,\theta') = d^{(1)}(\psi)M(E,\theta)$. The angle $\psi = (\theta' - \theta)$ is defined by a counter-clockwise rotation about the y axis perpendicular to the scattering plane for which M is defined. The polarization observables calculated in both the primed and unprimed frames can be related through the block-diagonal rotation matrices

$$\begin{pmatrix} p_{y'} \\ p_{x'} \\ p_{z'} \end{pmatrix} = \begin{pmatrix} 1 & 0 & 0 \\ 0 & \cos\psi & -\sin\psi \\ 0 & \sin\psi & \cos\psi \end{pmatrix} \begin{pmatrix} p_y \\ p_x \\ p_z \end{pmatrix} \tag{C.2a}$$

$$\begin{pmatrix} p_{y'y'} \\ p_{x'y'} \\ p_{y'z'} \\ p_{x'x'} \\ p_{x'z'} \\ p_{z'z'} \end{pmatrix} = \begin{pmatrix} 1 & 0 & 0 & 0 & 0 & 0 \\ 0 & \cos\psi & -\sin\psi & 0 & 0 & 0 \\ 0 & \sin\psi & \cos\psi & 0 & 0 & 0 \\ 0 & 0 & 0 & \cos^2\psi & -\sin 2\psi & \sin^2\psi \\ 0 & 0 & 0 & \frac{1}{2}\sin 2\psi & \cos 2\psi & -\frac{1}{2}\sin 2\psi \\ 0 & 0 & 0 & \sin^2\psi & \sin 2\psi & \cos^2\psi \end{pmatrix} \begin{pmatrix} p_{yy} \\ p_{xy} \\ p_{yz} \\ p_{xx} \\ p_{xz} \\ p_{zz} \end{pmatrix} . \tag{C.2b}$$

The relation between Cartesian polarization moments are shown as an example. They may be replaced with any set of Cartesian vector and tensor observables (e.g. P^i and P^{ij} or K_y^i and K_y^{ij}).

Appendix D

Polarimeter Calibration Information for the $^3He(\vec{d},p)^4He$ and $^4He(\vec{d},d)^4He$ Reactions between 5-12 MeV

Results of the polarimeter calibration experiments are compiled below including the analyzing powers $A_y(25°)$, $A_{yy}(25°)$, $A_{zz}(25°)$ and $A_{zz}(0°)$ for five energies between 5 MeV and 11 MeV (see Table D.1) within the polarimeter gas cell. These calibration data were taken using the secondary polarization standard $^4He(d,d)^4He$ elastic scattering at the laboratory angles 37.5° and 52.5° for energies ranging from 10 MeV to 14 MeV. The elastic scattering information at these angles is the same as compiled and used in [Ton80]. Calibration graphs for A_y and A_{yy} at 37.5° and 52.5° are also shown (see Figures D.1 and D.2).

Reference data of side-to-back detector cross section ratios (Σ_0/B_0) for comparison with Monte Carlo calculations are compiled in Table D.3. The calculations A, B and C are described in section 4.3. Finally, relative cross section information for the forward angle scattering (0°-30°) for the $^3He(d,p)^4He$ reaction are also shown (in Table D.2) for energies between 5 MeV and 12 MeV. These data were used to supplement cross section information from Grüebler *et al.* [Grü73] used in the Monte Carlo calibration of the polarimeter. These data are normalized to the data of [Grü73] at 11.5 MeV.

MeV	$A_y(25°)$	ΔA_y	$A_{yy}(25°)$	ΔA_{yy}	$A_{zz}(25°)$	ΔA_{zz}	$A_{zz}(0°)$	ΔA_{zz}
5.73	-0.176	0.014	0.695	0.047	-0.835	0.056	-1.797	0.047
7.21	-0.310	0.027	0.799	0.048	-0.745	0.044	-1.721	0.104
8.55	-0.429	0.028	0.828	0.031	-0.801	0.030	-1.575	0.059
9.80	-0.505	0.032	0.788	0.029	-0.745	0.028	-1.369	0.051
11.03	-0.574	0.060	0.687	0.071	-0.639	0.064	-1.089	0.110

Table D.1 - $^3He(\vec{d},p)^4He$ analyzing power measurements for the deuteron polarimeter. Errors shown include statistical uncertainties as well as estimated (≈3%) uncertainty in the $^4He(\vec{d},d)^4He$ calibration information.

Energy (MeV)	25°	0°	10°	15°	20°	30°
5.25	7.676	12.315	11.128	9.846	8.454	6.314
6.33	7.128	13.465	----	----	----	----
7.39	6.152	13.477	11.217	9.403	7.549	4.702
8.44	5.129	12.829	----	----	----	----
9.48	4.413	12.328	11.227	8.843	6.378	3.153
10.52	3.696	12.517	----	----	----	----
11.50	3.200	12.358	9.283	7.076	4.688	2.320

Table D.2 - $^3He(d,p)^4He$ cross section measurements at forward angles for use in Monte Carlo calculations. They are relative cross sections normalized to the data of [Grü73] at 11.5 MeV. The relative errors for these measurements are estimated at 2.5% for the 10°-30° data and 3.5% for the 0° data. This includes both statistical (≈1%) and estimated systematic uncertainties (1.5-2.5%).

Data for Monte Carlo Calc. A		Data for Monte Carlo Calc. B		Data for Monte Carlo Calc. C	
Average Energy in Gas Cell (MeV)	0.159 cm Circular Collimator	Average Energy in Gas Cell (MeV)	0.635 cm Square Collimator (direct beam)	Average Energy in Gas Cell (MeV)	0.635 cm Square Collimator (scattered beam)
5.198	1.68±0.08	8.961	1.94±0.09	5.731	4.31±0.18
7.070	1.32±0.08	-----	------	6.850	4.06±0.16
7.902	1.17±0.08				

Table D.3 - Reference data taken for comparison with Monte Carlo calculations of the polarimeter performance. Experimental setups for each experiment are described in section 4.3 (Monte Carlo modeling...). Uncertainties are estimated from deviations in multiple measurements.

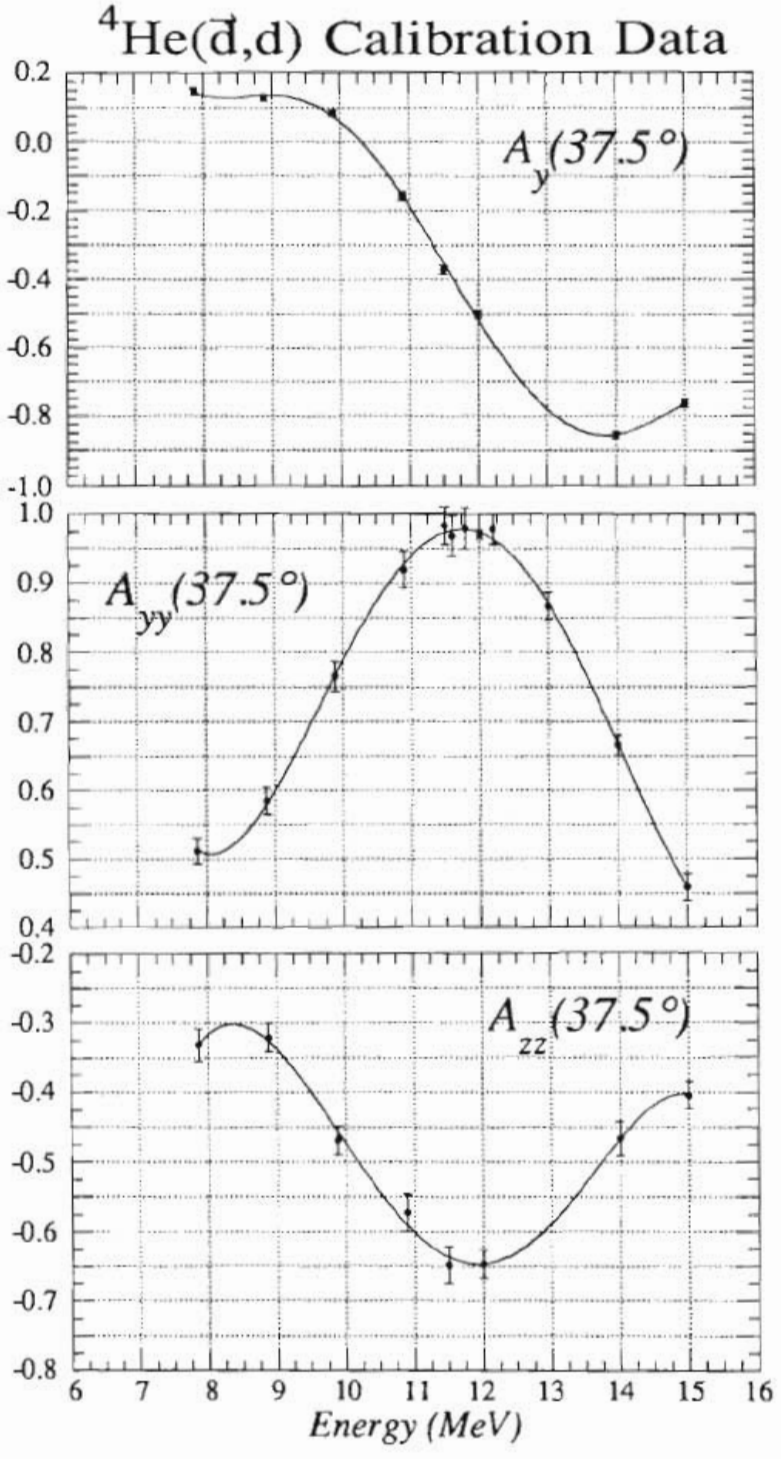

Figure D.1 - Calibration curves for $^4He(\vec{d},d)^4He$ elastic scattering at $\theta_{lab} = 37.5°$. The data comes from compiled information in [Ton80].

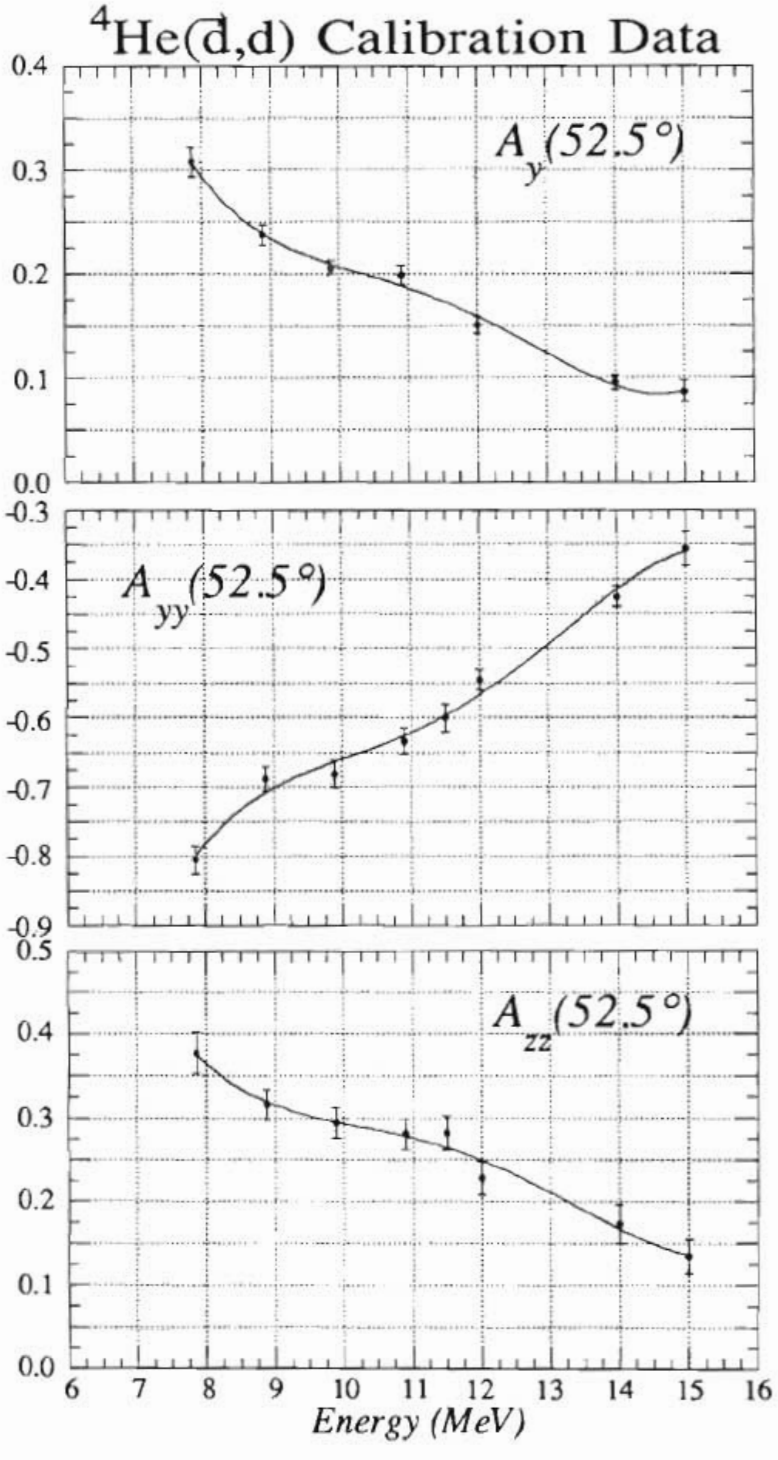

Figure D.2 - Calibration curves for $^4He(\vec{d},d)^4He$ elastic scattering at θ_{lab} = 52.5°. The data comes from compiled information in [Ton80].

Appendix E

Tables of Measurements for $^{90}Zr(\vec{d},\vec{d})^{90}Zr$ and $^{90}Zr(d,p)^{91}Zr$ Scattering Observables

Compiled below are the analyzing power and polarization transfer measurements for polarized deuteron elastic scattering from ^{90}Zr as well as absolute cross sections for the $^{90}Zr(d,p)^{91}Zr$ reaction all taken at TUNL with incident energy of 15 MeV. Additional data for deuteron scattering from ^{90}Zr discussed in this dissertation were acquired from several sources [Har72, God78, Hor72, Bak75].

Angle (cm)	$A_y(\theta)$	ΔA_y	$A_{yy}(\theta)$	ΔA_{yy}	$A_{xx}(\theta)$	ΔA_{xx}
25.5400	-0.0110	0.0038	0.0102	0.0049	-0.0231	0.0047
30.6400	-0.0311	0.0014	0.0066	0.0015	-0.0338	0.0035
35.7400	-0.0448	0.0022	0.0029	0.0024	-0.0258	0.0052
40.8300	-0.0087	0.0013	0.0212	0.0018	-0.0417	0.0047
45.9100	0.0496	0.0030	0.0191	0.0036	-0.0321	0.0097
50.9800	0.0209	0.0022	0.0055	0.0028	-0.0189	0.0054
56.0500	-0.0711	0.0051	0.0208	0.0068	-0.0257	0.0107
61.1100	-0.1517	0.0063	0.0231	0.0051	-0.0447	0.0072
66.1600	-0.1940	0.0085	0.0833	0.0102	-0.0857	0.0144
71.2100	-0.0098	0.0092	0.0594	0.0113	-0.0698	0.0153
76.2400	0.2135	0.0122	-0.0331	0.0154	-0.0688	0.0232
81.2600	0.0883	0.0113	-0.0450	0.0214	0.0040	0.0194
86.2800	-0.0854	0.0108	0.0186	0.0162	-0.0471	0.0164
91.2800	-0.2481	0.0084	0.0767	0.0107	-0.0320	0.0173
96.2800	-0.4176	0.0185	0.2260	0.0258	-0.0829	0.0198
101.2600	-0.3051	0.0154	0.2099	0.0232	-0.1270	0.0372
106.2400	0.1789	0.0241	0.1159	0.0369	-0.1237	0.0375
111.2100	0.4012	0.0205	-0.1920	0.0274	0.0186	0.0560
116.1600	0.1566	0.0133	-0.0859	0.0179	-0.0361	0.0155
121.1100	-0.1572	0.0136	0.0353	0.0185	0.0344	0.0380
126.0500	-0.3076	0.0134	0.1366	0.0151	-0.0473	0.0137
130.9800	-0.4464	0.0144	0.3424	0.0178	-0.0590	0.0195
135.9100	-0.3838	0.0155	0.4280	0.0188	-0.0824	0.0179
140.8300	0.0033	0.0174	0.2093	0.0222	-0.0911	0.0319
145.7400	0.3107	0.0276	-0.2158	0.0368	0.0335	0.0322
150.6400	0.2086	0.0191	-0.5659	0.0297	0.1944	0.0308
155.5400	-0.1529	0.0231	-0.4024	0.0348	0.1242	0.0267
160.4400	-0.3380	0.0220	-0.1360	0.0290	-----	-----

Table E.1 - Measured analyzing powers for $^{90}Zr(\vec{d},d)^{90}Zr$ elastic scattering at E_d = 15 MeV. The errors shown include statistical uncertainties only. An additional systematic uncertainty of an absolute ±0.011 was estimated for all the above measurements.

Angle (cm)	$K_y^{z'z'}$	$\Delta K_y^{z'z'}$	K_A	ΔK_A
25.54	0.0374	0.1320	-0.8870	0.3090
30.64	0.1138	0.0992	-0.7048	0.2075
35.74	0.1056	0.1720	-0.5770	0.3330
50.98	0.1071	0.0995	-0.3310	0.2330

Table E.2 - Measurements of Polarization Transfer Observables for $^{90}Zr(\vec{d},\vec{d})^{90}Zr$ elastic scattering at E_d = 15 MeV. Errors for these data include statistical uncertainties as well as estimated relative uncertainties from Monte Carlo information (≈2–3%).

Angle (cm)	σ(θ) (0.00 MeV)	Δσ	σ(θ) (1.20 MeV)	Δσ	σ(θ) (2.04 MeV)	Δσ
25.3500	8.6099	0.0928	2.7472	0.0527	3.8149	0.0622
30.4100	4.3614	0.0538	3.1977	0.0654	2.1279	0.0380
35.4700	2.0625	0.0348	2.3991	0.0369	1.2639	0.0274
40.5300	2.1511	0.0306	1.5751	0.0274	1.2808	0.0243
45.5800	2.8875	0.0348	1.0719	0.0264	1.4591	0.0306
50.6300	2.9055	0.0316	0.7849	0.0222	1.3441	0.0264
55.6700	2.1174	0.0295	0.5708	0.0158	0.8904	0.0200
60.7100	1.2016	0.0243	0.4895	0.0169	0.5433	0.0179
65.7400	0.7153	0.0137	0.5359	0.0148	0.3735	0.0127
70.7700	0.5591	0.0127	0.5053	0.0158	0.3545	0.0148
75.7900	0.4885	0.0084	0.3545	0.0074	0.2901	0.0063
80.8100	0.4990	0.0084	0.2205	0.0042	0.2764	0.0063
85.8200	0.5064	0.0084	0.1329	0.0032	0.2500	0.0053
90.8200	0.4241	0.0053	0.0918	0.0021	0.1878	0.0032
95.8200	0.3376	0.0053	0.1108	0.0021	0.1519	0.0042
100.8100	0.2226	0.0042	0.1192	0.0032	0.1087	0.0032
105.7900	0.1604	0.0042	0.1097	0.0032	0.0952	0.0028
110.7700	0.1266	0.0021	0.1014	0.0018	0.0797	0.0032
115.7400	0.1224	0.0021	0.0736	0.0011	0.0910	0.0026
120.7100	0.1245	0.0021	0.0491	0.0014	0.0933	0.0034
125.6700	0.1488	0.0032	0.0381	0.0011	0.0912	0.0027

Table E.3 - Measurements of absolute cross sections for the $^{90}Zr(d,p)^{91}Zr$ reaction at E_d = 15 MeV. Measured states correspond to the g.s. (0.0 MeV, $5/2^+$), the 1.20 MeV $1/2^+$ state and the 2.04 MeV $3/2^+$ states in ^{91}Zr. Cross sections are in units of millibarns/sr. The errors represent statistical uncertainties only. There is an additional estimated systematic uncertainty of 2.5%. The normalization of this data is expected to be good to less than 6%.

References

Abb89 D.J. Abbott, H.J. Karwowski, T.B. Clegg and E.J. Ludwig, Nucl. Inst. and Meth. **A284** (1989) 409.

Bak75 F. T. Baker, S. Davis, C. Glashausser and A.B. Robbins, Nucl. Phys. **A233** (1975) 409.

Bar70 Madison Convention, Proc. of the 3rd Int. Syp. on Polarization Phenomena in Nuclear Reactions, ed. H.H. Barshall and W. Haeberli (University of Wisconsin-Madison, 1971) xxv.

Big61 J.A. Biggerstaff, R.L. Becker and M.T. McEllistrem, Nucl. Instr. and Meth. **10** (1961) 327.

Bow82 J.E. Bowsher, charged particle energy loss computer code BABEL, private communication.

Bow89 J.E. Bowsher, Ph. D. dissertation, University of North Carolina, 1989 (unpublished), available from University Microfilms International, 300 N. Zeeb Rd., Ann Arbor, Michigan 48106.

Bro78 R.E. Brown, W. Grüebler, R.A. Hardekopf, F. D. Correll, N. Jarmie and G. G. Ohlsen, Los Alamos internal report LA-7378-MS (July 1978).

Bür72 H.R. Bürgi, Nucl. Phys. **A321** (1972) 445.

Cle74 T.B. Clegg, A. Bissinger, T.A. Trainor, Nucl. Inst. Meth. **120** (1974) 445.

Cle90 T.B. Clegg, private communication, 1990.

Dae80 W.W. Daehnick, J.D. Childs and Z. Vrcelj, Phys. Rev. **C21** (1980) 2253.

Els88 K. Elsener, W. Grüebler, F. Sperison, K. Ghazi-Wakili, V. König, P.A. Schmelzbach, B. Vuaridel, M. Bittcher, D. Singy and J. Ulbricht, Nucl. Phys. **A481** (1988) 227.

Erm87 M. Ermer, H. Clement, P. Grabmayr, G.J. Wagner, L. Friedrich and E. Huttel, Phys. Lett. **B188** (1987) 17.

God76 R.P. Goddard, N. Rohrig, L.D. Knudson, and W. Haeberli, Nucl. Instr. and Meth. **137** (1976) 451.

God78 R.P. Goddard, Ph. D. dissertation, University of Wisconsin - Madison, 1978, (unpublished), available from University Microfilms International, 300 N. Zeeb Rd., Ann Arbor, Michigan 48106.

God79 R.P. Goddard and W. Haeberli, Nucl. Phys. **A316** (1979) 116.

Gol58 L.J.B. Goldfarb, Nucl. Phys. **7** (1958) 622.

Grü71 W. Grüebler, V. König, A. Ruh, P.A. Schmelzbach, R.E. White and P. Marmier, Nucl. Phys. **A176** (1971) 631.

Grü73 W. Grüebler, 1973 internal ETH Zürich report and private communication to UNC nuclear physics group.

Grü75 W. Grüebler, P.A. Schmelzbach, V. König, R. Risler, B. Jenny and D. Boerma, Nucl. Phys. **A242** (1975) 285.

Grü79 W. Grüebler, R.E. Brown, F.D. Correll, R.A. Hardekopf, N. Jarmie and G.G. Ohlsen, Nucl. Phys. **A331** (1979) 61.

Grü82 W. Grüebler, F. Sperisen, K. Elsener, V. König, P.A. Schmelzbach, B. Jenny, C. Schweizer, and J. Ulbrict, Nucl. Inst. and Meth. **203** (1982) 235.

Grü87 W. Grüebler, V. König, P.A. Schmelzbach, M. Bittcher, B. Vuaridel, Ch. Forstner, D. Singy, I. Slaus and A. Chisholm, Nucl. Inst. and Meth. **A262** (1987) 307.

Hae67 W. Haeberli, Ann. Rev. Nucl. Sci. **17** (1967) 373.

Har72 R.A. Hardekopf, D.D. Armstrong, L.L. Catlin, P.W. Keaton, Jr. and C.P. Lawrence, Los Alamos internal report LA-5051 (October 1972).

Hoo71 D.J. Hooten and R.C. Johnson, Nucl. Phys. **A175** (1971) 583.

Hor72 J.L. Horton, C.L. Hollas, P.J. Riley, S.A.A. Zaidi, C.M. Jones and J.L.C. Ford, Jr., Nucl. Phys. **A190** (1972) 362.

Ise89 Y. Iseri, H. Kameyama, M Kamimura, M. Yahiro and M. Tanifuji, Nucl. Phys. **A490** (1989) 383.

Kea73 P.W. Keaton, Jr., and D.D. Armstrong, Phys. Rev. **C8** (1973) 162.

Knu73 L.D. Knutson and W. Haeberli, Phys. Rev. Lett **30** (1973) 986.

Knu75 L.D. Knutson and W. Haeberli, Phys. Rev. **C12** (1975) 1469.

Lai88 A. Laid, Masters Thesis, University of Surrey-England (1988, unpublished).

Leo87 W.R. Leo, Techniques for Nuclear and Particle Physics Experiments (1987), Springer-Verlag, New York.

Lop77 M.H. Lopes and F.D. Santos, Nucl. Phys. **A283** (1977) 77.

McI67 L.C. McIntyre and W. Haeberli, Nucl. Phys. **A91** (1967) 369.

Mac87 R.S. Mackintosh, S.G. Cooper and A.A. Ioannides, Nucl. Phys. **A472** (1987) 85.

Mat86 N. Matsuoka, H. Sakai, T. Saito, K. Hosono, M. Kondo, H. Ito, K. Hatanaka, T. Ichihara, A. Okihana, K. Imai and K. Nishimura, Nucl. Phys. **A455** (1986) 413.

Mit73 C.K. Mitchell, Los Alamos Internal Report LA-5412-5 (1973) unpublished.

Ohl72a G.G. Ohlsen, Rep. Prog. Phys. **35** (1972) 717.

Ohl72b G.G. Ohlsen, J.L. Gammel and P.W. Keaton, Jr., Phys. Rev. **C5** (1972) 1205.

Ohl73 G.G. Ohlsen, P.A. Lovoi, C.G. Salzman, U. Meyer-Berkhout, C.K. Mitchell and W. Grüebler, Phys. Rev. **C8** (1973) 1639.

Raw71 G.H. Rawitscher and S. N. Mukherjee, Ann. of Phys. **68** (1971) 57.

Raw77 G.H. Rawitscher, Bull. Am. Phys. Soc. **22** (1977) 597.

Raw78 G.H. Rawitscher and S.N. Mukherjee, Phys. Rev. Lett. **40** (1978) 1486.

Rei68 R.V. Reid, Ann. of Phys. **50** (1968) 411.

Rob74 B.A. Robson, The Theory of Polarization Phenomena (1974), Clarendon Press, Oxford.

Sal73 G.C. Salzman, C.K. Mitchell and G.G. Ohlsen, Nucl. Inst. and Meth. **109** (1973) 61.

Sat60 G.R. Satcher, Nucl. Phys. **21** (1960) 116.

Sim67 M. Simonius, Phys. Rev. Lett. **19** (1967) 279.

Sim70 M. Simonius, Proc. of the 3rd Int. Syp. on Polarization Phenomena in Nuclear Reactions, ed. H.H. Barshall and W. Haeberli (University of Wisconsin-Madison, 1971) 401.

Spe83 F. Sperisen, W. Grüebler and V. König, Nucl. Inst. and Meth. **204** (1983) 491.

Sta70 A.P. Stamp, Nucl. Phys. **A159** (1970) 399.

Ste80a E.J. Stephenson and W. Haeberli, Nucl. Inst. and Meth **169** (1980) 483.

Ste80b E.J. Stephenson, R.J. Holt, J.R. Specht, J.D. Moses, R.L. Burman, G.D. Crocker, J.S. Frank and M.J. Leitch, Nucl. Instr. and Meth. **178** (1980) 345.

Tak87 M. Takei, Y. Aoki, Y. Tagishi and K. Yagi, Nucl. Phys. **A472** (1987) 41.

Tan89 M. Tanifuji, private communication, (1989).

Tho88 I.J. Thompson, Comp. Phys. Rep. **7** (1988) 167.

Ton80 S.A. Tonsfeldt, Ph. D. dissertation, University of North Carolina, 1980, (unpublished), available from University Microfilms International, 300 N. Zeeb Rd., Ann Arbor, Michigan 48106.

Tos83 J.A. Tostevin and R. C. Johnson, Phys. Lett. **124B** (1983) 135.

Tos87 J.A. Tostevin, Nucl. Phys. **A466** (1987) 349.

Tos90 J.A. Tostevin, private communication, (1990).

Ulb84 J. Ulbricht, W. Grüebler, V. König, P.A. Schmelzbach, K. Elsener, C. Schweizer, M. Merdzan and A. Chisholm, Nucl. Inst. and Meth. **227** (1984) 57.

Var86 R.L. Varner, Ph. D. dissertation, University of North Carolina, 1986,(unpublished), available from University Microfilms International, 300 N. Zeeb Rd., Ann Arbor, Michigan 48106.
R.L. Varner, T.B. Clegg, T.L. McAbee and W.J. Thompson, Phys. Lett. **B185** (1987) 6.
R.L. Varner, to be published in Physics Reports.

Wat58 S. Watanabe, Nucl. Phys. **8** (1958) 484.

Yah82 M. Yahiro, M. Nakano, Y. Iseri and M. Kamimura, Prog. Theor. Phys. **67** (1982) 1467.